

Durham E-Theses

Landsliding and sediment dynamics following the 2008 Wenchuan Earthquake in the Beichuan area of China

WHADCOAT, SIOBHAN,KATHLEEN

How to cite:

WHADCOAT, SIOBHAN,KATHLEEN (2011) *Landsliding and sediment dynamics following the 2008 Wenchuan Earthquake in the Beichuan area of China*, Durham theses, Durham University. Available at Durham E-Theses Online: <http://etheses.dur.ac.uk/1369/>

Use policy

The full-text may be used and/or reproduced, and given to third parties in any format or medium, without prior permission or charge, for personal research or study, educational, or not-for-profit purposes provided that:

- a full bibliographic reference is made to the original source
- a [link](#) is made to the metadata record in Durham E-Theses
- the full-text is not changed in any way

The full-text must not be sold in any format or medium without the formal permission of the copyright holders.

Please consult the [full Durham E-Theses policy](#) for further details.

Academic Support Office, Durham University, University Office, Old Elvet, Durham DH1 3HP
e-mail: e-theses.admin@dur.ac.uk Tel: +44 0191 334 6107
<http://etheses.dur.ac.uk>

Landsliding and sediment dynamics following the 2008 Wenchuan Earthquake in the Beichuan area of China

Siobhan Kathleen Whadcoat

Department of Geography

University of Durham

Thesis submitted for the degree of Master of Science

Declaration

I confirm that no part of the material presented in this thesis has previously been submitted for a degree in this or any other university. In all cases the word of others, where relevant, has been fully acknowledged.

The copyright of this thesis rests with the author. No quotation from it should be published without prior written consent and information derived from it should be acknowledged.

Siobhan Whadcoat

University of Durham

Abstract

Extensive and widespread landsliding is a common feature in a post-earthquake mountainous environment. The intense seismic shaking of an earthquake leaves the ground destabilised and thus very susceptible to slope failure. In addition to co-seismic landsliding, many slopes retain the high potential to fail for a significant amount of time beyond seismic activity. Therefore there is a need to further develop our understanding of sediment dynamics of steep mountain environments once the shaking has stopped. The 2008 Wenchuan Earthquake in China resulted in widespread landsliding, generating large volumes of loose rock and soil. Examples from other recent large earthquakes warn of the potential secondary hazards associated with such loose material: up to 30m of river-bed aggradation was seen following the 1999 Chi-Chi Earthquake, Taiwan and it is thought that Sichuan may experience hazards of a similar magnitude. Preliminary reports and oblique photographs have displayed significant levels of sediment aggradation in certain areas and summer monsoonal rains continue to trigger further landslide failures. In addition to the associated hazards, this event has provided the opportunity to investigate sediment dynamics following a large earthquake ($M_w = 7.9$) in a unique area of heterogeneous lithology and wide ranging geophysical variables, which has been impacted upon by both seismic and post-seismic (rainfall) activity.

This study uses a combination of desk-based and field-based research in order to examine the distribution and evolution of post-seismic landslide failures. Volume-area scaling laws are developed in order to allow erosion rates to be calculated and finally an innovative oblique photography technique is used to constrain the depth of sediment aggradation. The results demonstrate that as a source of material, the occurrence of landslides in this region is controlled by a combination of topographic, geologic and seismological factors. Resulting volume estimations and subsequent erosion rates indicate that the Wenchuan earthquake has potentially destroyed more material through erosion than it has built through surface uplift. To conclude the movement of sediment through a mountain catchment, levels of sediment aggradation show that a significant proportion of material from the hillslope is transported down into the valley bottom; this is seen to coincide with periods of intense rainfall.

Overall, this research derives a unique assessment of sediment mobilisation in Sichuan in order to understand the controls on sediment remobilisation and secondary hazards. By constraining the extent of sediment sources and transfer, this research has the potential to aid the prediction of future post-earthquake hazards and landscape response in Sichuan, providing insight into the role of earthquakes in landscape evolution.

Acknowledgements

There are many people without whom this work would not have happened. I am very grateful for the advice, support and encouragement of many, and would particularly like to acknowledge and thank the following people:

My academic supervisors, Dr. Alexander Densmore and Dr. Nick Rosser. Without their support, wisdom and encouragement over the past 15 months not even the title page would exist. I am very grateful for their patience as I have tried new ideas and their help and sense of humour when things don't always go to plan. I have learnt considerably more than I had imagined I would throughout my masters degree and can attribute that to the time and effort that both Alex and Nick are willing to give to their students.

Rob Parker and Professor Dave Petley, for many very useful conversations about the Wenchuan earthquake and working on this project – thank you especially for your enthusiasm and encouragement. Dr. Danny Donoghue, for loaning me a very useful piece of fieldwork equipment and trusting me to take it to China and back. The I.T staff in the Geography department – I may have lost count of the number of times I have come to the office with a problem, but they are always able and willing to help. Also, thanks to many other friends in the department who have shared advice and wisdom over coffee on numerous occasions.

All those who assisted me during fieldwork: Professor Li Yong and his students, particularly Yan for accompanying me during fieldwork and helping with data collection; the Geohazards team at Chengdu University of Technology for allowing me to attend their conference; and most crucially thanks to Oli Tomlinson, without whom I would not have understood a word.

The Geographical Club and the Royal Geographical Society for their generous award of a fieldwork grant, which made the trip to China possible.

Friends and family who have been patient, supportive and made me laugh along the way. In particular, thanks to Harriet for a fantastic trip to China; to Mel for being a wonderful cycling buddy and an inspiration to work harder; and to the wonderful staff at Leonards for keeping me sane, giving me some perspective and ultimately for providing coffee!

Dedication

This work is dedicated to the memory of Denis Daniel Jack – who inspired and encouraged me to explore the world and taught me that there is always more to learn.

Contents

Declaration	i
Abstract	ii
Acknowledgements	iii
Contents	iv
List of figures	vi
List of tables	viii
Glossary of terms	ix
Chapter 1 Introduction	1
1.1 Introduction and project rationale	1
1.2 Aim and Research Objectives	2
1.3 Study site	3
1.4 Thesis outline	5
Chapter 2 Literature review	6
2.1 Landsliding: controls and characteristics	6
2.2 Landslide inventory mapping	9
2.3 Sediment volume estimations	13
2.4 Transfer of material through the catchment	14
2.4.1 Sediment (re)mobilisation: controls and characteristics	14
2.4.2 Hillslope-fluvial coupling	15
2.5 Summary of research gaps	18
2.5.1 Landslides – the sediment source	18
2.5.2 Hillslope-fluvial coupling	19
Chapter 3 Landslides: the source	20
3.1 Methodology	20
3.1.1 Resources	20
3.1.2 Identifying slope failures – automated landslide mapping overview	27
3.1.3 Stage One: Classifications	29
3.1.4 Stage Two: Slope and noise filters	30
3.1.5 Stage Three: Editing	33
3.1.6 Stage Four: Shadow filter	35
3.1.7 Stage Five: Validation and evaluation of mapping	38
3.2 Analysis of landslide inventory maps	43
3.2.1 Preliminary results	43
3.2.2 Analysing the sample grids	53
3.2.3 Geophysical variables	57
Chapter 4 Landslide volumes and erosion rates	
4.1 Methods	78
4.2 Results	82
4.3 Application	89

4.3.1	Total landslide volume	89
4.3.2	Regional erosion rates	92
4.3.3	Geologic influence	96
Chapter 5	Sediment aggradation: storage within the catchment	100
5.1	Methods	102
5.2	Technique evaluation	108
5.3	Results	114
Chapter 6	Analysis and Discussion	123
6.1	Landscape characteristics and landslide occurrence	124
6.1.1	Comparing Beichuan to the wider earthquake affected region	124
6.1.2	Temporal changes in landsliding: June 2008 – March 2009	128
6.1.3	The influence of landslide location	129
6.2	Sediment movement: the impact of the volume of displaced material	133
6.2.1	Short-term	133
6.2.2	Long-term	134
6.3	In the context of wider literature on the Wenchuan earthquake	135
6.3.1	Post-seismic landslide evolution	136
6.3.2	(Re) mobilisation of material	137
6.4	Evaluation of the resources and techniques used	139
6.4.1	Satellite imagery	139
6.4.2	Volume scaling laws	139
6.4.3	Oblique photographs and sediment aggradation technique	140
Chapter 7	Conclusions	145
7.1	Main findings	145
7.2	Contribution to knowledge	146
7.3.	Future research	147
References		148

List of figures

Chapter 1

1.1	Overview map and photograph of the study area	4
-----	---	---

Chapter 2

2.1	Earthquake magnitude plotted against landslide area (after Keefer, 1999)	7
2.2	Identifying slope failures from satellite imagery	10
2.3	Spectral signatures of bare soil, vegetation and water	11
2.4	Examples of landslide inventory maps	12
2.5	Sediment movement flow diagram	17
2.6	Landslide classification after Imazumi and Sidle (2007)	18

Chapter 3

3.1a	Map of the earthquake rupture zone	23
3.1b	Satellite imagery used for landslide mapping	23
3.2	Landslide failures in image S1 and S2	24
3.3	Final area of imagery available for mapping	25
3.4	Comparison between failures in the satellite image and an oblique photograph	26
3.5	Landslide classification algorithm summary	28
3.6	Histogram of panchromatic image S2	29
3.7	Images of stages during the unsupervised classification	31
3.8	Landslide raster post the application of the slope and noise filters	32
3.9	Images displaying the manual editing of landslide features	34
3.10	Hillshade map	36
3.11	Final mapped area and landslide inventory maps	36-37
3.12	Test area used in comparison of mapping techniques	41
3.13	Sample grids	45
3.14	Maps of landslide density based on 500 m ² sample grid	46
3.15	Case study 1	49
3.16	Case study 2	50
3.17	Case study 3	51
3.18	Case study 4	52
3.19a	Kernel density plots for image S3	55
3.19b-d	Log-frequency plots based on landslide inventory data	55-56
3.20	Plots displaying the relationship between landslide density and distance from the fault	61-62
3.21	Landslide density distribution plots against slope gradient	63
3.22	Normalised plots displaying landslide distribution across slope gradients	64-65
3.23	Normalised difference plot based on landslide distribution across slope gradients	66
3.24	Normalised plots displaying landslide distribution across local elevation	68

3.25	Landslide density distribution plots against local elevation	69
3.26	Landslide density maps and a map of geologic units	71
3.27	Normalised plots displaying landslide distribution across geologic units	72
3.28	Landslide density distribution plots against geologic unit	73
3.29	Plots of temporal changes in landslide density for each geologic unit	74
3.30	Normalised plots displaying landslide distribution over slope aspect	76-77
 Chapter 4		
4.1	Map of fieldwork locations	80
4.2	A schematic diagram illustrating the method used to measure scar depth	81
4.3	Landslide area-volume plot for failures measured in field	85
4.4	Landslide area-volume plots for failures measured in the hanging wall and the footwall	86
4.5	Landslide area-volume plots representing scaling relationships from various literature sources	87
4.6	Landslide area-volume plots	88
4.7	Landslide area-volume plot for failures measured in field, defined by geologic unit	98
4.8	Plot displaying the distribution of landslide volume across geologic units	99
 Chapter 5		
5.1	Sediment movement flow diagram	101
5.2	Initial photograph collection of Beichuan town	104
5.3	Map of photographic benchmark locations	105
5.4	Photographs displaying fieldwork data collection in Beichuan	107
5.5	Plot of error in building height estimations	110
5.6	Surface models of sediment aggradation in Beichuan town	112-113
5.7	Temporal changes in landslide and aggraded sediment volumes for the Beichuan catchment	118
5.8	Conceptual model of temporal changes in sediment volumes	121
5.9	Exponential plots of sediment volume against time for the Beichuan catchment	122
 Chapter 6		
6.1	Co-seismic landslide density against slope angle (from Sato and Harp, 2009)	127
6.2	Photographs displaying differing landslide failures around Beichuan town	132
6.3	Sediment movement flow diagram	138
6.4	Photographs displaying high-density landsliding around Beichuan town	142
6.5	Automated landslide mapping of image S2, highlighting areas of omission	143
6.6	Satellite images illustrating landslide failure coalescence in mapping	144

List of tables

Chapter 2

2.1	Formulas for estimating landslide volume	14
-----	--	----

Chapter 3

3.1	Parameters for satellite imagery landslide recognition	32
3.2	Results of the comparison between mapping techniques	42
3.3	Results of technique validation	42
3.4	Summary statistics from landslide inventory maps	44
3.5	Geophysical variables used in evaluating landslide inventories	58

Chapter 4

4.1	Results of landslide volume calculations	91
4.2	Erosion rates calculated from landslide volume estimates	95
4.3	Denudation calculated from landslide volume estimates	95

Chapter 5

5.1	Photograph sources	106
5.2	Photographic analysis measurements	111
5.3	Results of landslide sediment volume and aggraded sediment volume for the Beichuan and Huangjiaba catchments	117

Glossary of terms

Denudation (erosion) – the combination of erosional and weathering processes that wear away the earth's surface. This term is used interchangeably with erosion in this work: **regional erosion** – erosion averaged over the entire study region; **landslide erosion** – erosion averaged over the total landslide area

Distance decay – the reduction in the number and area of landslides with increasing distance from the fault rupture

Elevation: local – elevation values with respect to the local catchment, i.e. catchment base level taken as 0m; **raw** – elevation values taken directly from the DEM, i.e. sea level= 0m

Fault movements: thrust – relative movement occurs across the fault and ground on one side of the fault moves up and over ground on the other side; **strike-slip** – movement occurs along the fault as tectonic plates on either side of the fault slide past one another

Geophysical variables - parameters used to evaluate the influence of the physical landscape on landsliding: gradient, elevation, geology, aspect

Hanging wall effect - the effect resulting from larger acceleration and increased ground movement in the hanging wall compared to the footwall

Kernel density estimation - provides an estimation of the probability density function of a variable

Landslide (also referred to as failure) – the downslope movement of a mass of rock and earth, which moves primarily by sliding as one mass, maintaining contact with the ground

Landslide density (Mean – P^{ls}) - the number of landslides in a given area, i.e. per km²

Oblique photographs – photographs taken with the camera axis inclined greater than 0°, between the horizontal and the vertical

Rockfall – the downslope movement of loose rock, which moves primarily by falling or rolling as individual rocks rather than as one mass (landslide)

Satellite imagery: panchromatic – 5m resolution, single band SPOT imagery; **multispectral (m-x)** – 10m resolution, four band SPOT imagery

Sedimentation – the process by which particles of sediment settle out of the fluid (or fluid-sediment mix) that they're entrained in; the end of sediment transport

Sediment aggradation – the deposition and build up of sediment, in an area where the supply of sediment is greater than what can be transported by the system

1. Introduction

1.1. Introduction and project rationale

The intensity of seismic shaking associated with an earthquake leaves the ground destabilised and fragile and thus with significant potential for slope failure (Matsuoka *et al.*, 2008). In order to attempt post-earthquake control and mitigation plans, developing an understanding of post-earthquake sediment dynamics is crucial. Assessment of the geomorphic consequences of earthquakes, i.e. landsliding, is essential over shorter time scales for hazard mitigation and risk assessment (Owen *et al.*, 2008) and over longer time scales to understand the influence of geomorphic events on landscape evolution (Densmore *et al.*, 1997).

Geomorphic impacts: post-earthquake hazards

Landslides are the main secondary hazard associated with earthquakes and storms in mountainous regions; both co-seismic and post-seismic failures cause severe damage and loss of life (Meunier *et al.*, 2008). As a dominant mass wasting process (Hovius *et al.*, 1997), landslides significantly affect the transfer of sediment through a mountain catchment and consequently also impact on the fluvial network (i.e. Dadson *et al.*, 2004).

Co-seismic landsliding generates large volumes of loose rock and debris, which can lead to a range of hazards (Huang and Li, 2009a). However the significance of this material is often realised when storms and heavy rainfall trigger remobilisation of the loose material (Harp and Jibson, 1996). Post-seismic landslides commonly occur in areas where the slopes have been pre-conditioned to failure through seismic impact (Dadson *et al.*, 2004). Although the distribution of co-seismic and post-seismic landslides in the landscape often differs (Densmore and Hovius, 2000), they are both primarily responsible for the transfer of material from hillslopes into the fluvial network (Lin *et al.*, 2008) and therefore exert a significant control on sediment efflux from active mountain catchments (Hovius and Stark, 2002).

Geomorphic impacts: long-term landscape development

Beyond the immediate (short-term) hazards, signatures of seismically-triggered landslides continue to be seen in sediment dynamics and landscape evolution. The sediment budget in a catchment is driven by sediment mobilisation (Hovius *et al.* 2000) and the persistence of the geomorphic impact of landslides in a mountain environment may last for up to 10^4 yr, significantly influencing patterns of erosion and sedimentation over this time (Korup *et al.*, 2009). The ability to quantify erosion caused by landsliding enables the scale of denudation from landsliding to be derived (Barnard *et al.*, 2001).

The Wenchuan Earthquake

On 12th May 2008, the Wenchuan Earthquake $M_w = 7.9$ occurred in the Sichuan region, southwest China (USGS, 2008). It ruptured along the fault system of the Longmen Shan mountain range with a c.300 km rupture zone, overall impacting an area greater than 130,000 km² (Huang and Li, 2009a). The resulting death toll of over 70,000 provides significant motivation for greater understanding of this catastrophic event and the hazards that followed. Over 100,000 landslides have been identified, with a cumulative area of more than 560 km² (Parker *et al.*, 2009). As outlined above, the potential for remobilisation of this material is a significant secondary hazard; for example, 30 m of river-bed aggradation followed the 1999 Chi-Chi Earthquake, Taiwan and there are indications that Sichuan may experience hazards of a similar magnitude (Wang, 2009a). Photographs of the region provide evidence to suggest that the heavy monsoonal rains of September 2008 caused a considerable transfer of material from the hillslopes to the valley floor (Lin and Tang, 2009). Constraining the extent of this sediment is essential to aid future prediction and assessment of post-earthquake hazards in the region and to provide further insight into the role of earthquakes in landscape evolution more widely. This event has provided a unique opportunity to investigate post-earthquake sediment dynamics for a significantly large earthquake ($M_w = 7.9$) in an area of heterogeneous lithology and wide ranging geophysical variables, which has been impacted upon by both seismic and post-seismic (rainfall) activity.

1.2. Aim and Research Objectives

1.2.1. Aim

This research seeks to assess the controls upon and impact of the mobilisation of debris released by landslides triggered during the Wenchuan Earthquake in China, May 2008.

1.2.2. Objectives

To achieve my aim I will assess sediment mobilisation and consequent aggradation of earthquake released landslide sediment to better understand the impact upon landscape-scale sediment dynamics by constraining sources, transfers and sinks of material. This will be attained through the following research objectives:

- i. Map the evolution of landslides from satellite images captured since the earthquake, focussing on rainfall triggered landslide failure evolution.

- ii. Constrain topographic controls on sediment generation using topographic analysis in GIS, in order to estimate the contribution of landslide derived sediments to the fluvial system.
- iii. Map the extent and evolution of sedimentation in valleys using satellite imagery and, innovatively, oblique photography to give a vertical control on aggradation.
- iv. Use fieldwork to constrain the depth of landslides, and to ground truth GIS analysis results (Obj. i-iii).

1.2.3. Research Hypotheses

Through the attainment of the research objectives, I will test the following hypotheses:

- i. I predict that rainfall triggered landslides will have a similar spatial distribution to seismically triggered landslides on a regional level. However at the catchment level I expect to see a difference in their distribution: the rainfall triggered landslides are likely to occur at a lower point on the hillslope compared to seismically triggered landslides.
- ii. I expect that the characteristics of landslide derived sediment mobilisation, including volume, will vary spatially in correlation with geology, distance from co-seismic surface ruptures and topographic controls.
- iii. I predict that the extent and evolution of sedimentation in valleys will correlate temporally with the occurrence of large rainfall events, whilst the characteristics of the landslide material will exert a strong control on spatial variations.

1.3. Study site

This research is based in Sichuan province, China, with a focus upon Beichuan town, an area severely impacted upon by earthquake-related landsliding (Figure 1.1). Beichuan is located on the Beichuan fault at a point where the co-seismic slip along strike changed from a dominantly thrusting motion (vertical) to a dominantly strike-slip motion (horizontal) (Ouimet, 2010). As a result the seismic impact in this area was significantly greater than many other points along the fault rupture (Densmore *et al.*, in review) as demonstrated by the severe landsliding.

Satellite imagery and oblique photographs of this area have allowed landsliding and sedimentation to be assessed and quantified remotely as many areas are inaccessible. In addition, field data collection in this area has provided information that cannot be gained from imagery and subsequently has contributed significantly to a uniquely focussed and detailed study of the Beichuan area.

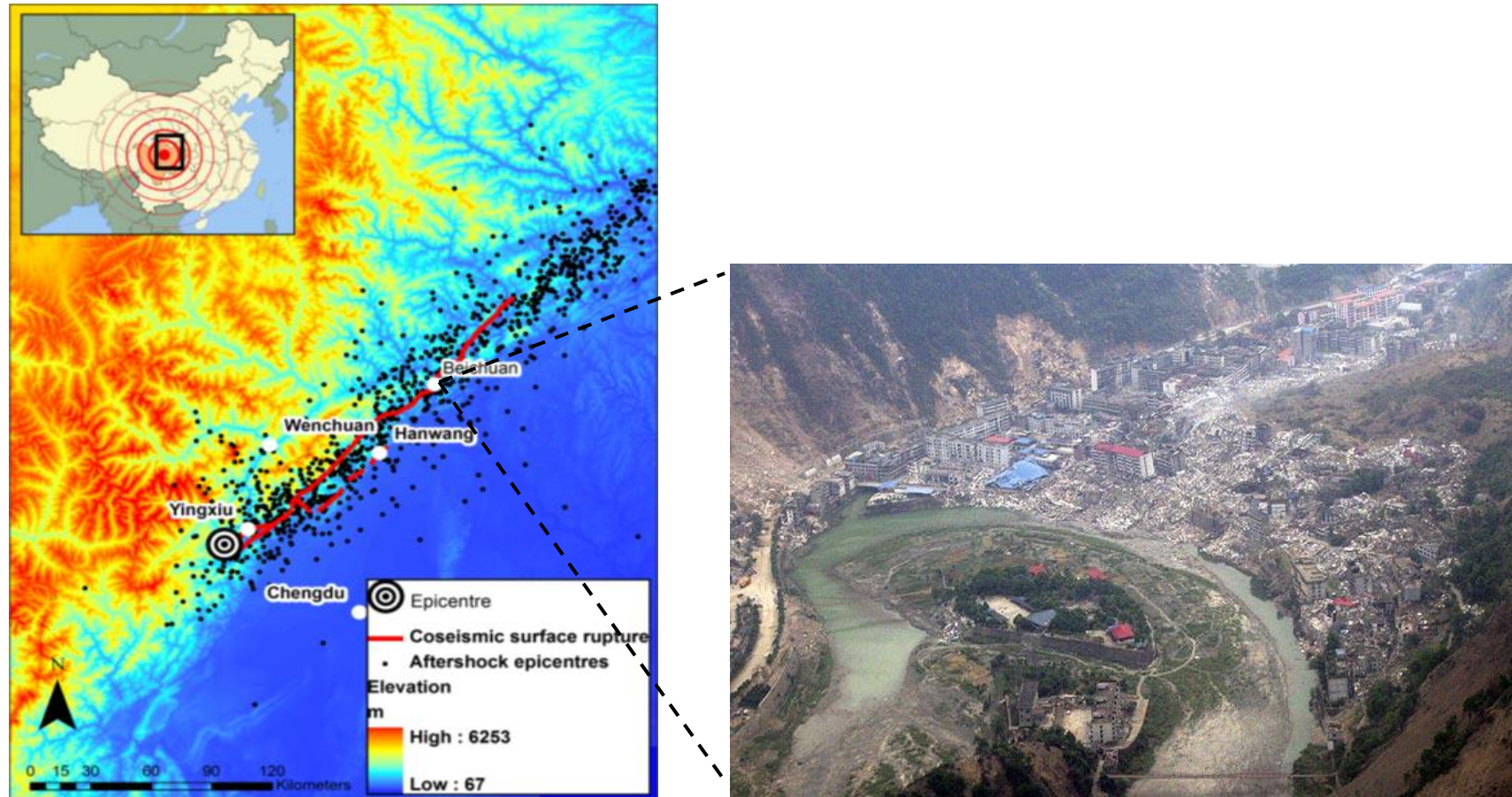


Figure 1.1: Overview map of the earthquake affected area (after Parker, 2010). The photograph shows Beichuan town 9 days after the earthquake occurred.

1.4. Thesis outline

Chapter 2 outlines our current understanding of this topic through a review of the key literature regarding earthquake-related landsliding and associated sediment dynamics.

Chapter 3 outlines the process of landslide mapping in order to generate three landslide inventories for June 2008, October 2008 and March 2009. It also presents the results generated from analysis of these maps with respect to seismic, topographic and geologic variables.

Chapter 4 details the development and application of a volume-area scaling law in order to quantify the volume of eroded material by landsliding following the Wenchuan earthquake.

Chapter 5 presents a unique insight into post-earthquake sediment aggradation on the valley floor through a case study of Beichuan Town: this chapter explores an innovative oblique photography technique in order to quantify the depth of sediment.

Chapter 6 presents additional analysis and discussion of the results from Chapters 3-5 in the context of literature introduced in Chapter 2. It considers landslides as the sediment source and subsequent movement of material before going on to consider these results in the context of wider literature regarding sediment dynamics following the Wenchuan earthquake. Finally, the resources and techniques used in this study are evaluated.

Chapter 7 provides a conclusion; a final summary of the findings of this study.

2. A review of post-earthquake landsliding and associated sediment dynamics

Scientific, post-earthquake investigations can be found as far back as 1783, however an awareness of the significance of post-earthquake landsliding and associated sediment dynamics has primarily developed over the last century (Keefer 2002). Work dating back to the early 1900s speculated over the importance of earthquake-induced landslides on sediment deposits (see Keefer, 1994 for a review) and since then many further studies have sought to understand and quantify the importance of earthquakes upon sediment dynamics and consequent landscape evolution (Hovius and Stark 2002; Lin et al. 2008; Korup et al. 2009). The developments in remote sensing, computer-based information systems and other technological advancements have significantly enhanced understanding of these processes as locations or scales that were previously not investigated have become accessible for research (Keefer and Larsen 2007).

The following discussion reviews previous studies and literature to outline the current understanding of seismically associated landsliding and sediment dynamics throughout the catchment. The discussion then draws attention to research gaps in both the understanding of aforementioned processes and also in the approaches taken to study them. Finally, a short review of published literature on the Wenchuan earthquake provides a background to the earthquake event.

2.1. Landsliding: controls and characteristics

Landsliding is recognised as a vital geomorphic process in the evolution of mountain landscapes (Hovius et al. 2000; Meunier et al. 2008). Not only do they play a significant role in shaping hillslope morphology (Densmore et al. 1997) but they provide a major source of sediment to the catchment (Schuerch et al. 2006). As a result many studies to date have focused on investigating the controls and characteristics of landslides and their place within catchment dynamics. Whilst it is recognised that landslides are generated by a wide range of natural and human causes (Keefer 1999) the review of studies which follows will focus on those associated with seismic activity: both co-seismic landslides and post-seismic landslides – often triggered by heavy rainfall (Owen et al. 2008) – will be addressed.

Keefer (1984; 1994; 1999) has often produced pivotal research and vital contributions to improving our understanding of earthquake-induced landsliding. In his 1984 paper, '*Landslides*

caused by earthquakes' he importantly recognises that despite the known significance of earthquake-induced landslides, they are not well understood. Questions raised in this paper were to shape a large amount of geomorphological studies in this field over the following decades: they included questions regarding the types of landslides caused by earthquakes (Keefer 1999); the susceptibility of different materials to earthquake-induced landslides (Owen et al. 2008); and the relationship between landslide distribution and seismic parameters (i.e. Figure 2.1).

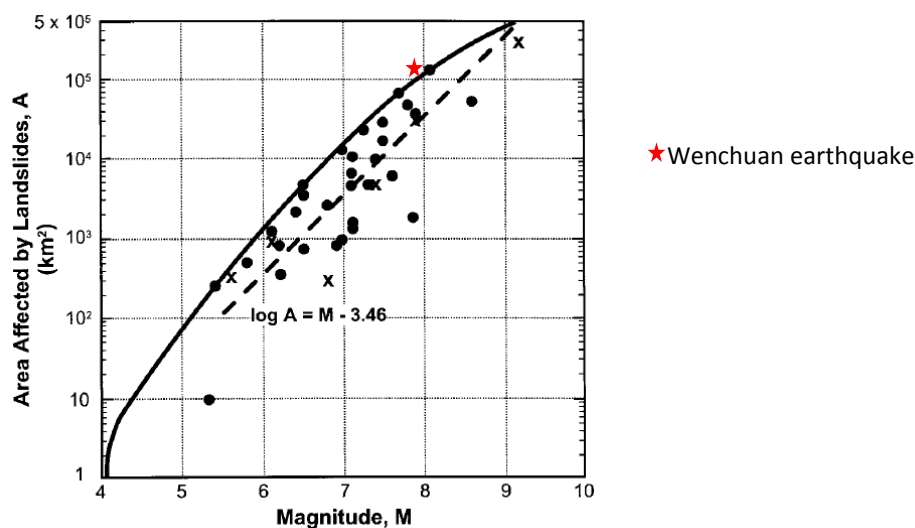


Figure 2.1: Earthquake magnitude, M, vs. Area affected by landslides triggered by earthquake (after Keefer and Wilson, 1989). Source: Keefer (1999) – updated from Keefer (1984).

Landslide distribution and seismic parameters

Results from Keefer (1984) provide a first-order quantification of the correlation between the area affected by landsliding and earthquake magnitude (Figure 2.1) – this is regarded as a significant control on co-seismic landsliding (Keefer 1994; Malamud et al. 2004b) and has provided a springboard for further investigation into the control of seismic parameters. Advancing studies in this field has shown that empirical relationships can be derived which directly link the event magnitude to total volume of landslides (Malamud et al. 2004b). Such developments in quantifying this relationship allow for predictions of landslide area and volume associated with an earthquake, presenting a measure of the seismic control on landsliding.

Additional seismic parameters have been studied for their controls upon the distribution of landslides. As seismic waves attenuate with distance from the epicentre, so does the density of earthquake-induced landslides (Meunier et al. 2008). Known as ‘density-decay’ this has become a well established and confirmed control upon the distribution of co-seismic landslides (Hovius et al. 2009), indicating how they reflect the dissipation of energy from an earthquake (Harp and Jibson 1996; Meunier et al. 2007): analysis of landslide distribution following the 1989 Loma Prieta earthquake showed an exponential decay in landslide occurrence with distance from the epicentre (Keefer 2000); and following the Chi-Chi earthquake, Taiwan in 1999, landslide density and the vertical component of peak ground acceleration displayed a linear relationship (Dadson et al. 2004). However in contrast to these studies and many others, some research has deemed ‘density-decay’ to be ineffective as a causative factor, arguing for a more detailed consideration of rupture dynamics (Lee et al. 2008), which highlights the complexities and variability associated with determining the controls on landsliding.

Co-seismic and post-seismic

The overall importance of earthquake-induced processes for landsliding following a large earthquake was questioned by Owen et al. (2008) in a study of landslides triggered by the 2005 Kashmir earthquake. Whilst they recognise the influence of seismic activity in inducing slope failure, they conclude that storm (monsoon) and human activity was more significant in determining the distribution and magnitude of landsliding (Owen et al. 2008). This is an issue often raised in papers discussing the controls on landsliding. For example in the development of analytical methods for assessing landslide behaviour, Cole et al. (1998) highlight the significant contribution of reactivated landslides associated with the Loma Prieta earthquake, 1989. Densmore and Hovius (2000) argue that over longer time scales, this implies the importance of storm triggers over earthquake triggers in the area. Conversely, a study by Keefer (1994) quantified the long-term importance of earthquake-induced landsliding through denudation rates of worldwide data and found that in a number of locations – but not all – earthquake-triggered landslides were more significant than storm-triggered landslides or other fluvial transport over historical time scales. Therefore it can be concluded that both earthquake and storm activity exert a control upon patterns of landsliding following an earthquake, but the level of importance given to either has considerable regional variability.

Documented patterns of landsliding have shown that effects of the dominant trigger mechanism can be seen as ‘topographic signatures’ on the landscape (Densmore and Hovius 2000; Meunier and Hovius 2006; Chang et al. 2007; Lin et al. 2008). Earthquake-triggered

landslides are commonly found at ridge crests due to the topographic amplification of seismic waves (Lin et al. 2006). Densmore and Hovius (2000) suggest that co-seismic shaking also causes failure at hillslope toes resulting in a notable uniform distribution of steep slopes. Their investigations into mountain ranges where storms are the dominant trigger (i.e. NW California), revealed steep slopes in the lower part of the hillslope. Whilst these conclusions are not disputed, other studies show spatial variations in results: storm-triggered landsliding in the Southern Alps, New Zealand exhibit a more uniform distribution over the slopes when compared with earthquake-triggered landslide data from California (Meunier and Hovius 2006); and post-earthquake, typhoon-triggered landsliding in Taiwan preferentially occurred near to stream channels and followed patterns of co-seismic distribution (Chang et al. 2007; Lin et al. 2008). However patterns of pre-earthquake, storm-triggered landsliding in Taiwan follow the method proposed by Densmore and Hovius (2000) and primarily occur in low positions on the hillslopes (Lin et al. 2008). Clearly this remains an open debate and one which this research will investigate for the Sichuan region.

2.2. Landslide inventory mapping

Overview

In order to investigate the controls, characteristics or distribution of landslides, as discussed, knowledge of landslide location is essential. Following a large event such as a high magnitude earthquake, where landsliding occurs over a vast spatial area, an inventory map delineating failures is needed “as the most basic element of any landslide assessment” (McKean and Roering, 2004), providing an overview of landslide distribution in an accessible and useable format. Based on the interpretation of imagery, ground surveyed data and historical databases, landslide inventory maps are a straightforward approach to hazard assessment (Metternicht *et al.*, 2005). They also enable the application of remote sensing techniques to change detection through image classification (Cheng and Chang, 2004).

Slope failures can be identified in satellite images and aerial photographs (see Figure 2.2) due to the spectral properties of landslide scars (De La Ville *et al.*, 2002). This bare ground that remains following the removal of material has a higher reflectance than vegetation at most wavelengths (Figure 2.3) and therefore appears very bright in contrast to surrounding vegetation in the image (as seen in Figure 2.2). Cognitive recognition allows the human eye to distinguish between slope failures and other surfaces that also appear bright, i.e. roads and buildings, according to other visual characteristics of slope failures (Table 3.1). Consequently

manual mapping of slope failures is a common method for producing an inventory following an event, especially when field investigations may not be possible due to limited access and the wide coverage of failures. Huang and Li (2009a) provide an example of where this has been done following the Wenchuan earthquake. Whilst this is recognised as an effective and accurate way of identifying slope failures, it is also extremely time- and labour-intensive and thus a faster methodology based on satellite imagery is desirable (Nichol and Wong, 2005). For an event such as the Wenchuan earthquake where over 100,000 landslides have been identified (Parker, 2010), a significant amount of time would be required for manual mapping, thus reducing the value of the data.

Maps of slope failures are employed for a variety of purposes including identifying hazardous areas; providing scientific information for decision-making; analysis of distribution patterns and the controls upon this, and many more (Galli *et al.*, 2008). In all these things, the sooner the information is available then the more effective the analysis and following actions will be. As a response to this demand, automated mapping techniques have been developed allowing maps and inventories of slope failures to be produced quickly and effectively after an event. Following the Wenchuan earthquake a variety of automated techniques were used to map co-seismic slope failures, alongside manual mapping (Sato and Harp, 2009) and field investigations (Huang and Li, 2009a). For example, Parker (2010) developed an automated classification that utilised a selection of satellite imagery collected in June 2008 covering the entire rupture zone. The final map can be seen in Figure 2.4 along with a map produced by Huang and Li (2009a): whilst the latter map (Figure 2.4b) has a much smaller spatial coverage than Figure 2.4a it has the advantage of combining field investigations with automated mapping from aerial imagery.

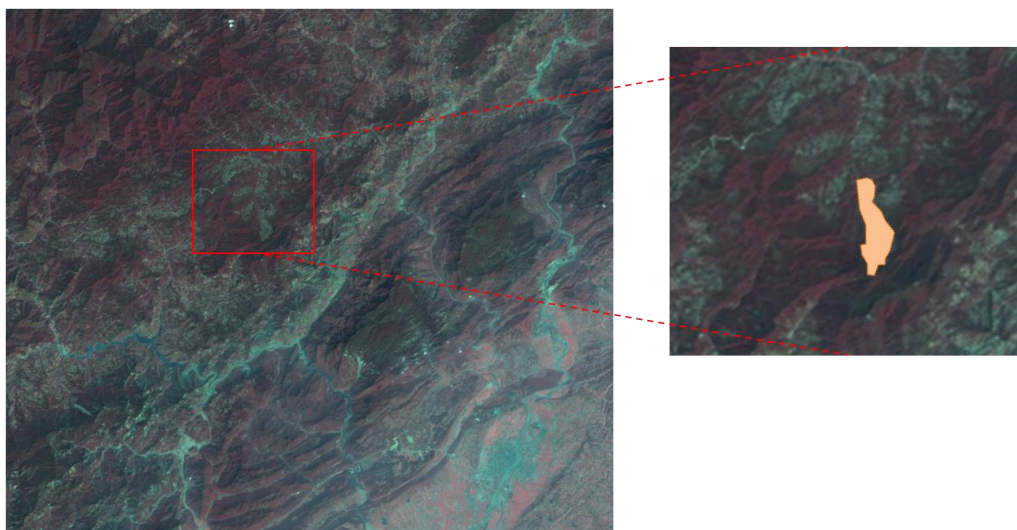


Figure 2.2: An example of identifying slope failures from satellite imagery (SPOT 5 multispectral).

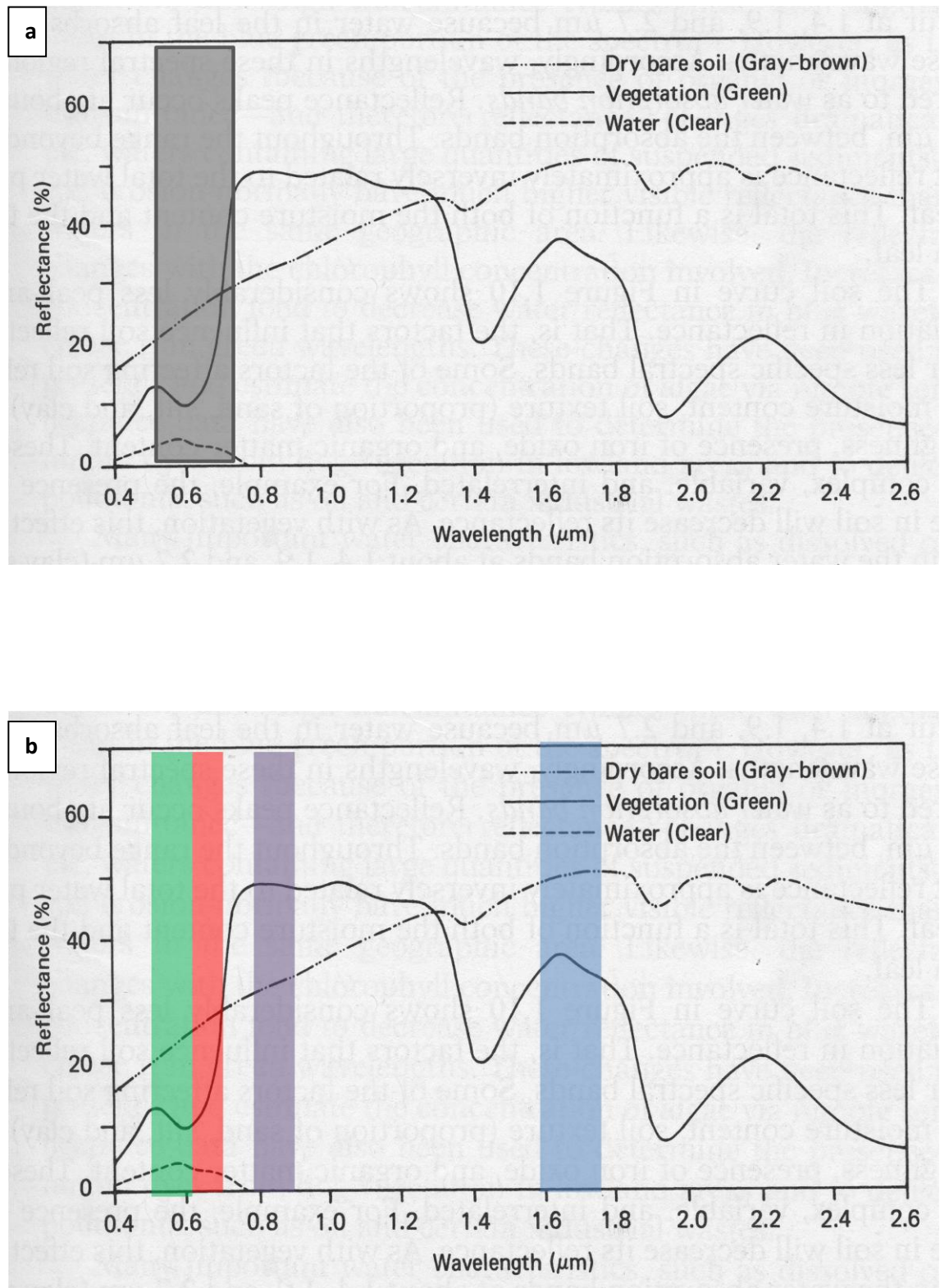


Figure 2.3: Typical spectral signatures of bare soil, vegetation and water (taken from Lillesand and Keefer, 2004). **a:** The SPOT 5 panchromatic band is shown in grey; **b:** The SPOT 5 multispectral bands are shown as follows: Green = Green; Red = Red; Purple = NIR; Blue = MIR.

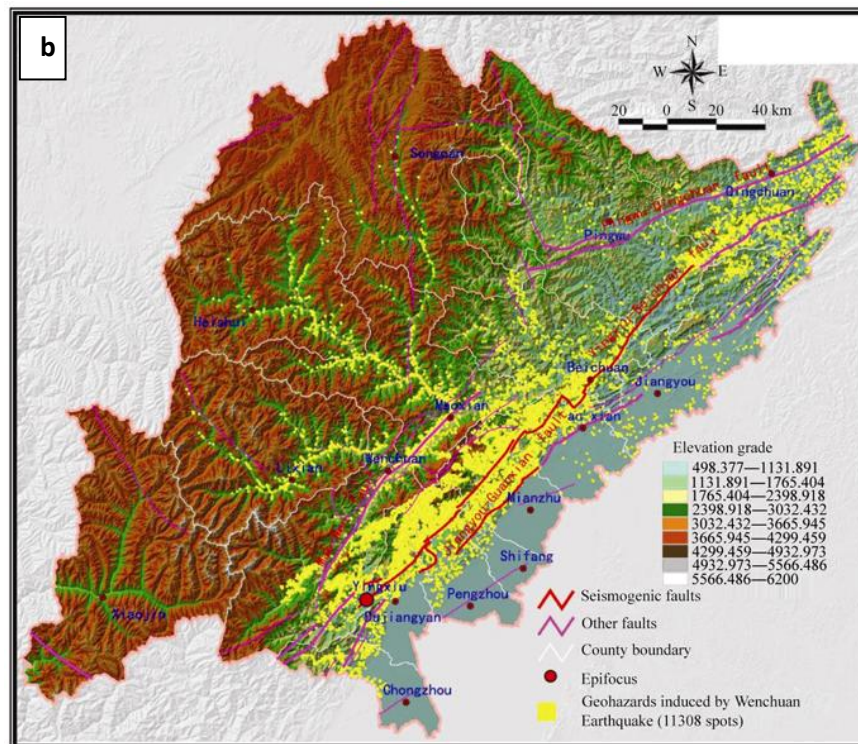
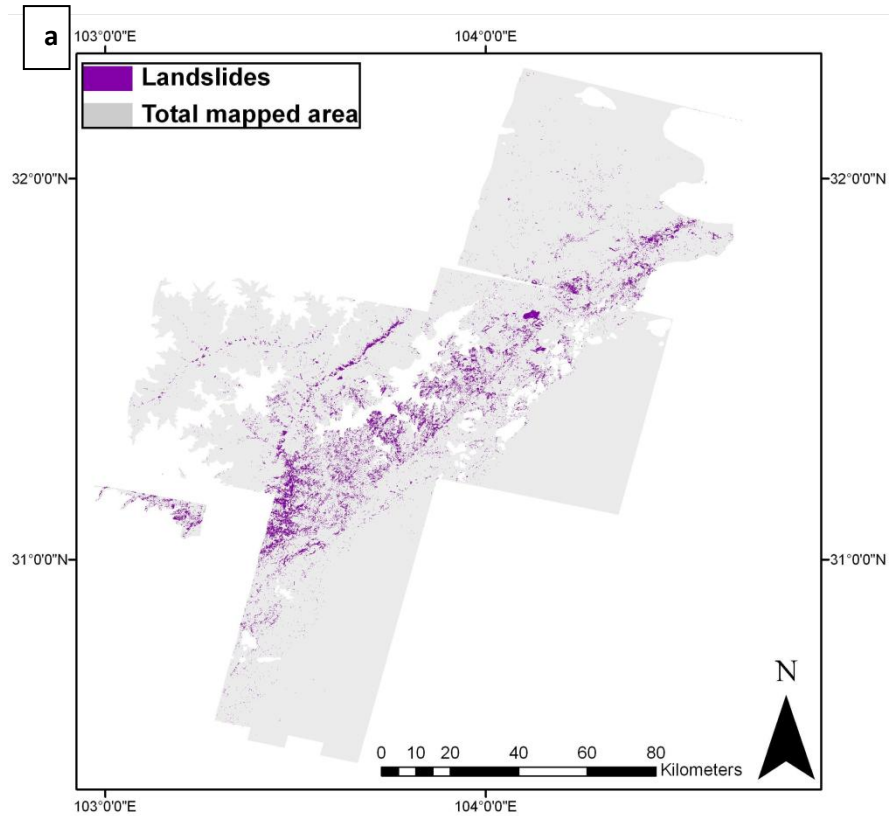


Figure 2.4: Examples of landslide inventory maps produced following the 2008 Wenchuan earthquake. **a:** produced by Parker (2010); **b:** produced by Huang and Li (2009a).

Purpose

As mentioned, slope failure inventory maps are used in a variety of ways. Primarily they provide an indication of the areas susceptible to landsliding, based on the notion that landslides are more likely to occur in places where they have occurred previously (Nichol and Wong, 2005) and under conditions which led to past instability (Guzzetti *et al.*, 1999). In order to fulfil the aims and objectives of this research project, inventory maps have provided a tool for analysis of the landslide failures, i.e. the source of material. Maps have been produced using satellite images from June 2008, October 2008 and March 2009, primarily to assess the temporal changes in landslide distribution and consequently the controls upon the mobilisation of debris released by landslides.

2.3. Sediment volume estimations

As outlined in the Introduction, the numerous hazards associated with landsliding mean that it is crucial to understand the processes and improve upon assessments of their impact. Quantifying the volume of sediment displaced by landslides is one aspect of this, which continually re-appears in the literature as more accurate and applicable methods are sought to enable post-earthquake impact assessment. Table 2.1 lists some examples of studies and the formulas that they have derived for volumetric estimation (see Guzzetti *et al.*, 2009 for a more comprehensive review). Whilst there are advantages and disadvantages to all, the most recent study (Guzzetti *et al.*, 2009) arguably provides the best formula. Firstly it is based on a worldwide catalogue of 677 landslides, rather than data from just one or a few regions; secondly it is applicable to landslides with a large range of areas ($2 \times 10^0 \leq A_L \leq 1 \times 10^9$); and thirdly it is largely independent of the physiographical setting, making it applicable to many future landslide assessments. Results from application of the formula to the Collazzone area, central Italy are correlated to event magnitude and landslide mobilization rates (Guzzetti *et al.*, 2009); this builds on the work of Malamud *et al.* (2004a), which related the predicted total volume of mass wasting to the landslide-event magnitude. Such findings aid assessments of the impact of landslides both as a hazard and as a long-term geomorphic process in landscape evolution (Korup *et al.*, 2009).

Table 2.1: Formulas for estimating landslide volume V_L

The formulas in column 3 derive landslide volume (V_L in m^3) from landslide area (A_L in m^2). Malamud *et al.* (2004) use V_{LT} (total landslide volume) and N_{LT} (total number of landslides); in the formula from Hovius *et al.* (1997; 2000) β is a scaling exponent, ϵ is a landslide width-depth scaling coefficient, L_1 is the upper length scale for the process in the region, and A_d is the area drained

Literature	Data source	Formula	Conditions
(Guzzetti <i>et al.</i> , 2009)	Worldwide catalogue of 677 landslides	$V_L = 0.074 * A_L^{1.450}$	➤ $2 * 10^0 \leq A_L \leq 1 * 10^9$
(Imaizumi and Sidle, 2007)	Miyagawa Dam Catchment, Japan	$V_L = 0.39 * A_L^{1.31}$	➤ Valid for shallow landslides ➤ $1 * 10^1 \leq A_L \leq 3 * 10^3$
(Malamud <i>et al.</i> , 2004b)	Northridge, California; Umbria, Italy; Guatemala	$V_{LT} = (7.30 * 10^{-6}) N_{LT}^{1.122}$	
(Martin <i>et al.</i> , 2002)	Queen Charlotte Islands, British Columbia	$V_L = 1.0359 * A_L^{0.880}$	➤ $2 * 10^2 \leq A_L \leq 5.2 * 10^4$
Hovius <i>et al.</i> (1997; 2000)	Southern Alps, New Zealand	$V_L \sim ((2\beta\epsilon\kappa)/(3 - 2\beta)) * L_1^{3-2\beta} A_d$	➤ Assumes a linear width-depth relationship

2.4. Transfer of material through the catchment

The movement of material through a catchment relies on sediment mobilisation and a strong hillslope-fluvial coupling. Just as landslides are recognised as playing a vital role in mountain landscape evolution (Densmore *et al.*, 1997; Meunier *et al.*, 2008), the flux of sediment is equally important to ensure the transfer of mass downstream and back into the processes of mountain building (Hovius *et al.*, 2000). Thus, there is a need for a clear understanding of both sediment mobilisation and hillslope-fluvial coupling. Figure 2.5 introduces a flow diagram which conceptually describes this movement of sediment through a typical catchment. This is used as a basis for discussing some of the topics below and re-appears throughout this study to illustrate the contribution of knowledge at each stage.

2.4.1. Sediment (re)mobilisation: controls and characteristics

Initial mobilisation of sediment due to landsliding has already been discussed (section 2.1) and therefore this section will principally focus on the remobilisation of sediment post-earthquake. As previously mentioned, earthquakes destabilise the ground leaving significant potential for slope failure (Matsuoka *et al.*, 2008). Therefore when a trigger occurs, such as a large

rainstorm, seismically loosened sediments are mobilised again (Lin *et al.*, 2008). This is displayed most clearly by the 1999 Chi-Chi earthquake in Taiwan: one of the main findings of research following this event was the post-seismic failure of many hillslopes, which had been weakened by seismic activity (Dadson *et al.*, 2004; Lin *et al.*, 2006). Triggered by a typhoon, the failures produced enhanced concentrations of suspended sediment flux for five years (Lin *et al.*, 2008) and similar patterns of remobilisation are being seen in Sichuan.

Recent work in hydrology suggests that hillslope sediment inputs to a river system exert a strong control on the grain size of sediment contained within the river (Sklar *et al.*, 2006; Sklar and Dietrich 2008). From this it can be deduced that grain size distribution (GSD) must be a factor of sediment mobilisation and transport on hillslopes. This theory is reinforced in the findings of many geomorphic studies that provide evidence for size selective transport of materials associated with landsliding (Pearce and Watson, 1986; Fan and Cai, 2005; Peart *et al.*, 2005). Despite this evidence, the majority of work on mobilisation of landslide sediments into the fluvial system ignores the GSD of landslide materials. Sklar *et al.*, (2006) highlight the need for both data and theory that can be used in predicting the GSD of hillslope sediment supply to channels.

2.4.2. Hillslope-fluvial coupling

In a recent study Korup *et al.*, (2009) highlighted the often assumed view that in the hillslope-fluvial coupling, the fluvial controls the hillslope. Their review of landslides in mountain range evolution provides support for the alternative view that the hillslope (landsliding) exerts a direct geomorphic control on the fluvial network (Hovius *et al.*, 1997; Korup *et al.*, 2004). This is supported by a range of studies that have attempted to constrain the impact of hillslope mass wasting on sediment transport, exploring controls on the processes involved (i.e. Pearce and Watson, 1986; Hovius *et al.*, 2000; Dadson *et al.*, 2004; Imaizumi and Sidle, 2007).

In one of the first studies to quantify the link between earthquake-induced landslides and sediment transport, Pearce and Watson (1986) examined the sediment delivery from landslides into main river channels in the Southern Alps, New Zealand. Whilst the study may not have been very well constrained, it served to highlight issues of sediment storage times and the influence of grain size distribution, which are still open to debate within the literature. It also importantly concluded that not all landslides deliver sediment to the drainage network – this is imperative for sediment transfer and an issue that other studies have sought to understand. Imaizumi and Sidle (2007) examined the mobility of landslides and derived four classifications that displayed the ‘connectedness’ of landslides with the channel (Figure 2.6) based on their position within the network. This idea that the location of a landslide on the hillslope might affect the probability of it delivering to the fluvial system appears a justified

conclusion in current literature (Hovius *et al.*, 2000; Lin *et al.*, 2008), however patterns of landslide locations with respect to the river network are still poorly constrained (Dadson *et al.*, 2004).

Attempts to quantitatively assess the impact of seismically-induced landsliding on the fluvial system have primarily focused on sediment concentration in low-order river channels (Hovius *et al.*, 1997; Dadson *et al.*, 2004; Lin *et al.*, 2008) however it is questionable whether these truly reflect the stochastic and complex nature of sediment routing (Hovius and Stark, 2002). Other approaches include simple equations to balance the input and output of sediment: “total landslide volume – deposition in scars = amount lost to the fluvial system” (Peart *et al.*, 2005); and a general notion that measures of aggradation and deposition provide quantification of an earthquake’s impact (Lin *et al.*, 2006). Whilst these are all valid to an extent and contribute significantly to our understanding of the processes, they produce a ‘black-box’ approach to understanding sediment transfer, assuming that all material passes directly into the fluvial system and ignoring the probable mismatches and spatial variation between supply and transport (Korup *et al.*, 2009) as illustrated by Figure 2.5.

This issue has briefly been explored in Taiwan (Hovius *et al.*, 2000) and the 1999 Chi-Chi earthquake provided an ideal opportunity to explore hillslope-fluvial coupling in a co-seismic and post-seismic setting (Meunier *et al.*, 2007; Meunier *et al.*, 2008). This contributed considerably to the understanding of earthquake-induced landsliding and associated sediment flux. With respect to hillslope-fluvial coupling, key findings include the notable spatial variations in the impact of landsliding on downstream sedimentation (Lin *et al.*, 2006; Shou *et al.*, 2009); the differences in grain size distribution between the landslide, hillslope and channel bed (Chen and Wu, 2009); and a 2-fold increase in sediment discharge following post-seismic landsliding (Chuang *et al.*, 2009). A significant advance in many of the Chi-Chi studies was that issues were addressed over a range of scales, providing a better indication of overall system response.

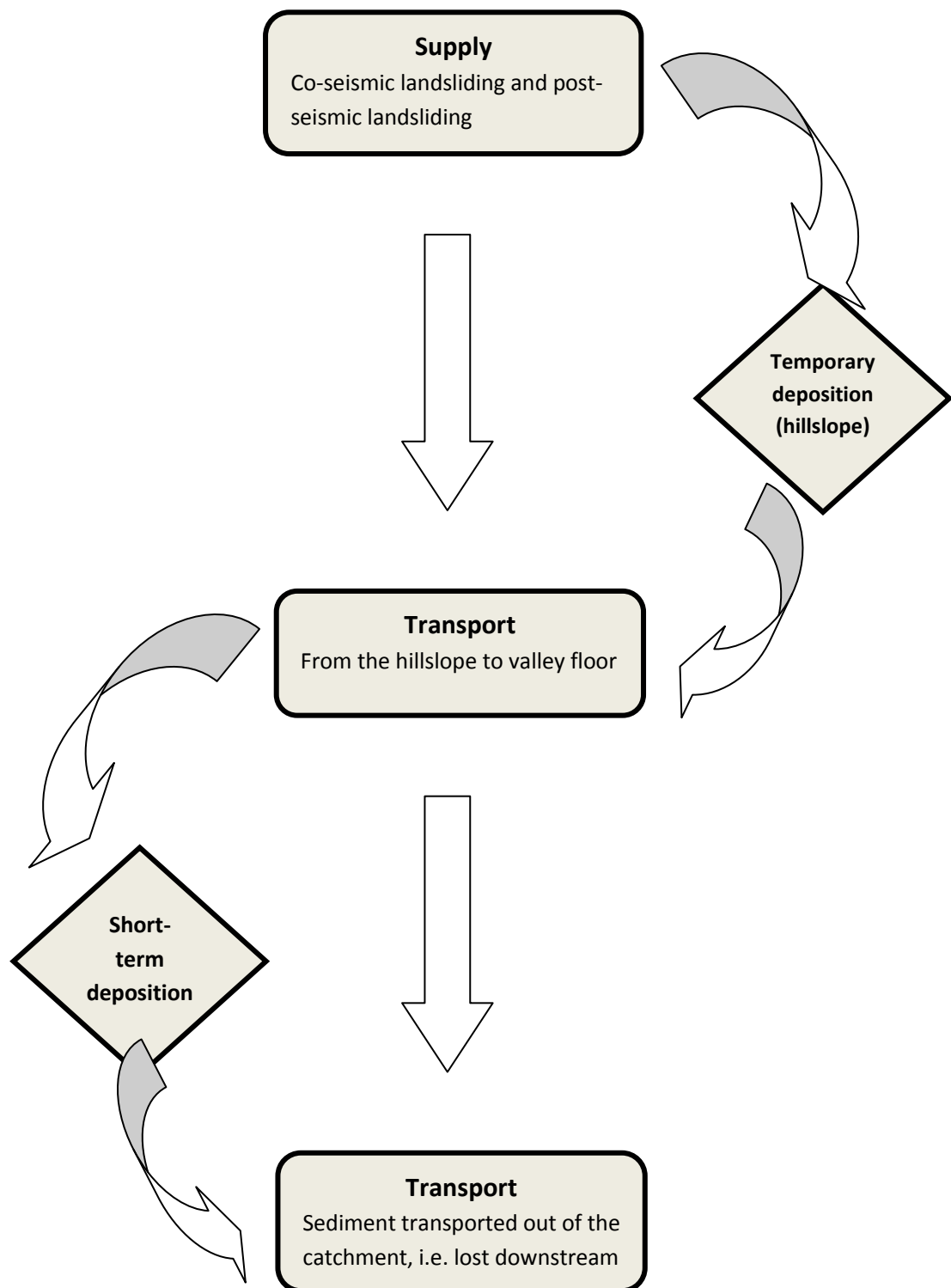


Figure 2.5: Flow diagram of sediment movement through a typical catchment.

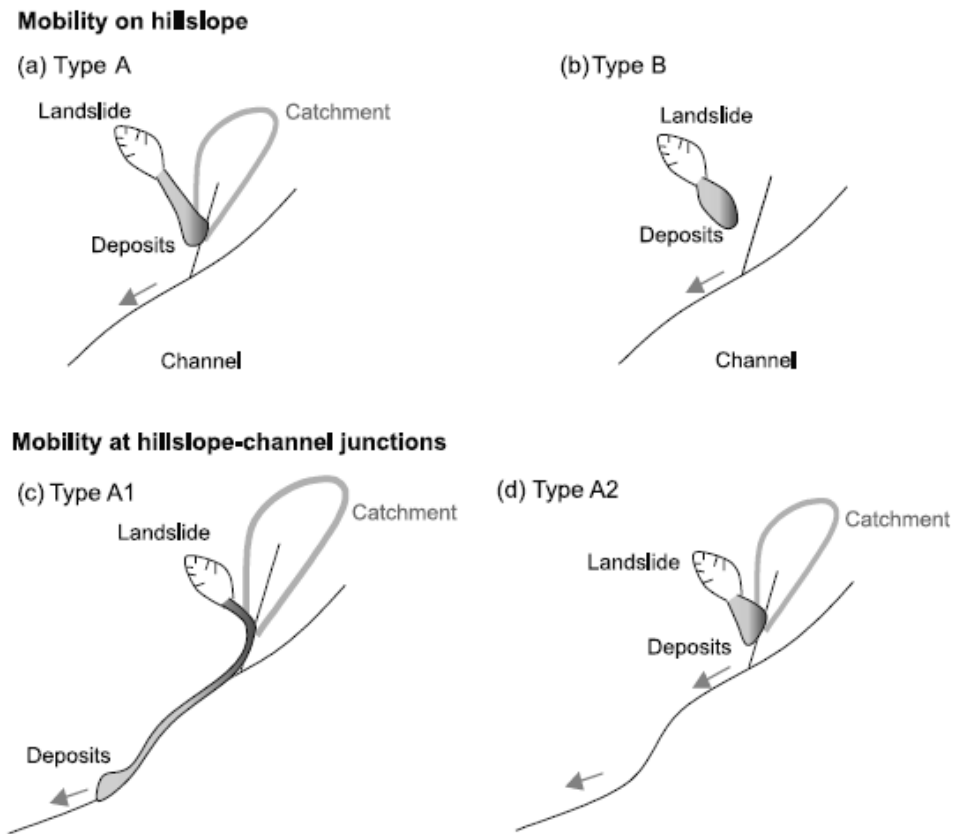


Figure 2.6: Classification of landslides on the basis of position and mobility of sediments (after Imaizumi and Sidle, 2007)

2.5. Summary of research gaps

As the previous discussion has shown, a body of research that has expanded over the recent decades focuses on the current understanding of seismically associated landsliding and sediment dynamics throughout the catchment. However there are still many open debates and notable gaps in our understanding of these processes.

2.5.1. Landslides – the sediment source

The ability to accurately quantify the volume of sediment displaced by landslides (Figure 2.5: supply) is a problem encountered in many studies and new methods/formula are continually sought out (Guzzetti *et al.*, 2009). Large variations arise between different spatial and temporal scales; therefore an increase in investigations which test and develop these methods over a range of scales will enhance accuracy of calculations and understanding of the governing processes.

Despite the evidence for size selective transport, the GSD has often been ignored in studies of landslide material. Research following the Chi-Chi earthquake, Taiwan did examine this and found clear differences in GSD between the landslide, hillslope and channel bed (Chen and Wu, 2009). This should motivate future studies to ensure that the type and composition of material is not ignored in landslide analysis.

2.5.2. Hillslope-fluvial coupling

Spatial patterns of landslide locations with respect to the river network are poorly constrained (Dadson *et al.*, 2004) despite awareness that landslide location most likely affects the delivery of material to the fluvial system (Imaizumi and Sidle, 2007). Following this, the 'black-box' approach to understanding sediment flux through a landscape fails to consider the spatial and temporal variations that exist in the movement of material on a hillslope and within a river system (Korup *et al.*, 2009). There is a pressing need to examine the transfer of material at each stage through the catchment (Figure 2.5: transport), with particular focus on the sediment flux between the landslide and the channel (Chuang *et al.*, 2009). This should be examined not only to further understanding of sediment transfer, but also due to the implications that this has for changes in sediment storage within a mountain belt (Korup *et al.*, 2009).

The approaches taken in studying these processes has led to a narrowed understanding, restricted to certain spatial and temporal scales. The extension of knowledge into different environments will serve to address some of these research gaps simply by increasing the wealth of information (Guzzetti *et al.*, 1999). Certain issues, such as the transfer of sediment and effects on the fluvial system, require consideration over smaller spatial scales in order to improve our understanding of processes at each stage in the system (Hovius *et al.*, 2000).

3. Landslides: the source

3.1. Methodology

3.1.1. Resources

Imagery

In order to produce an inventory map of slope failures, high resolution satellite imagery is required (Metternicht *et al.*, 2005). Satellite imagery is chosen above other types as it is cheaper and more extensive than aerial imagery and doesn't encounter the geometric problems that radar imagery often does in areas of steep terrain (Lillesand and Keefer, 2004). Whilst a broad range of satellite imagery exists, this research is restricted by the specific spatial and temporal coverage desired and therefore uses SPOT 5 imagery available at 5 – 10m resolution in panchromatic and multispectral formats for a variety of dates since the earthquake in May 2008. A review of the range of satellite imagery available for the area deemed SPOT 5 to be the most favourable balance between cost, coverage and resolution (Parker, 2010). Previous studies also confirm the reliability of SPOT imagery for landslide mapping: Nichol and Wong (2005) stated that approximately 70% of landslides were identified from a 20 m resolution SPOT multispectral image.

The three images used are shown in Figure 3.1, along with a map of the earthquake rupture zone. As can be seen, the spatial coverage of the images is fairly small in comparison to the total affected area. However, the region covered is seismically very significant because here the faulting mechanism changes from predominantly thrust faulting in the south-west to dominantly dextral (strike-slip) faulting in the north-east (Shen *et al.*, 2009). Consequently the ground acceleration was very high in this area and thus high landslide density is also to be expected (Chen *et al.*, 2009; Meunier *et al.*, 2007). In addition, the images provide good temporal coverage, which is essential in order to explore landslide failure evolution. The three images were acquired in June 2008, October 2008 and March 2009 respectively.

To afford the beneficial aspects of this imagery, as outlined above, there are some limitations to account for. These are described below along with measures taken to reduce their affect on the results:

- **Using a combination of imagery**

Due to the availability of imagery for the study area and resources available, the October image (S2) is in panchromatic format, unlike the June (S1) and March (S3) images, which are in multispectral format. The S1 and S2 images are also at a higher resolution of 5 m compared to the S3 image, which is at 10 m resolution.

As a result of the different formats, image S2 required a different method of classification (see section 3.1.2), which must be accounted for when analysing and comparing the landslide map inventories. Further, towards the upper end of the panchromatic band wavelength range (0.48 – 0.71 μm), the spectral signature of bare soil has a lower reflectance than vegetation (Figure 2.3). Consequently there are some failures identified in both the June and March images that are not clearly visible in the October image (Figure 3.2). This gives a false impression of re-vegetation between June and October.

- **Restricted areas**

Due to the climatic conditions of the Sichuan region, cloud and haze free imagery is very difficult to obtain. The region experiences both the Southeast Pacific Ocean monsoon and the Southwest Indian Ocean monsoon and, due to its location at the edge of the Tibetan Plateau, high levels of orographic rainfall are common. This problem could usually be overcome by selecting imagery from a time not affected by the monsoon, however as a temporal range of imagery was desired then the appearance of clouds and haze was unavoidable. Where clouds were present then this area of the imagery had to be removed from the analysis as it is impossible to delineate the slope failures beneath the cloud. As a result the area of imagery available for analysis was edited to not include any areas covered by haze or cloud in any of the three images. The final area of available imagery is shown in Figure 3.3.

DEM

The most recent global digital elevation model (GDEM hereafter) was used to provide a topographic basis for spatial analysis, allowing landscape characteristics (i.e. slope, aspect, elevation) to be considered. The ASTER GDEM utilises scenes from the ASTER Visual and Near Infrared image archive, to create the model (NASA, 2009). With a spatial resolution of 30 m, this is significant improvement on preceding DEM data for this region (90 m SRTM), which is important as it will significantly influence the quality and accuracy of the data derived from it (Gallant and Hutchinson, 1996).

Field data

Field site investigations provided an additional resource through enabling the collection of data, which is not available from satellite imagery. A lack of field data can often be a restricting factor in landslide hazard assessment (for example in Zhou *et al.*, 2002) and therefore this study benefited significantly from the following:

- Collecting data to validate methods and techniques used;
- Measurements to ground-truth results from desk-based analysis;
- Further detail on the characteristics of failures, i.e. type of failure, depth etc. This information is very useful as two failures which differ significantly in depth can appear very similar on a satellite image (see Figure 3.4). This has significant implications for analysis, especially volume estimations.

In addition, fieldwork provided an opportunity for analysis beyond the temporal range of the available imagery, i.e. the evolution of failures post-March 2009.

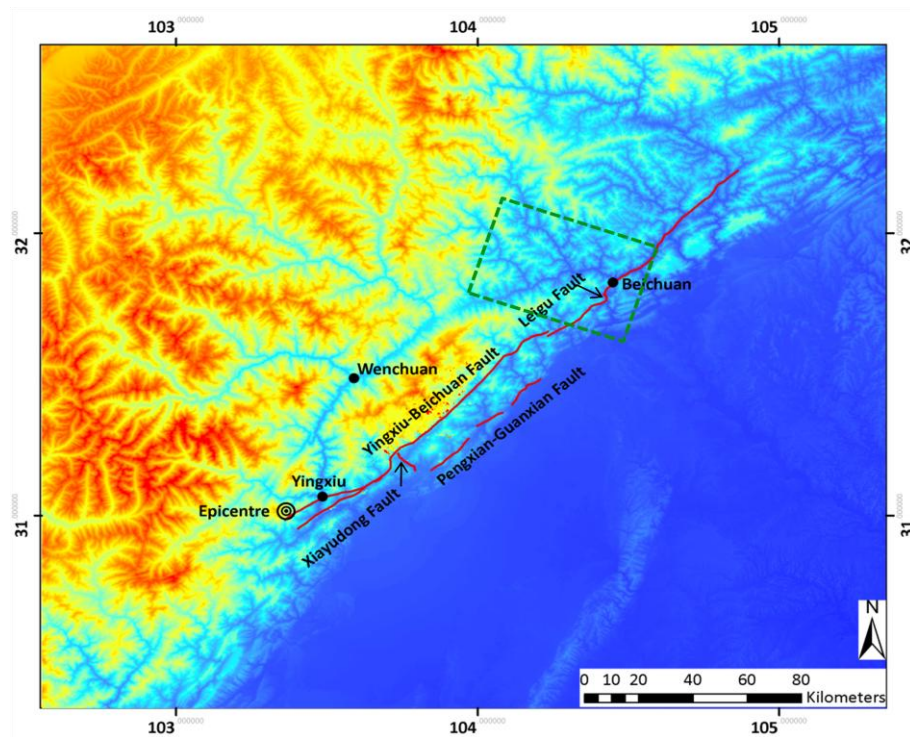


Figure 3.1a: The earthquake rupture zone (GDEM as base map): the fault lines that ruptured during the 2008 earthquake are shown in red (mapped by Densmore *et al.*, in press); the area outlined by the green dashed line represents the area covered by imagery.

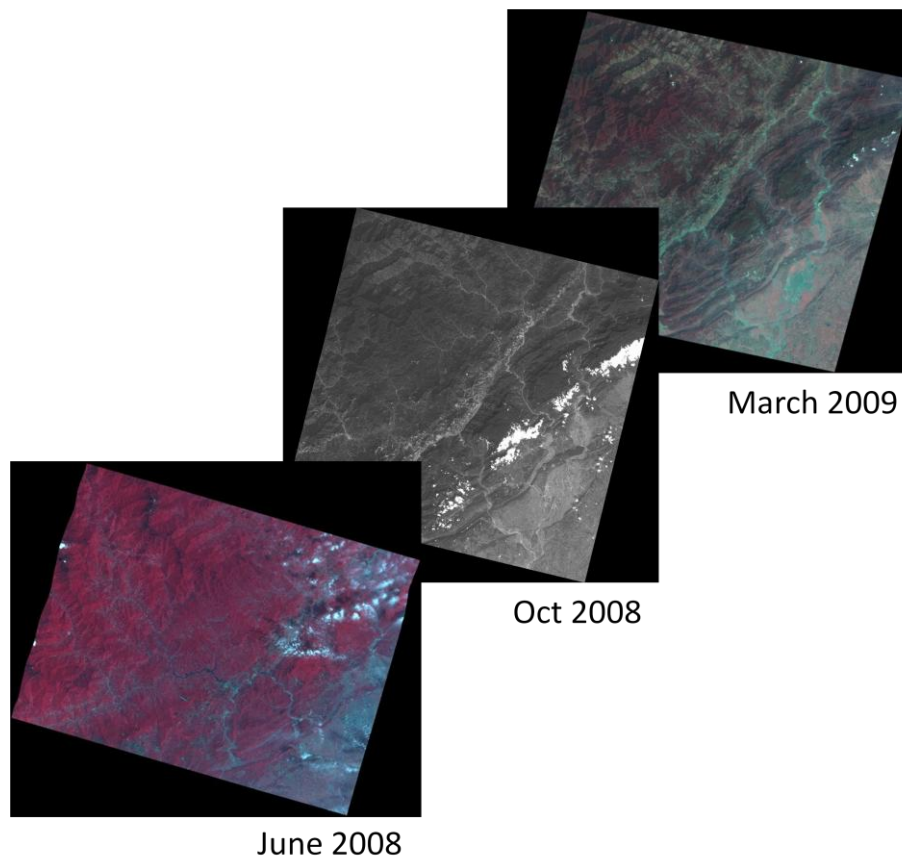


Figure 3.1b: Satellite images (SPOT 5) used for landslide inventory mapping

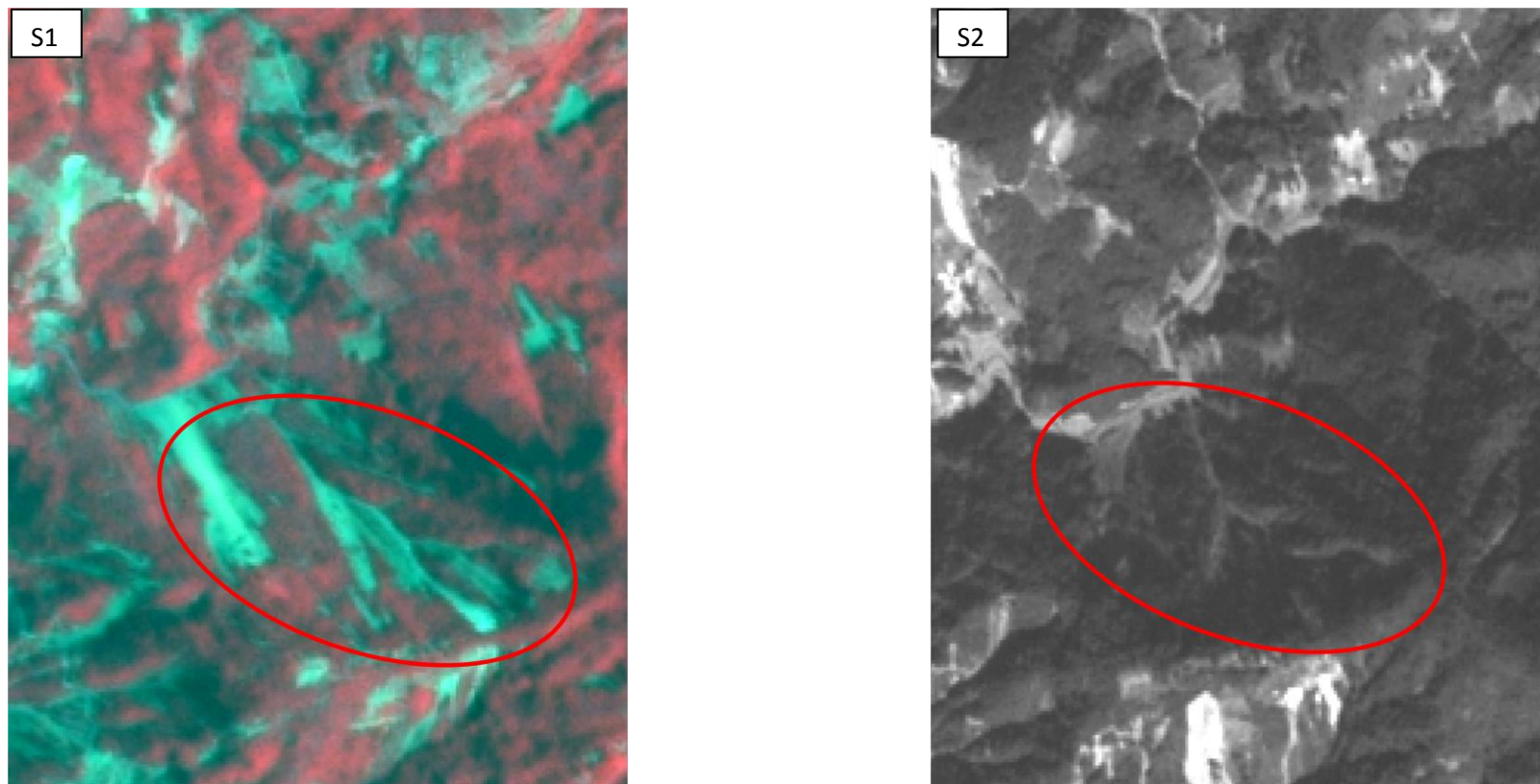


Figure 3.2: Failures clearly visible in image S1 that are not clear in image S2 – area highlighted by red ring.

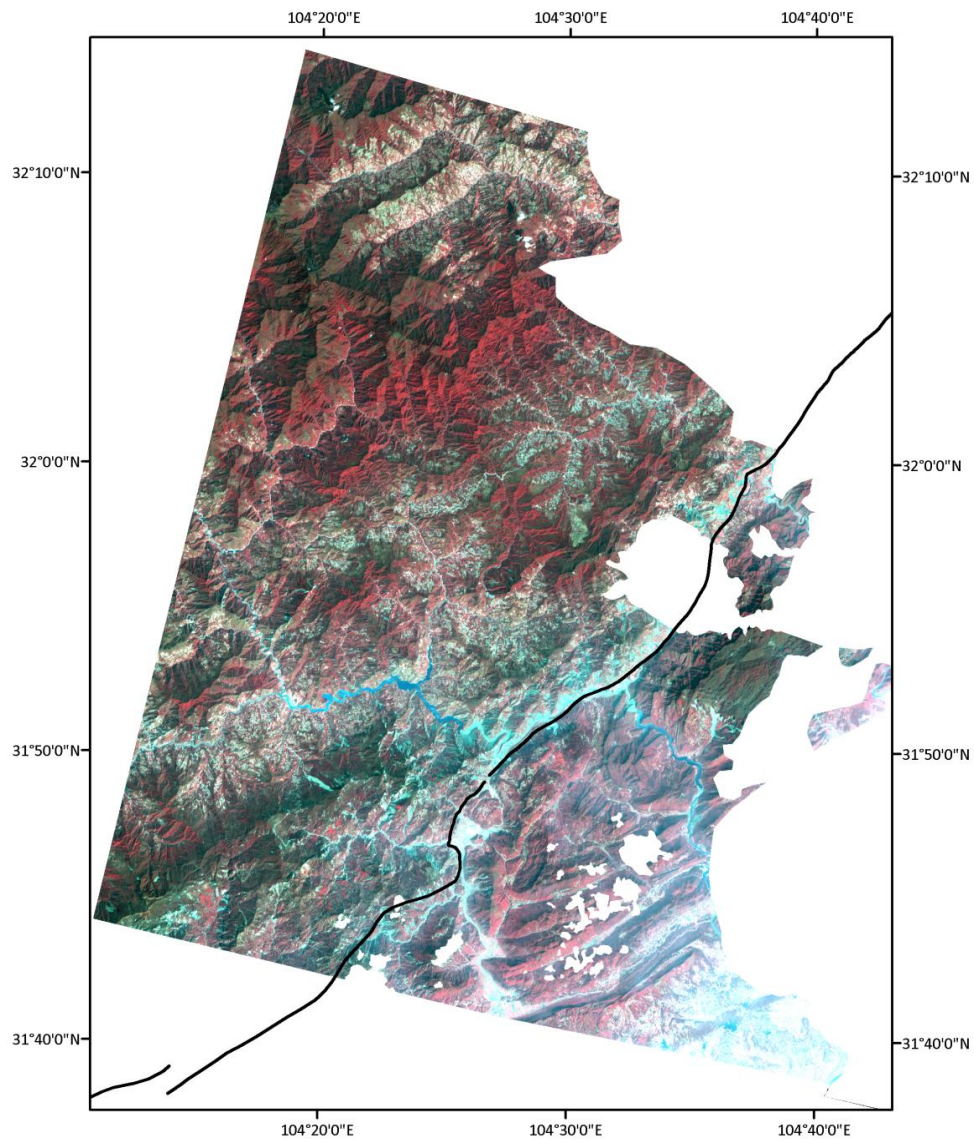


Figure 3.3: Final area of imagery available to be mapped, displayed using image S3. Main fault rupture is shown by the black line.

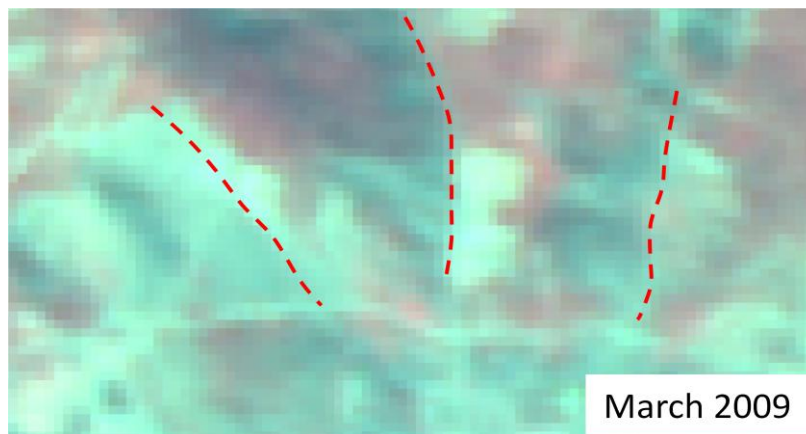


Figure 3.4: The three landslides seen in the satellite imagery (March 2009) all appear similar with no perception of depth; however in the photograph the variation in depth is clear. The red dashed lines represent the ridge lines as seen in the photograph.

3.1.2. Identifying slope failures – automated landslide mapping overview

In order to compare results with previous investigations into post-earthquake slope failure following the 2008 Wenchuan Earthquake, the classification algorithm developed by Parker (2010) was adopted as a general framework for landslide classification. A summary of the main stages in this algorithm are shown in Figure 3.8. Hervás and Bobrowsky (2009) stressed the need for landslide mapping at adequate scales and the application of cost-effective methods: this method responds to that and was chosen because it offered a fast method of accurately delineating slope failures over a large area. Therefore it allowed me to map the landslides at an appropriate scale in the area of imagery available, and its previous application to the Sichuan region ensured reliable and comparable mapping. The automated classification allows for a rapid first-order delineation of landslide areas, whilst providing an opportunity for manual editing beyond this. In the study conducted by Parker (2010), over 100,000 landslides were mapped over a period of weeks. In contrast, a study by Huang and Li (2009), which used manual mapping and field-based surveys, delineated only 11,500 landslides. This made the algorithm ideal for the time constraints on this project, whilst retaining a level of accuracy appropriate for the analysis intended. In addition, this had been developed and used on a range of images including SPOT 5 multispectral and panchromatic imagery, making it applicable to the imagery I have used.

As can be seen in Figure 3.5, a significant proportion of the process requires the judgement of the user, in defining classes that represent landslide areas (stage one – unsupervised classification), in defining the histogram thresholding (stage two – panchromatic band thresholding), and in manual editing (stage three – manual edits). Naturally this introduces a small amount of bias to the mapping procedure and means that the final inventory map produced is unique, even compared to those produced by other workers with the same methods. This is important to highlight and has been considered in the dissection and analysis of results, especially in comparison to other studies. The bias introduced through the unsupervised classification and manual edits is accepted as part of the landslide mapping procedure for the benefits that are offered by these stages; for example, the manual editing process is required to remove false positives that result from the classification (Martha *et al.*, 2010; Borghuis *et al.*, 2007). This is further explained in section 3.1.5. Altering the histogram thresholding can have a significant affect on the number and area of landslides identified; for example, changing the threshold level by +/- 5% produces up to a 16% change in the number of landslides classified. However this is still recognised as the most suitable initial classification for the panchromatic image (Parker, 2010) and thus the level of potential bias is considered in

interpreting the results from this imagery. The following sections describe each stage of the process of creating the landslide inventory map and include amendments made to the original algorithm from Parker (2010). For continuity, image S3 (March 2009) will be used to display all examples of each stage of classification, with the exception of the initial histogram thresholding, which only applied to image S2.

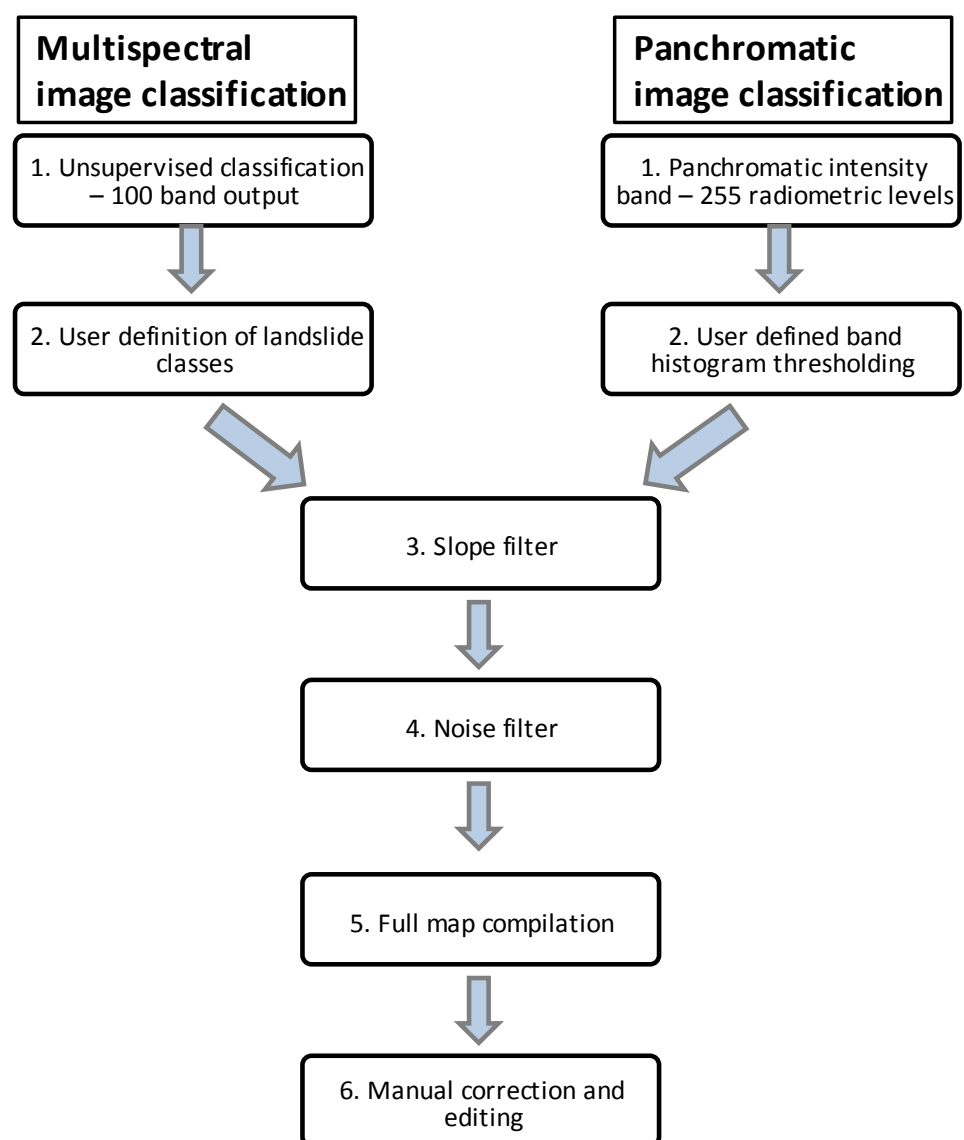


Figure 3.5: Summary of the landslide classification algorithm (adapted from Parker, 2010).

3.1.3. Stage One: Classifications

To account for the different spectral properties of multispectral and panchromatic imagery, different initial methods of classification were used. In the S2 image available for October 2008, landslides appear very bright due to the spectral reflectance properties of bare soil (see Figure 3.2). Therefore gray-level histogram thresholding was used to classify the image into landslide and non-landslide areas. Following visual experimentation with various threshold levels, Parker (2010) suggested that the optimum pixel intensity threshold level for defining landslide areas is ≥ 105 . Similar visual experimentation with threshold levels for the S2 imagery agreed with this suggestion (see Figure 3.6). Using the *Reclassify* function in *ArcMap Spatial Analyst toolbox*, the threshold was applied at a pixel value of 105.

In the SPOT 5 multispectral imagery (S1 and S3) landslides also appear very bright, however due to the combination of four radiometric bands (Green – G; Red – R; Near Infrared – NIR; and Short wave infrared – SWIR), histogram thresholding is not suitable. Instead, a classification that deals with all four bands in combination is required. Therefore an unsupervised classification was produced for S1 and S3 images using the *ERDAS Imagine 9.2* unsupervised classification tool. A total of 100 unsupervised classes were used, offering a suitable compromise between enough classes to pick out detail within the imagery but few enough that the following stage of reclassification is practical and not too time intensive (see Figure 3.7a). Once produced, the classes representing landslides were user-defined through visual comparison of the classified image with the original image. The resulting image was reclassified into a binary raster with landslide cells = 1 and non-landslide cells = 0. This was executed using the *Reclassify* function in *ArcMap Spatial Analyst toolbox* and the resulting raster is shown in Figure 3.7b.

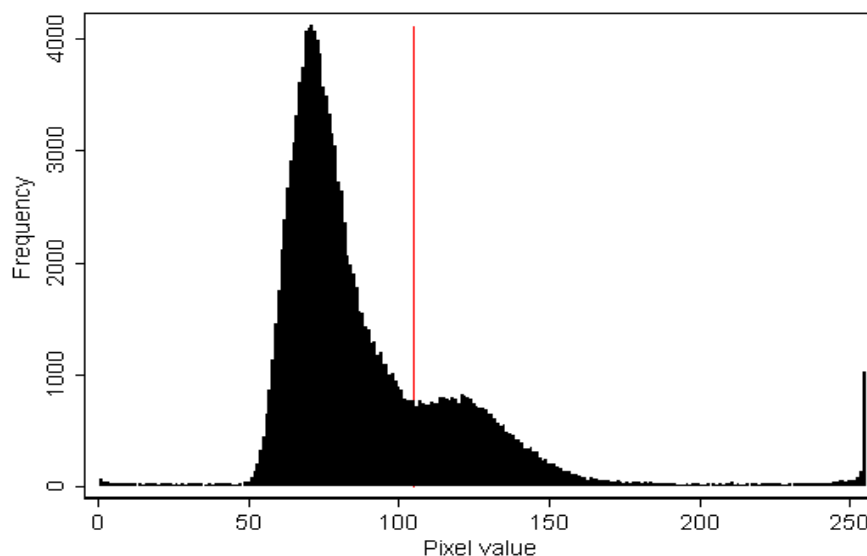


Figure 3.6: Histogram of panchromatic image S2; intensity threshold ($p = 105$) is shown in red.

3.1.4. Stage Two: Slope and noise filters

In the resulting binary rasters it was clear that some areas with similar spectral properties to landslides had been falsely classified as such. For example, roads are also bare ground and thus have a similar spectral reflectance value, causing them to become included in the landslide classes. However such incorrectly identified features can be cognitively recognised by the user due to differences in their appearance compared with landslide features, i.e. shape, position and direction (see Table 3.1). In order to account for these differences and remove the features from the classification, filters were applied to the imagery as suggested by Parker (2010) and shown as stages three and four in Figure 3.5.

Slope filter

Many of the falsely classified features including roads, rivers and buildings, occur on shallow slopes, whereas landslides predominantly occur on steeper slopes. This notion is supported by the results of many previous studies into the controls on slope failure, including those focused on post-earthquake failures (Chang *et al.*, 2007) and those regarding other triggers. For example, Bucknam *et al.* (2001) determined that the main concentrations of landslides following Hurricane Mitch in Guatemala were found on moderate to steep hillslopes. Therefore in order to remove the non-landslide features on lower slopes and retain the landslide features on steeper slopes, a slope filter was applied to the rasters to remove all areas with slope $\leq 20^\circ$. This was selected as the optimum slope threshold because the results matched most closely with visually identifiable landslide areas in the SPOT image. The 30 m resolution ASTER GDEM was used to create a binary slope mask (areas $\leq 20^\circ = 0$ and areas $> 20^\circ = 1$), which was then multiplied with the classification rasters using the *Raster Math* tool in *ArcMap Spatial Analyst toolbox* to remove areas $\leq 20^\circ$ from the classification.

Noise filter

Within the image some individual pixels and small clusters were delineated as landslide features in the classification, however their spatial area makes them too small to be conclusively classified as landslides. To remove these pixels a noise filter was applied based on a technique used by Borghius *et al* (2007), which applied a threshold of three adjacent pixels to landslide mapping (stage four in Figure 3.5). Due to the 10 m cell resolution of image S3, this resulted in a 300 m² noise filter being applied to all three classifications, removing all features smaller than the threshold level. Figure 3.8 displays image S3 following the application of both slope and noise filters.

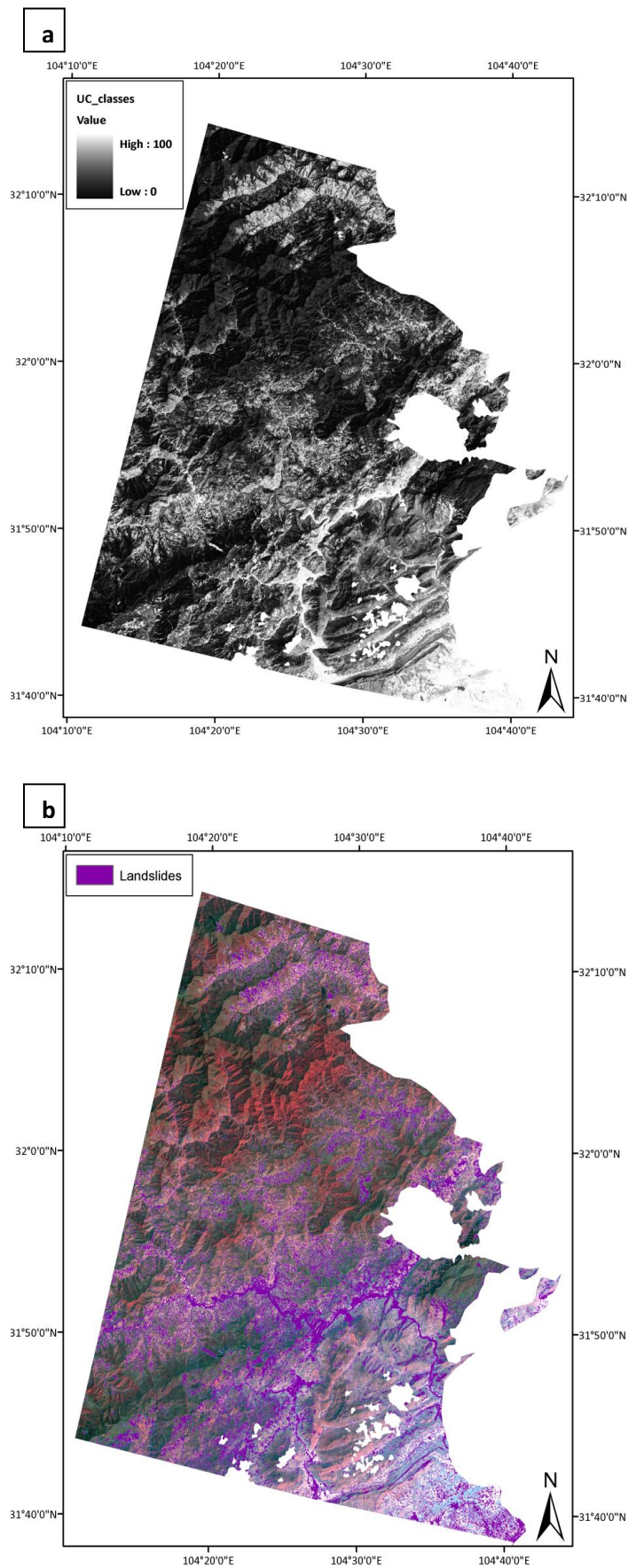


Figure 3.7: Unsupervised classification – **a:** 100 classes produced from the unsupervised classification of image S3; **b:** the resulting raster following reclassification of **a**.

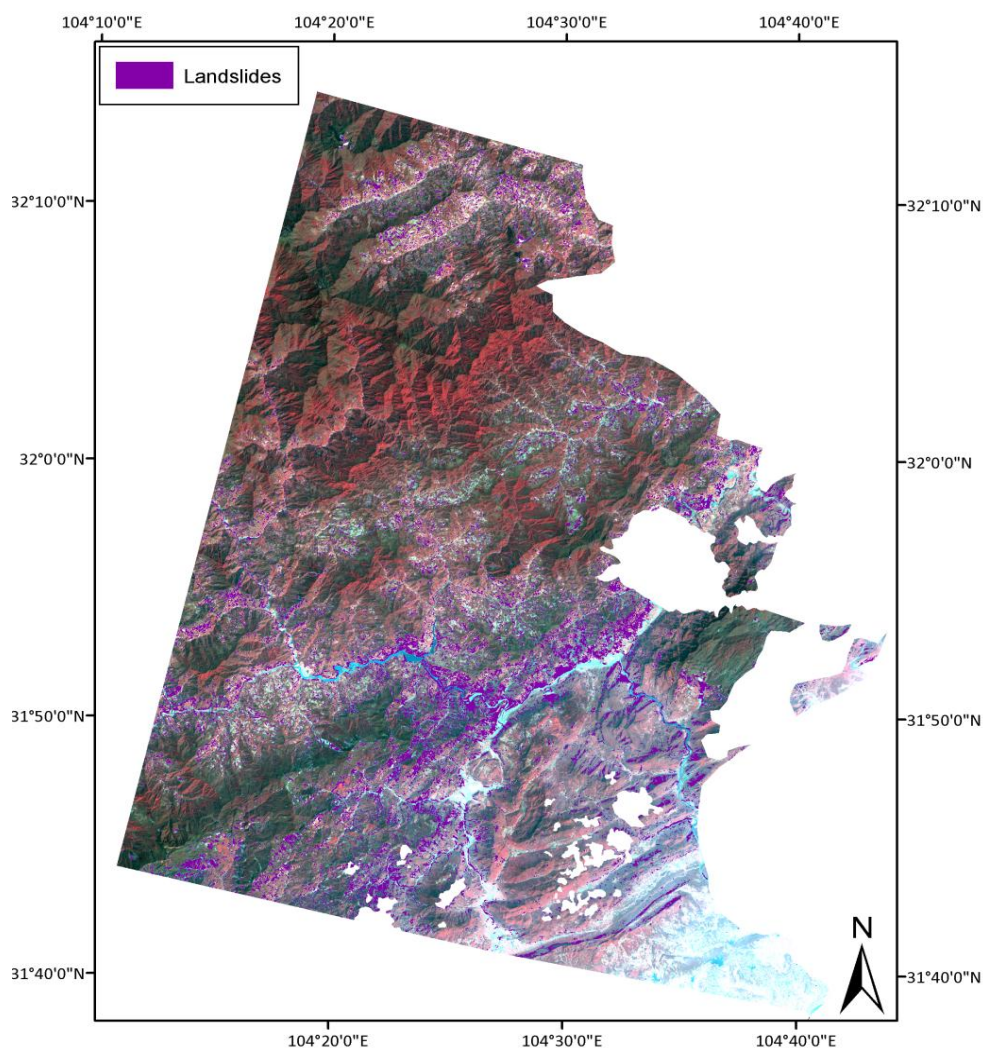


Figure 3.8: Raster of slope failures following the application of slope and noise filters (as identified from image S3).

Table 3.1: Parameters for satellite imagery recognition of landslides: adapted from information in Nichol and Wong (2005)

Parameter	Likely characteristics
Colour	Bright: blue-green (multispectral); white (panchromatic)
Shape	Lenticular, spoon-like, tree-like pattern, rectangular or triangular
Shadow	Indicates positions of valleys and ridges
Direction	Long axis along the direction of gravity

3.1.5. Stage Three: Editing

Commission

Despite the use of slope and noise filters, some additional non-landslide features remained in the classification. These included small buildings and roads found on slopes $> 20^\circ$ as well as larger areas of arable fields, which are particularly common in this region and often terraced on steeper slopes. This was a particular problem in the S1 image – acquired in June 2008, as many fields would have been bare ground at this time.

All of these additional non-landslide features can be visually recognised due to clear differences in shape: the often rectangular shape and straight edges of buildings and fields distinguishes them from the more elongated shape and non-uniform edges of landslides (see Figure 3.9a). In addition, roads are clearly identifiable as they align across contour as opposed to the downslope trend or alignment of landslide features.

To ensure a high level of accuracy and precision in removing these features from the classification, manual editing was used. At a later stage this also allowed for field-based knowledge to support the decisions made in delineating features to be removed.

Omission

In addition to incorrectly commissioned features, some areas of omission were found in the classification. These existed where parts of a failure occurred on slopes shallower than 20° and where the automated classification had fragmented failures to account for areas of vegetation, however this vegetation was often part of the failure. Manual editing was used to ‘fill-in’ areas of the landslides that had been removed (see Figure 3.9b), and the resulting classification was reclassified to dissolve any areas of overlap.

Distance buffer

In order to generate results of a high quality it was reasonable to focus upon a small study area and thus it was decided to work within a 40 km wide corridor around the fault in the along-strike direction; this allowed a high accuracy of mapping where imagery was available. The majority of slope failures were contained in this area (88% - Huang and Li, 2009) and therefore it provided a focused study on the area most affected by landsliding in this region during the 2008 Wenchuan earthquake. In order to do this, a 20 km buffer was applied to either side of the fault line and any mapped areas outside of this buffer were removed.

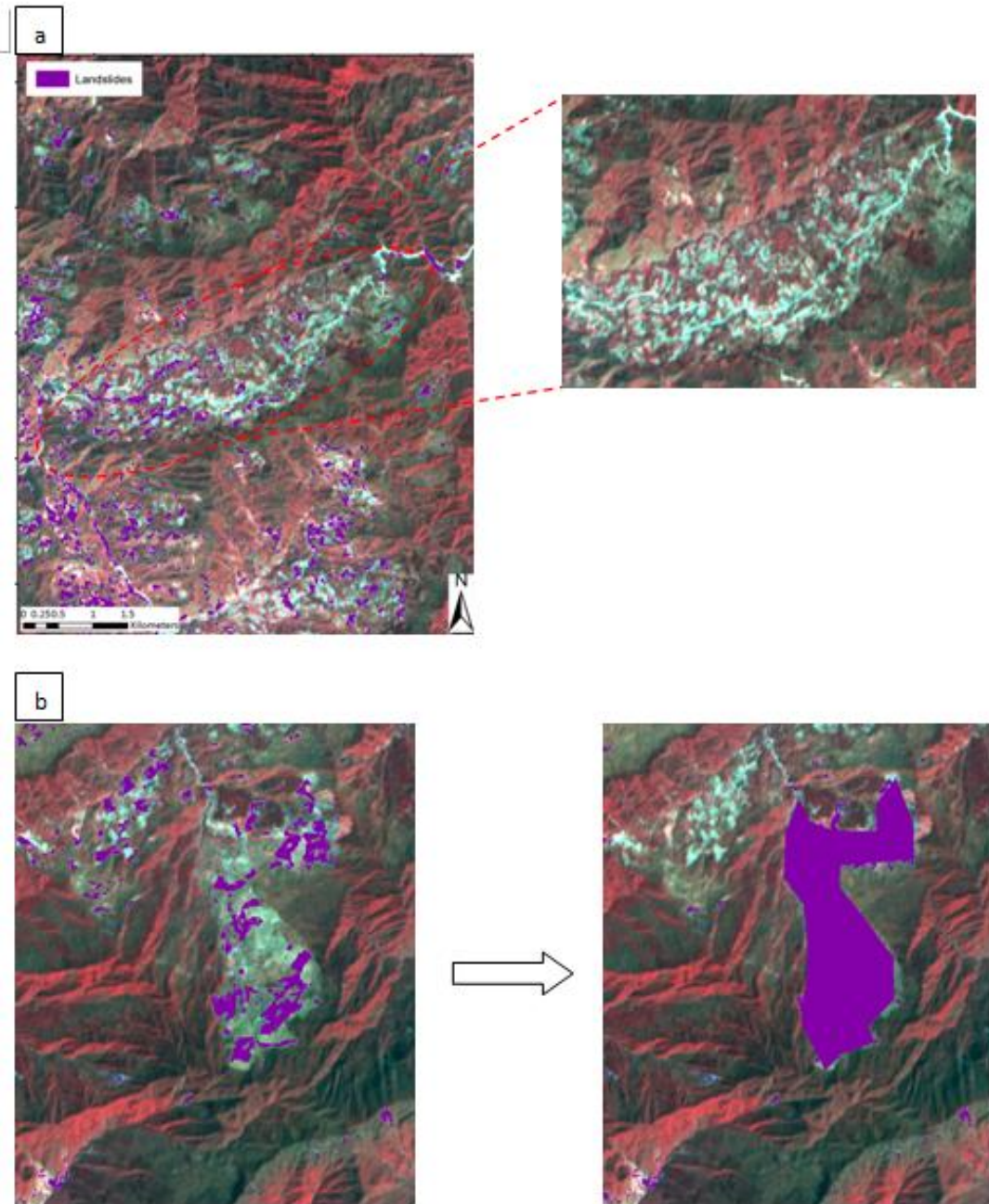


Figure 3.9: Manual editing of landslide features – **a:** areas of commission (in red ring) can be seen clearly as arable fields in the original image; **b:** areas of omission that were filled in

3.1.6. Stage Four: Shadow filter

The final stage of editing to be applied was to areas located on slopes in shadow. The shadow prevented accurate classification due to lowering the pixel brightness values and thus landslide features were unrecognised by the classification methods. To correctly identify areas of shadow, information regarding image acquisition was used to run a hillshade model based on the GDEM in ArcMap, using the *Spatial Analyst: Surface* tools. This created a hillshade map representative of the time at which the image was taken. Figure 3.10 displays the hillshade map produced for image S3, acquired at 3:56 pm on 24/03/2009; the pixels with a value of zero (coded black) are calculated as having been in shadow at that time.

The *Reclassify* function in *ArcMap Spatial Analyst toolbox* was used to reclassify the map into a binary raster (shadow areas = 0 and non-shadow areas = 1), which was used to erase areas in shadow from the landslide inventory map. In order that the resulting three maps may be comparable, any area in shadow of either of the images was removed from all three inventory maps.

Figure 3.11 displays the final mapped area and resulting landslide inventory maps based on images S1, S2 and S3. Following necessary validation and evaluation of the mapping results (section 3.2.5), these maps were used for analysis of the distribution and controls upon post-seismic landsliding as outlined in section 3.2 of this chapter. This responds to research objective 1, which focuses on post-seismic failure evolution (Chapter 1: section 1.2).

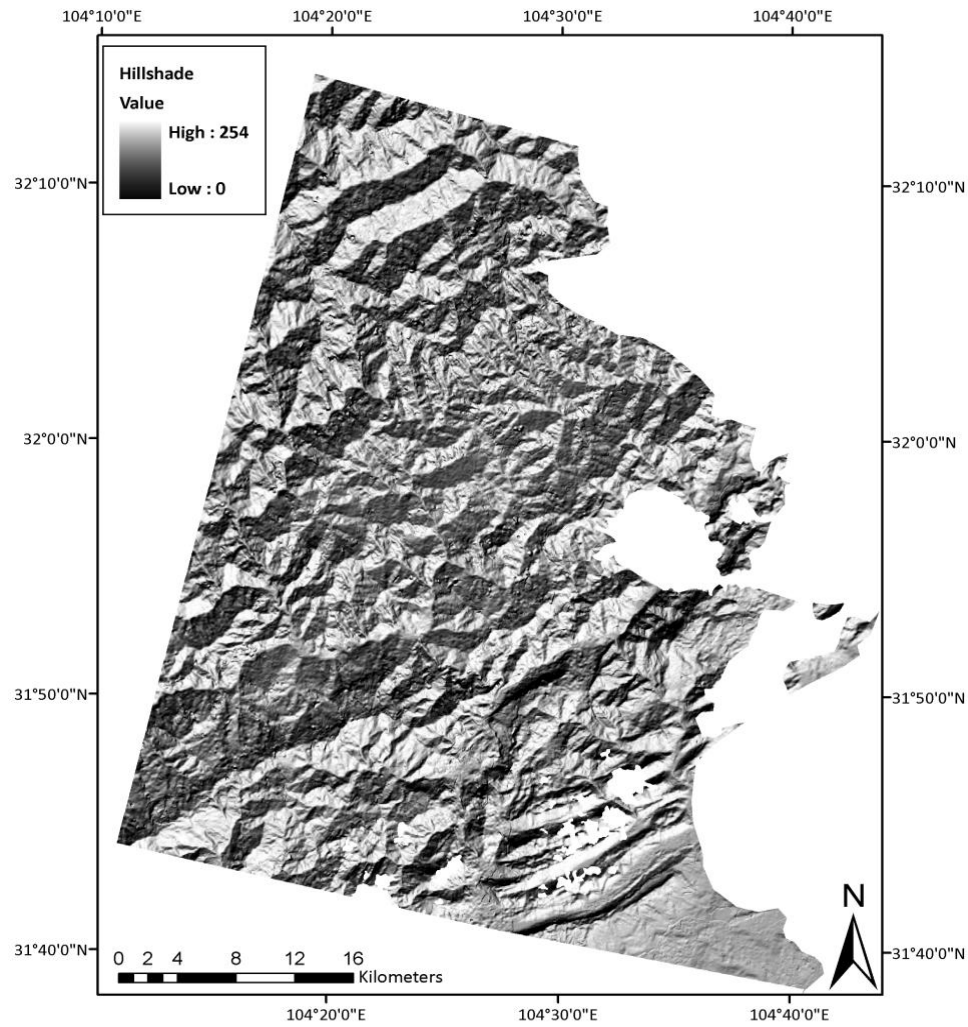


Figure 3.10: Hillshade map based on image S3 (produced using ArcMap Surface Tools). Areas in shadow are represented with a hillshade value of 0.

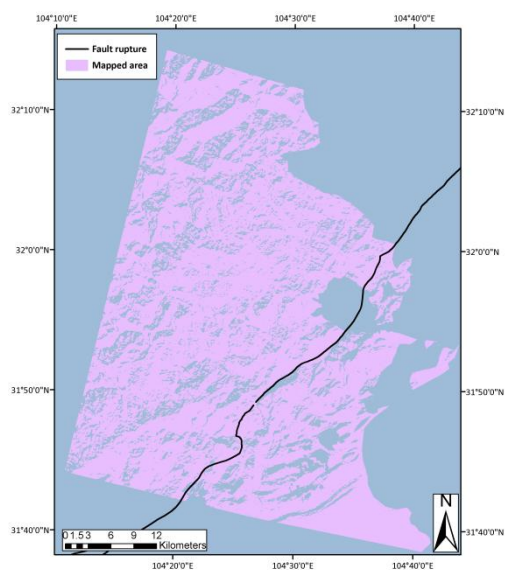


Figure 3.11a: Final mapped area

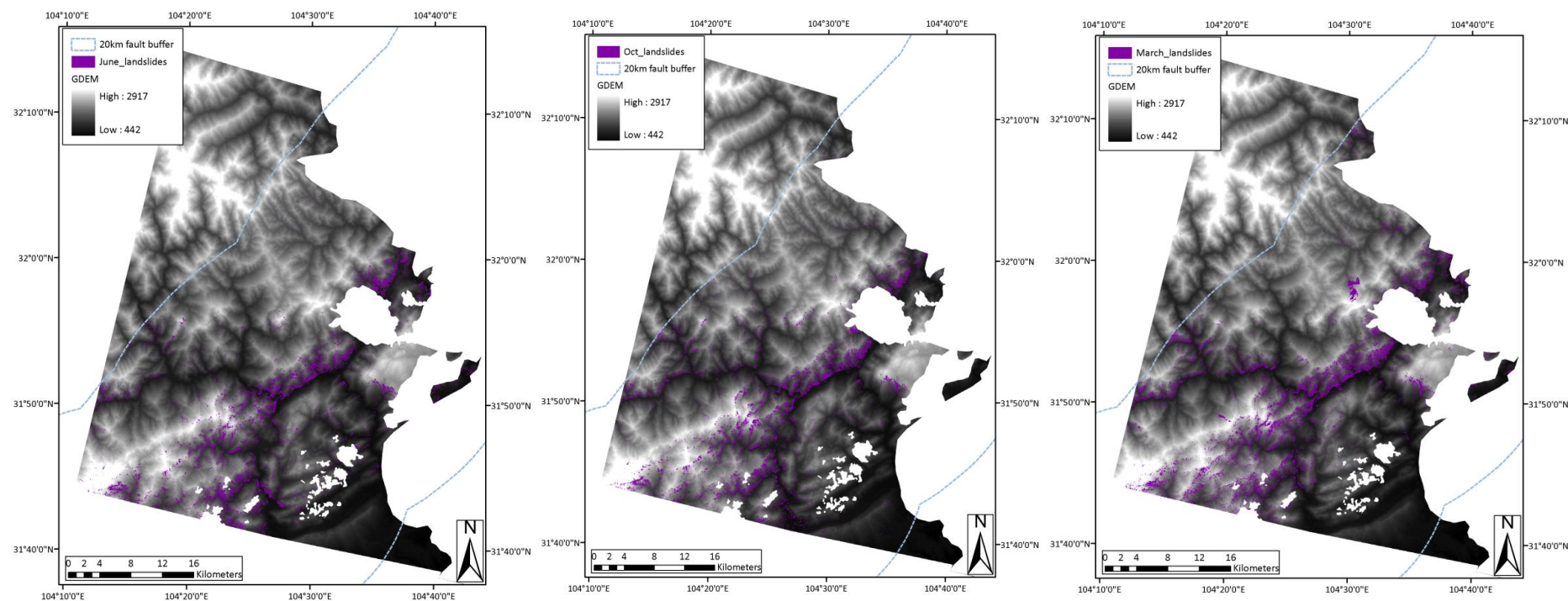


Figure 3.11b: Final landslide inventory maps following the 2008 Wenchuan earthquake based on images S1, S2 and S3 respectively.

3.1.7. Stage Five: Validation and evaluation of mapping

As discussed in the introduction to this chapter, cognitive recognition allows the human eye to distinguish landslide features from non-landslide features and thus manual delineation is commonly used as a method of mapping failures (Huang and Li, 2009; Wang *et al.*, 2009a). Therefore to validate the results of the landslide inventory maps produced from images S1, S2 and S3, manual mapping was compared with the results of the automated landslide classification over a square 16 km² test area (Figure 3.12a). Failures within this area were manually digitised as polygons and the results compared with the shapefiles created from the automated classification (see Figure 3.12b).

Table 3.2 shows the results of this comparison, which are comparable to results from Parker (2010) and Borghius *et al.* (2007) when using the same method. The main differences between the two techniques are in the total area mapped and the amount of individually mapped objects:

- In agreement with previous investigations, the automated classification under-sampled compared to manual delineation (by approximately 10 to 15 %) for images S1 and S3, shown by the larger error of omission than commission. This could be due to a number of reasons, including omission of landslide features that occurred below the threshold slope value (20°); omission of landslide features smaller than the 300 m² noise filter (Nichol and Wong, 2005); automated delineation of landslides, which draws exact lines around pixel edges and therefore may omit areas at the edges of the failures; and the identification of failures on a cell-by-cell basis, excluding any areas of vegetation, thus omitting these areas of landslide features.
- In contrast with images S1 and S3, the automated classification over-sampled for image S2 and delineated an area almost 8 % larger than manual mapping. Although the error of commission is larger than omission, the difference between the techniques is smaller than for the two multispectral images. This is most probably due to the different classification technique used for image S2.
- As a result of the aforementioned differences, the areal overlap of automated and manual techniques ranges from 49.5 to 66.7%, which is similar to results from Parker (2010) of 58.7 to 66.2%, and from Borghius *et al.* (2007) of 53 to 66%.
- Despite the automated classification predominantly under sampling, the number of individually mapped features generated is much greater than for the manual technique. This is true for all images and particularly for image S3 where 476 features were delineated by the automated classification compared to 81 by manual techniques. This is due to the breaking-up of failures by the automated classification

(explained above) in contrast to the manual technique, which amalgamated multiple failures into one large failure if the space between them was too small to allow accurate separation. Consequently the number of individual failures is not a reliable statistic, and therefore frequency analysis is not used in this study. Despite this, the data do provide a relatively accurate first-order assessment of the extent and distribution of affected areas.

It is important to note that neither technique was regarded as significantly more accurate than the other; rather the accuracy of both techniques is measured more by the level of agreement between them. Based on this it is reasonable to state that the automated classification is suited to the analysis used in this study, indicated by the agreement between the data, which is comparable to results from previous studies.

At a later stage it became possible to further validate the results and individually test the accuracy of the automated technique through the use of fieldwork. Sample sites were chosen so that a variety of failures were sampled on both sides of the fault, in as many different lithologies as possible and at different heights on the hillslope. ArcGIS was used to select many potential sites based on these criteria and the accessibility of these areas ultimately determined which were sampled. During fieldwork carried out in April 2010 over 50 landslides were mapped through the collection of geometric measurements and field inspection, providing data on the location and size of landslides that could be compared with the desk-based automated classification. Of those that were located in the area covered by imagery, GPS points from the fieldwork were overlaid onto the landslide inventory maps. A simple yes/no classification was used based on whether the automated mapping had identified the failure and further visual assessment of the results determined the extent of mapping. Results are shown in Table 3.3.

Due to the time lag between image acquisition and ground surveying it was expected that there would be some discrepancy between the field data and the classification data, increasing with the time difference. In addition approximately 15% of the failures surveyed were located in areas covered by cloud and therefore were not mapped from satellite imagery. This explains the decreasing percentage of failures that were recognised by the automated technique (see the first row of Table 3.3). The other statistics listed in Table 3.3 are based only on the mapped failures and therefore are more appropriate for describing how well the identified failures were mapped:

- *Partially mapped:* The increasing proportion of partially mapped failures with time is partly reflective of the evolution of failures between June 2008 and April 2010. In

approximately half of the cases for images S1 and S2 the classification had delineated the entire failure as was visible on the image, however the extension of failures since – via propagation upward and laterally, and through failure of lower slopes merging with failures above – caused them to appear only partially mapped.

- *Coalescence in mapping:* The clumping together of failures by the automated classification is most common in image S3 due to the lower spatial resolution of 10 m. This appears mainly to occur on lower slopes where many long, narrow landslides have failed in close proximity. However, as the data was not used for magnitude-frequency analysis, this did not affect the investigation of results.
- *Mapped as in-field:* For images S2 and S3 the percentage of failures delineated by the automated classification as they were seen in the field, fall within the range of results from the comparison of automated and manual techniques (Parker, 2010; Borghius *et al.*, 2007). This statistic for image S1 is lower (40%) however accounted for by the evolution of failures over a period of almost two years.

Overall this comparison with ground surveyed data supports the previous validation of results, further indicating that the automated classification is suited to the analysis of this study. Aside from the discrepancies in mapping due to the time lag between image collection and fieldwork, and also due to cloud cover obscuring some areas of imagery; the failures that were not classified by the automated technique were rockfall failures located in the footwall, suggesting that the classification techniques used do not recognise this type of failure as easily as landslides. Consequently the analysis of results has assumed to focus predominantly on landslide failures, excluding rockfall.

The following section presents the results and analysis of the landslide inventory maps with respect to the landslide distribution and the geophysical controls upon this. It also provides details of the methods used in analysis and the impact of the sampling resolution.

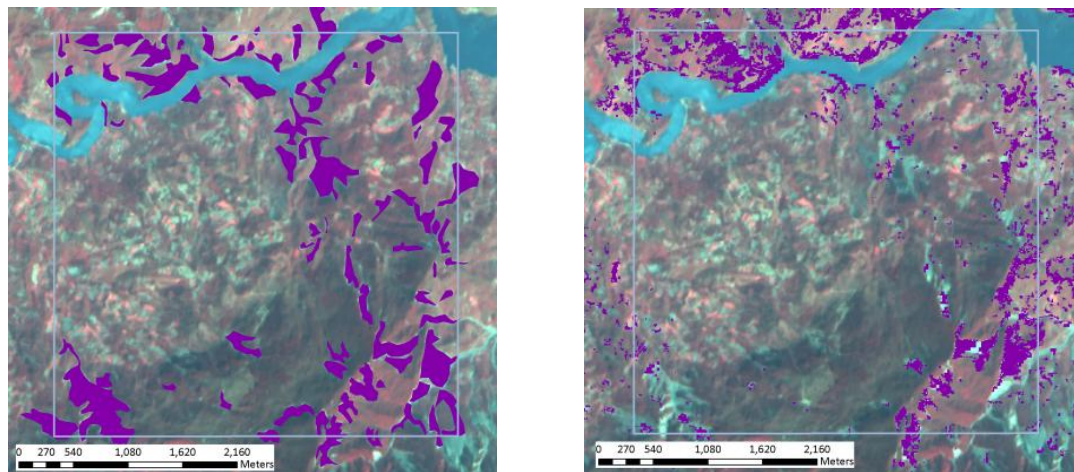
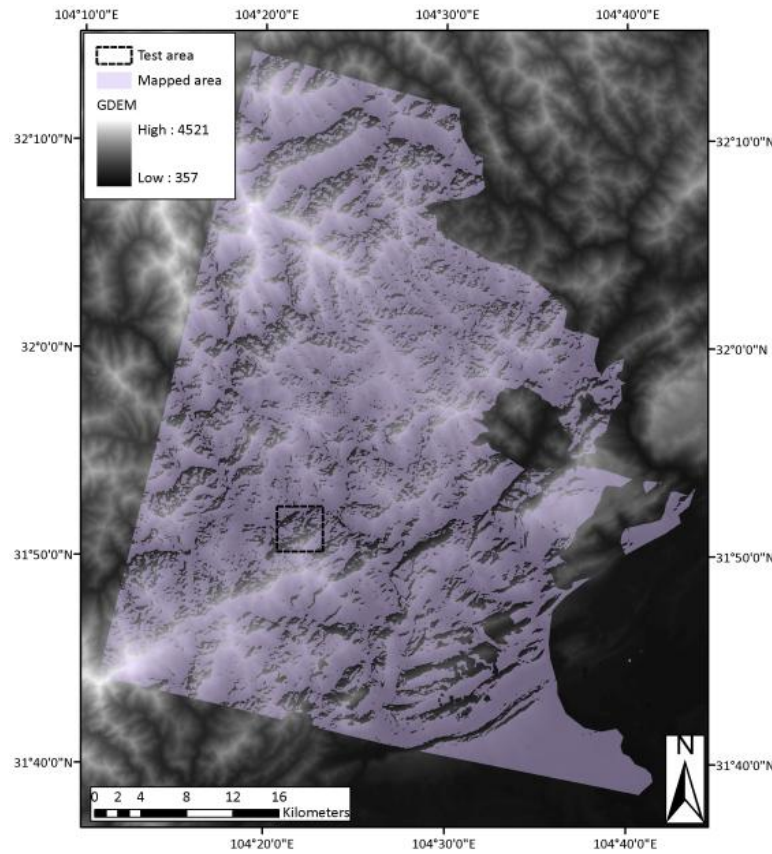


Figure 3.12: 16 km² test area used for comparison of mapping techniques – **a** shows the location of the test area; **b** displays the manual mapping (left) and automated mapping (right) of image S3 for the test area.

Table 3.2: Results of comparison between automated and manual mapping techniques

Image Mapping technique	June 2008 (S1)		October 2008 (S2)		March 2009 (S3)	
	Automated	Manual	Automated	Manual	Automated	Manual
Total mapped area (km ²)	1.19	1.41	1.06	0.99	1.86	2.11
Area difference (%)	15.62		-7.54		11.86	
Average density (%)	13.47	11.37	15.04	16.17	8.59	7.57
Density difference (%)	2.10		-1.13		1.02	
Individually mapped features	183	141	256	143	476	81
Error of commission (km ²)	0.32		0.48		0.88	
Error of omission (km ²)	0.54		0.41		1.13	
Areal overlap (km ²)	0.87		0.58		0.98	
Areal overlap (%)	66.69		56.81		49.45	

Table 3.3: Results of validation of automated mapping technique with field data

Image Image type	June 2008 (S1) SPOT 5 XS (5m)	October 2008 (S2) SPOT 5 Panc. (5m)	March 2009 (S3) SPOT 5 XS (10m)
% of ground surveyed landslides mapped (<i>a</i>)	71.4%	57.1%	57.1%
% of <i>a</i> partially mapped	53.3%	26.7%	25%
% of <i>a</i> clumped in mapping	6.7%	0	16.7%
% of <i>a</i> mapped as seen in field	40%	66.7%	58.3%

3.2. Analysis of landslide inventory maps

3.2.1. Preliminary results

Landslide area statistics provide an impression of the spatial extent and distribution patterns of landsliding. As a result they highlight areas of high and low density of landsliding, thus indicating the regions that likely supply the most material to the fluvial system.

Using *ArcMap Spatial Analyst*, summary statistics were extracted from the inventory maps based on the polygon shapefiles that represent failures (Table 3.4). The total failure area increased between each image: a small increase of 1.03% between June and October 2008 and a much larger increase of 40.65% between October 2008 and March 2009. This is reflected in the increase of number of individual failures, however the increase is not proportional to the total area: 17.50% increase from June to October and 62.15 % increase from October to March.

To statistically analyse the landslide distribution, the polygon shapefiles representing failures had to be re-sampled as numerical data, i.e. to landslide density, defined by a grid of variable spacing. In order to extract these data from the polygon features, sample grids were created using *ArcMap XTools Pro*, which limited the grid cell size to a minimum of 500 m². As a result three grids were created with cell sizes 500 m², 1,000 m² and 2,000 m² (see Figure 3.13): the grid size was not set any higher than this as a larger grid would not provide adequate coverage of the mapped area (due to its non-rectangular shape). Grid cells were decided as the mapping unit as they are most suited to raster-based GIS analysis and preferred for statistical modelling (Guzzetti *et al.*, 1999). The sample grids allowed the total landslide area and number of failures to be calculated for each grid cell. However as mentioned in section 3.1.7, the data is not suitable for frequency analysis, thus negating the need for statistics of the number of failures. Rather, to focus on the extent and distribution of failures, landslide density was calculated and used as a primary unit of analysis along with landslide area. This is an established approach to analysing landslide inventories (Guzzetti *et al.*, 1999). For the purposes of this research, whenever landslide density is referred to, it is based on the following equation (3.1):

$$\text{Landslide density (\%)} = (\text{landslide affected area} / \text{total sample area}) * 100 \quad (3.1)$$

In order to visualise this information, landslide density maps were created using the *Zonal Statistics* function in the *ArcMap Spatial Analyst toolbox*. The highest resolution grid available (500 m²) was used for this and the resulting maps are shown in Figure 3.14.

In all three maps the areas with a higher landslide density concentrate around the earthquake surface rupture; moving away from the fault, the landslide density decreases and areas with no failures become more widespread. Between the images, i.e. over time, there is an overall increase in landslide density which is spatially non-uniform. Areas of very high density landsliding, i.e. > 70%, increase in the north of the study area, whilst an increase in areas of mid-density landsliding, i.e. 20 – 70 %, is seen in the south and west of the study area. In addition, whilst the overall spatial distribution of all landslide areas (density > 0 %) remains similar between June '08, October '08 and March '09, there are some noticeable changes, including areas of new landsliding and areas where landsliding has seemingly decreased, i.e. re-vegetation has begun.

These maps provided a good overview of the distribution, extent and temporal changes in landslide density. All of these patterns are explored in more detail at a higher sample resolution and analysed with respect to the geophysical controls on landsliding in section 3.3.3.

Table 3.4: Summary statistics from landslide inventory maps

	June	October	March
Study area (km²)	1503.47	1503.47	1503.47
Total area of failures (km²)	55.39	55.96	78.71
% of study area occupied by failures	3.68	3.72	5.24
Individual failures	9765	11474	18605

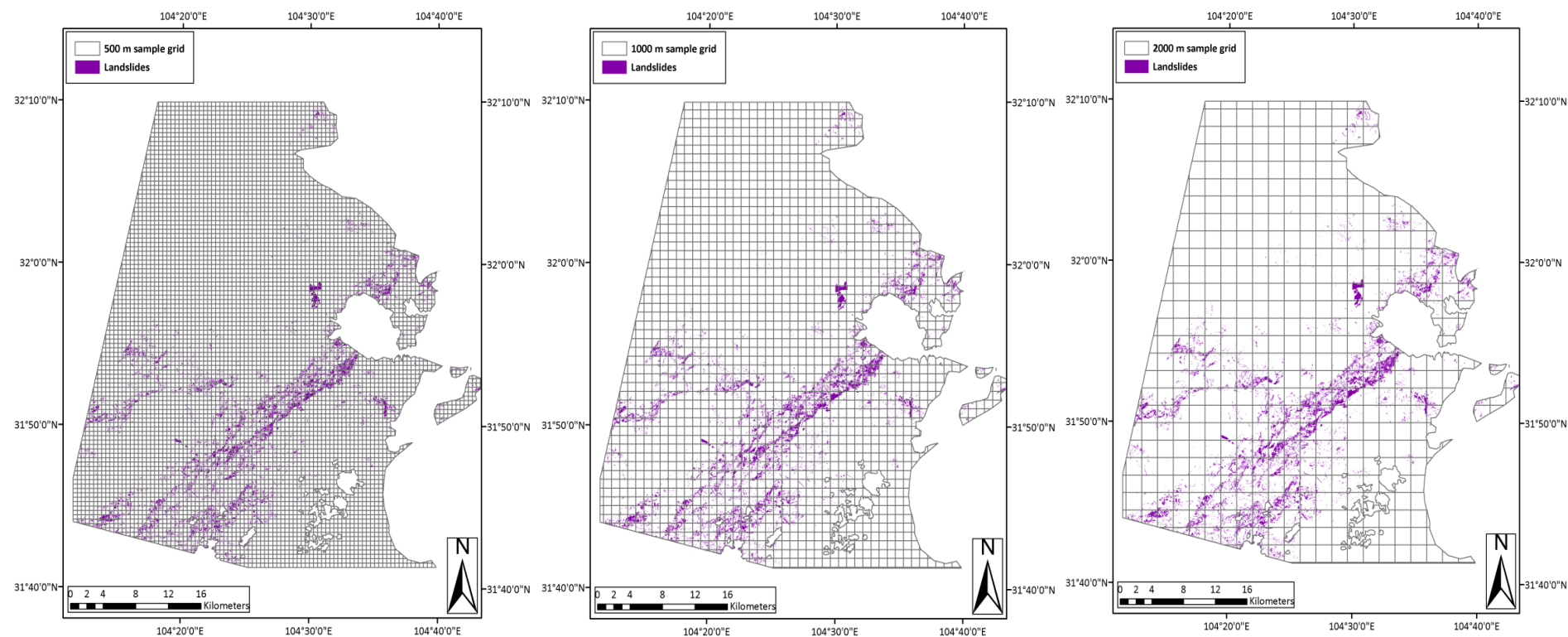


Figure 3.13: Sample grids – left to right: 500 m²; 1000 m²; 2000 m²

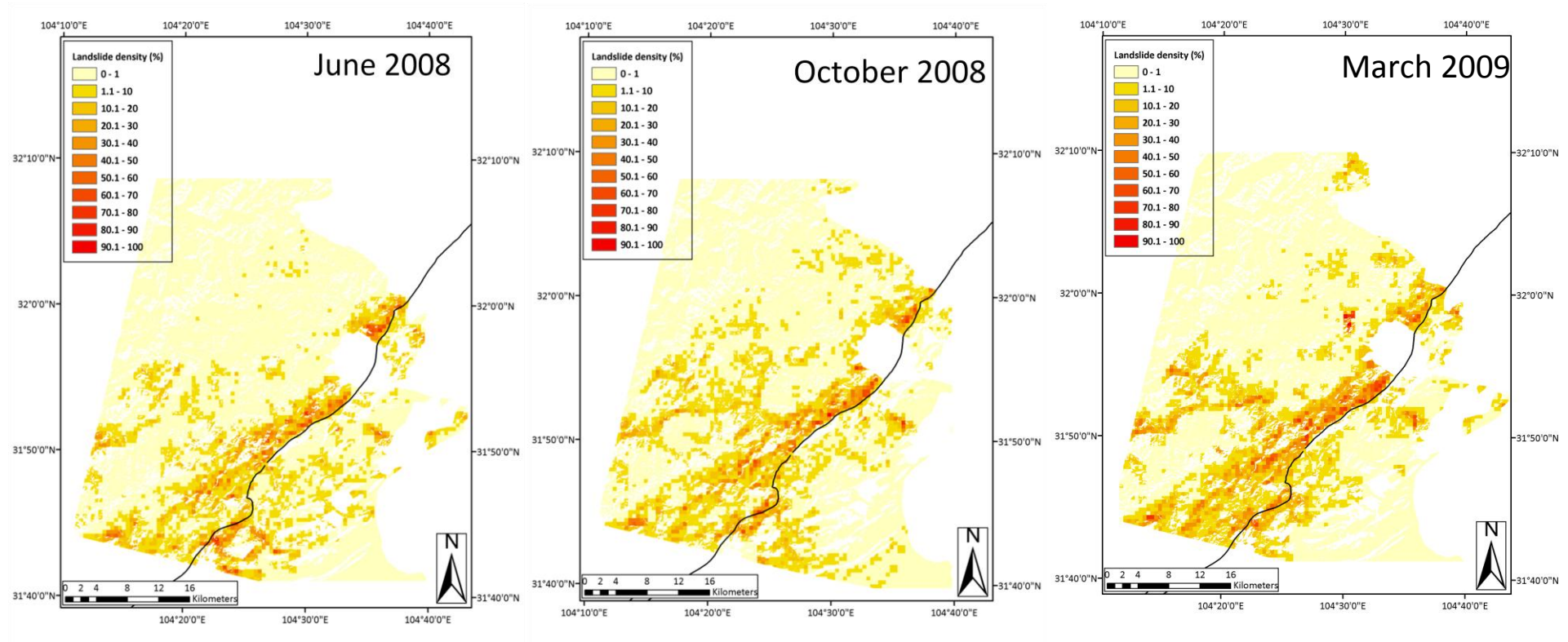


Figure 3.14: Maps of landslide density based on data extracted using the 500 m² sample grid. The main fault rupture is shown in black.

Case studies

To illustrate the key patterns of temporal change that can be seen in the extent and distribution of landslides, four case studies have been selected:

1: New post-seismic failures

As shown by the increase in spatial area and more specifically, the increase in number of failures from June 2008 to March 2009 (see Table 3.4), many new landslides occurred post-seismically. Figure 3.15 shows an area of hillslope to the north of Beichuan in the hanging wall of the Beichuan fault; landslides can be seen in the October imagery in a location that appears not to have failed in the June image. These post-seismic landslides were most likely triggered by the heavy monsoonal rains that began in late September 2008, as suggested by their occurrence on lower parts of the hillslope (Densmore and Hovius, 2000).

2: Propagation of co-seismic failures

In addition to post-seismic failures, some co-seismic failures enlarged in the period following the earthquake through propagation up and across the slope. This helps to explain the disproportionate increase in total area of failures compared with the number of individual failures. Figure 3.16 shows an example of this at Huangjiaba – a small settlement located in the hanging wall of the Beichuan fault within a few hundred meters of the fault. The landslide extended across and down the slope and by March 2009 it had merged with another landslide on the lower part of the slope. In a similar way to the evolution of new failures in case 1, the extension of co-seismic failures were also most likely triggered by the heavy monsoonal rains; the failure of slope areas in close proximity to co-seismic landslides also supports the theory that those slopes weakened during an earthquake are more likely to fail post-seismically, i.e. they are pre-conditioned to fail (Chang *et al.*, 2007).

3. Re-vegetation

Although there was an overall increase in landsliding between June 2008 and March 2009, visual comparison of the landslide density maps (Figure 3.14) shows that in some areas landslide density decreased over that time period. A primary reason for this is the re-vegetation of co-seismic landslides, which did not fail again post-seismically, i.e. during the monsoon rains. The presence of vegetation changes the spectral reflectance of the failure so that it is no longer recognised as a landslide by the classification (see section 3.1). This is more commonly found on the higher slopes where post-seismic failures were less common: an example is shown in Figure 3.17. Located in a small valley opposite Huangjiaba in the footwall

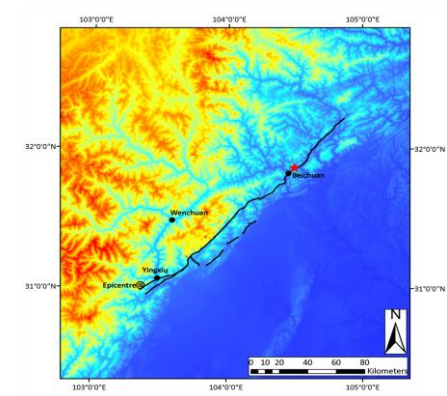
of the fault, this cluster of landslides can be seen very clearly in the June image, however much of the failure appears to have disappeared in the March image thus decreasing the landslide density.

4. Removal of landslide material

Another reason for the decrease in landslide density seen in some areas is the removal of landslide material by human interference and river incision at the toes. In many towns and villages the vast amount of re-building required people to source materials from the landslide deposits that provide an abundant source of aggregates. Therefore when looking at the imagery post-removal the overall landslide area appears to have reduced in size thus reducing the calculated landslide density. Figure 3.18 displays an example of where this has happened at Fenghuang, a small settlement near the river in the hanging wall of the Beichuan fault. As can be seen from the June image the landslide deposit spread out over the area surrounding the river, however in the March image this area has been cleared and only small amounts of deposits remain.



Figure 3.15: Post-seismic failures in the hanging wall north of Beichuan



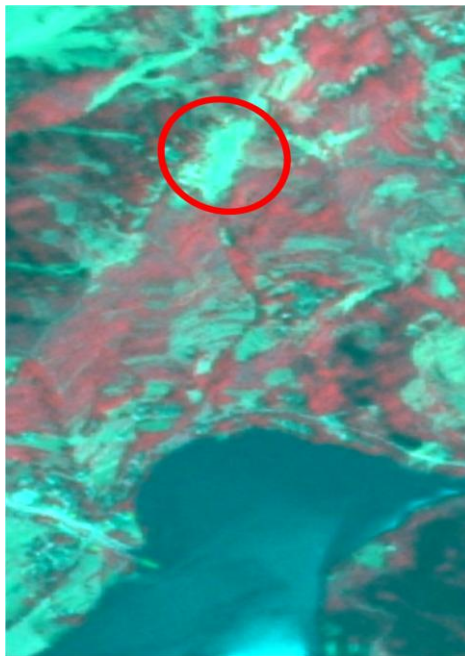
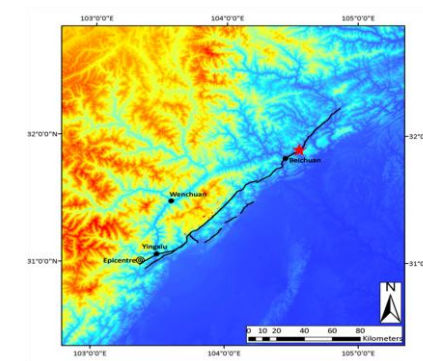


Figure 3.16: Extension of a co-seismic failure in the hanging wall at Huangjiaba – images (left to right): S1 (June 2008); S2 (October 2008); S3 (March 2009)

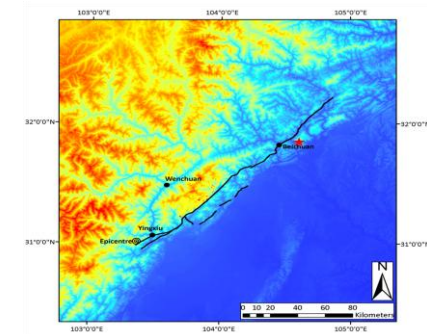


Figure 3.17: Re-vegetation of landslides on higher slopes in the footwall opposite Huanjiaba, indicated by the ‘disappearing’ of failures between images S1 (left) and S3 (right)

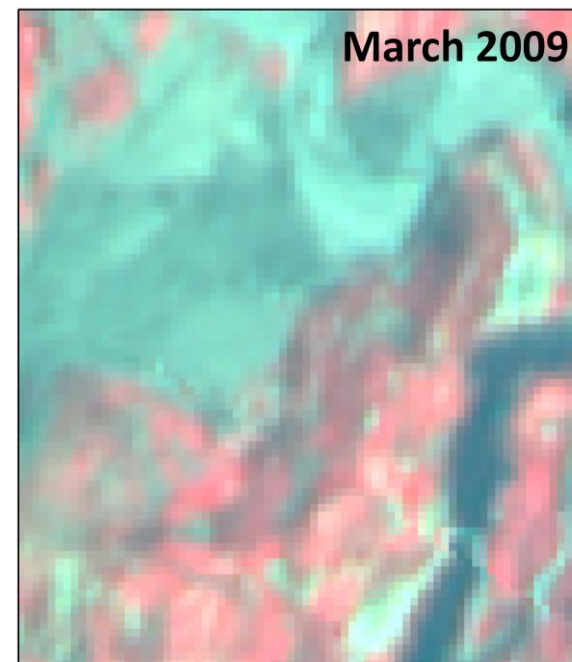
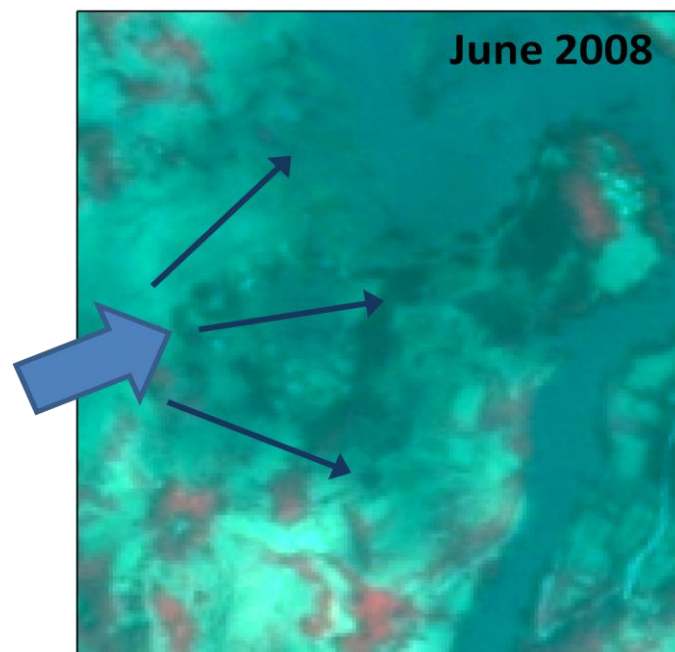
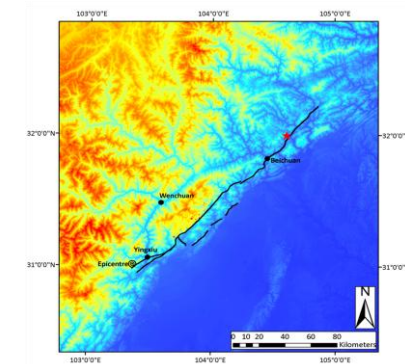


Figure 3.18: Removal of landslide deposit at Fenghuang as seen in the satellite imagery. Arrows on image S1 (left) indicate the direction of flow of material.

3.2.2. Analysing the sample grids

Kernel density estimation

Kernel density estimation (executed in *Stata 11*) was used to further investigate the landslide distribution and to provide an assessment of the impact of the varying grid sizes upon the data. The resulting plots for the March 2009 landslides can be seen in Figure 3.19a.

From these standard plots on a non-logarithmic scale it is hard to see the complete distribution of landslide areas, as this only represents a small portion of the dataset; the higher frequency of grid cells with a landslide density around zero cause all the remaining data (i.e. cells with a density > 0) to be compressed. However this does reinforce what is seen in the landslide density maps – that the areas of interest, i.e. areas containing landslides, are only a small portion of the entire study area.

In order to visually analyse the distribution of landslides in the study area, logarithmic plots (base 10) were created of the compressed data, i.e. that to the right of the red dashed line in Figure 3.19a. The logarithmic plots can be seen in Figure 3.19 (b-d) and whilst there are differences in the curves according to the grid resolution used in sampling, similar key features can be seen in each sample:

- The majority of grid cells in June and October 2008 have a landslide density between 1% - 10%, as indicated by the peak of the curve. By March 2009 the curve has shifted to the right and the majority of grid cells have a landslide density of 3% - 16%. This indicates that the majority of areas have a moderate landslide density, and that overall density in most areas has increased over time.
- Beyond a landslide density of 20% the curve drops off very quickly, showing that the majority of areas have a moderate landslide density and few areas have a high landslide density. Despite the overall increase in landslide density seen in the March 2009 plot, there doesn't appear to be an increase in areas of very high landslide density ($> 70\%$).

As mentioned, the different grid resolutions used alter the resulting distribution curve. Plots based on the 1,000 m and 2,000 m grids display smoother curves and lower landslide densities compared to the plot based on the 500 m grid. This is most probably because a sample area of 1,000 m or 2,000 m will average over an entire hillslope range (average hillslope length in Sichuan is approximately 2,000 m) and therefore the range of densities that occur across the hillslope will be smoothed as pixels are not always centred on the slope midpoint.

Whilst there are differences in the plots, all resolutions provide a valid analysis of the dataset, each at a different scale of interest. Such a range of data at different scales is needed in order to fully understand the development and impact of landslides (Metternicht *et al* 2005) and the following paragraphs describe the application of sampling at another scale.

Higher resolution sample grid

The density grids and kernel density plots provide a useful overall impression of the distribution of landslide failures. However a higher sampling resolution is required for more detailed analysis and particularly for exploring the relationship with geophysical controls on landslides. The topographic derivatives used to represent geophysical controls were obtained from the 30 m resolution GDEM and therefore this is the highest spatial resolution available for analysis. A sample grid was created based on the GDEM and was used to extract data from the inventory maps in a similar way to the lower resolution fishnet grids.

The higher resolution provided greater detail, reflected the scale of the various geophysical controls, and is at least one order of magnitude smaller than the average hillslope length, thus able to distinguish spatial variations in landsliding at this scale.

The analysis was focused on the following variables:

- Distance from the fault
- Gradient
- Relative relief
- Local elevation
- Geology
- Aspect

These were chosen because a landslide probability model for Sichuan (Parker, 2010) ranked them as the six most important geophysical variables in controlling landslide occurrence in this region. The following section deals with these variables in turn, analysing each with respect to the changes in landslide density distribution over time observed herein.

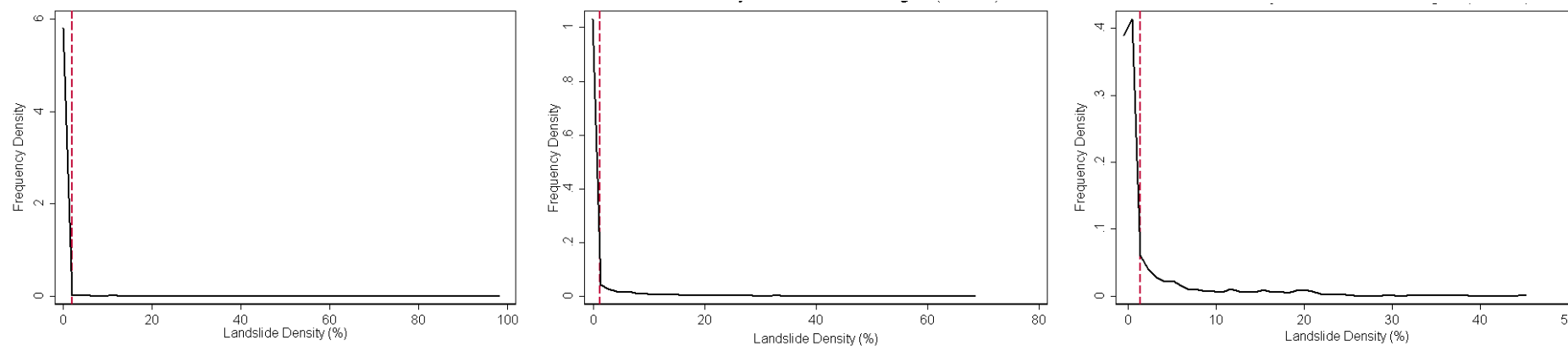


Figure 3.19a: Initial kernel density plots for the March 2009 landslide inventory, based on a 500 m; 1,000 m; and 2,000 m grid respectively (left to right)

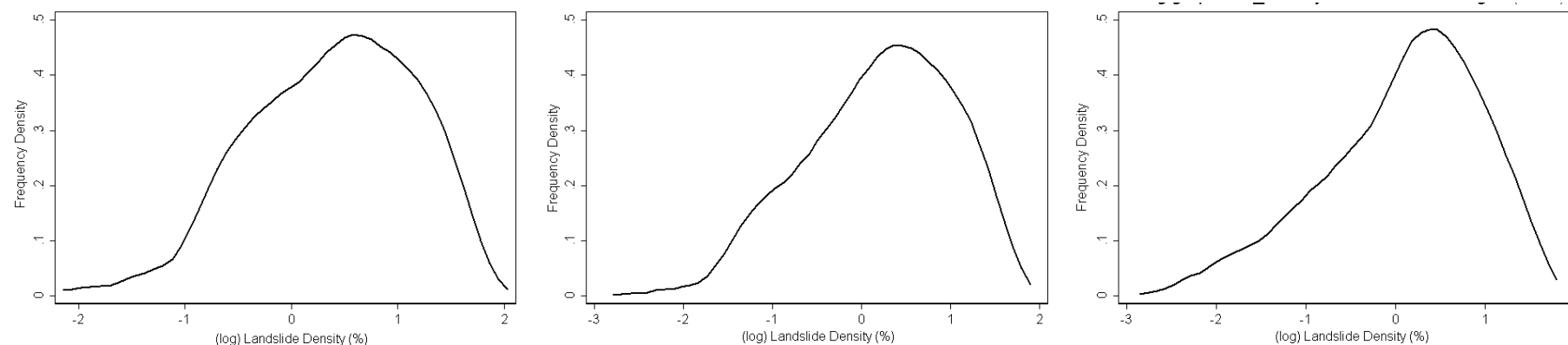


Figure 3.19b: Log – frequency plots for the *June 2008* landslide inventory data where Landslide Density > x. Plots based on a 500 m; 1,000 m; and 2,000 m grid (left to right), where x = 1.5 %; 0.9 %; 1.1 % respectively.

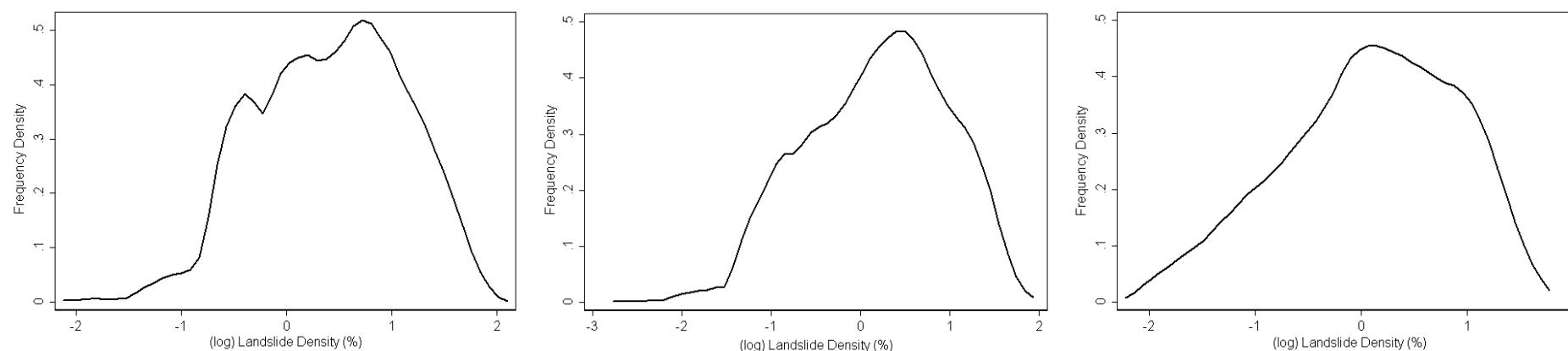


Figure 3.19c: Log – frequency plots for the *October 2008* landslide inventory data where Landslide Density > x. Plots based on a 500 m; 1,000 m; and 2,000 m grid (left to right), where x = 1.8 %; 0.98 %; 1.1 % respectively.

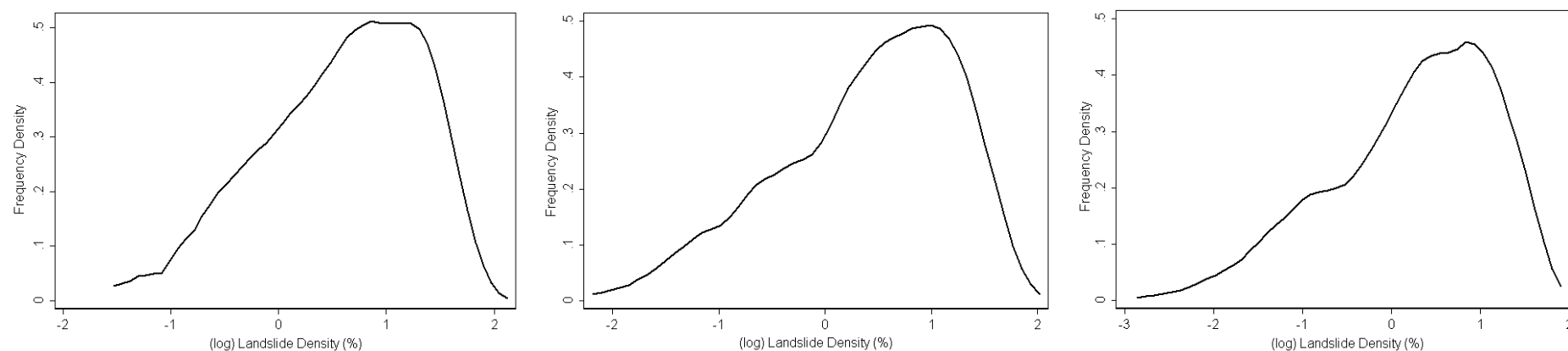


Figure 3.19d: Log – frequency plots for the *March 2009* landslide inventory data where Landslide Density > x. Plots based on a 500 m; 1,000 m; and 2,000 m grid (left to right), where x = 1.95 %; 1.2 %; 1.4 % respectively.

3.2.3. Geophysical variables

When evaluating landslide inventories, a crucial stage is the interpretation of results in the context of the geomorphological setting (Guzzetti *et al.*, 1999). The geophysical variables listed above can be used to define this setting. In addition they all have a conceptual link to the occurrence of landslides and are regarded as important controls upon this, not only for the Sichuan region (Parker, 2010) but also in many other cases, i.e. controls on landsliding following the 1999 Chi-Chi earthquake (Lin *et al.*, 2008). The processes which link each variable to the occurrence of landslides are outlined in Table 3.5: in some cases the process varies co-seismically and post-seismically. The first control on landslide occurrence, Distance from co-seismic fault rupture, is a seismic control, related to the pattern and recognition of co-seismic shaking (Meunier and Hovius, 2006). The remaining five controls are non-seismic and associated with the physical causes of hillslope instability, thus providing the potential for failure when seismic activity occurs (Owen *et al.*, 2008).

Each control was assessed in turn in order to address the following questions:

- i. How do the results based on the June 2008 landslides from this dataset compare with previous regional studies of Wenchuan earthquake-triggered events, which covered the entire earthquake affected area?
- ii. How do the relationships between each variable and landslide occurrence (measured as landslide density) change over time, between June 2008, October 2008 and March 2009?

Table 3.5: Geophysical variables ranked as the most important for evaluating landslide susceptibility in Sichuan (from Parker, 2010) and the processes that they represent co-seismically and post-seismically.

Geophysical variable	Process (co-seismic)	Process (post-seismic)
Distance from co-seismic fault rupture	Attenuation of PGA and density-decay theory (Meunier and Hovius, 2006)	Hillslopes pre-conditioned to fail through co-seismic shaking (Chang <i>et al.</i> , 2007)
Gradient	Potential energy available for erosion based on balance of forces within a hillslope (local scale)	Potential energy available for erosion based on balance of forces within a hillslope (local scale)
Relative relief	Balance of forces (gradient) at the hillslope scale	Balance of forces (gradient) at the hillslope scale
Local elevation	Topographic amplification of seismic waves (Meunier <i>et al.</i> , 2008)	Concentration of storm-triggered landslides at hillslope toes (Densmore and Hovius, 2000)
Geology	Impact of co-seismic shaking on material properties of the rock & soil (Wen <i>et al.</i> , 2004)	Impact of extreme rainfall on material properties of the rock & soil
Aspect	Direction of seismic waves; sub-aerial processes – influencing soil strength and energy for erosion (Chang <i>et al.</i> , 2007)	Hillslopes pre-conditioned to fail; impact of orographic rainfall

Distance from the co-seismic fault rupture

Many previous studies regarding earthquake-triggered landslides have noted the dominant effect of the fault rupture on landslide distribution, which can be summarised as an inverse relationship between landslide density and distance from the fault (Meunier and Hovius, 2006). Evaluating distance from the fault rupture with respect to landslide occurrence is regarded as a more refined relationship than distance from the epicentre because the seismic energy is released throughout the fault rupture zone rather than just from a single point (Keefer, 1984).

In order to examine this relationship, the 30 m sample grid was used to provide the landslide density and the distance from the fault for each grid cell. Areas in the hanging wall were assigned negative distance values to allow an across strike profile to be produced. The data were evaluated in 1 km bins across strike and the resulting profiles can be seen in Figure 3.20a. Density decay plots for values in both the hanging wall and footwall were also produced for each time interval to allow easier visual comparison of the data (Figure 3.20b).

In accordance with previous studies, landslide density decays with distance from the fault in both directions. There is a hanging wall effect in the distribution (Huang and Li, 2009a),

which becomes more exaggerated over time: this can be seen in both the across-strike profile and exponential plots. Previous studies, based on data from the entire earthquake affected region, display a clearer hanging wall effect (i.e. Parker, 2010; Huang and Li, 2009). This could be because this dataset is based on an area of very high peak ground acceleration around Beichuan, allowing for an increase in landsliding in the footwall compared with the overall trend.

Over time the landslide density increases in the hanging wall and decreases in the footwall thus accentuating the hanging wall effect, which can be seen most clearly in the density decay plots (Figure 3.20b). This indicates that post-seismic, rainfall induced landslides have preferentially occurred in the hanging wall, suggesting that a larger number of co-seismically weakened slopes that didn't initially fail are present in the hanging wall.

Slope

Steeper slopes are inherently more unstable due to the balance of forces on a hillslope. The gravitational potential energy (GPE) is larger and thus when a trigger such as seismic shaking or heavy rainfall occurs, the steeper slopes are more likely to fail.

To analyse the relationship between landslide density and slope, the gradient was calculated from the 30 m GDEM and the data were resampled in 1° gradient bins and the 30 m sample grid was used to provide the relevant slope data for each grid cell. Landslide density curves (Figure 3.21) were produced based on the mean values of landslide density (mean – P^L). Normalised area plots were also produced (see Figure 3.22a) to show the distribution of gradients across the whole study area and across landslide areas (i.e. areas with a landslide density >0).

Results from Parker (2010), which were based on data from SPOT imagery for the whole earthquake-affected area, indicated that areas of higher than average landslide density are found on steeper hillslopes and areas of lower than average landslide density are found on shallower hillslopes. Figure 3.22a also displays this trend for all three distributions, however the distinction between the distribution of gradients for all areas and landslide areas is even greater than results from Parker (2010). In order to visualise this more clearly, difference plots of the two curves were produced (Figure 3.22b), which clearly indicate that landslides are preferentially occurring on slopes with a gradient between 25° and 55°. This has been recognised by other landslide studies following the 2008 Wenchuan earthquake (Chen *et al.*, 2009) and seemingly fits a more widely recognised trend of seismically related landsliding occurring on moderately steep terrain (Zhou *et al.*, 2002). However it is important to note that

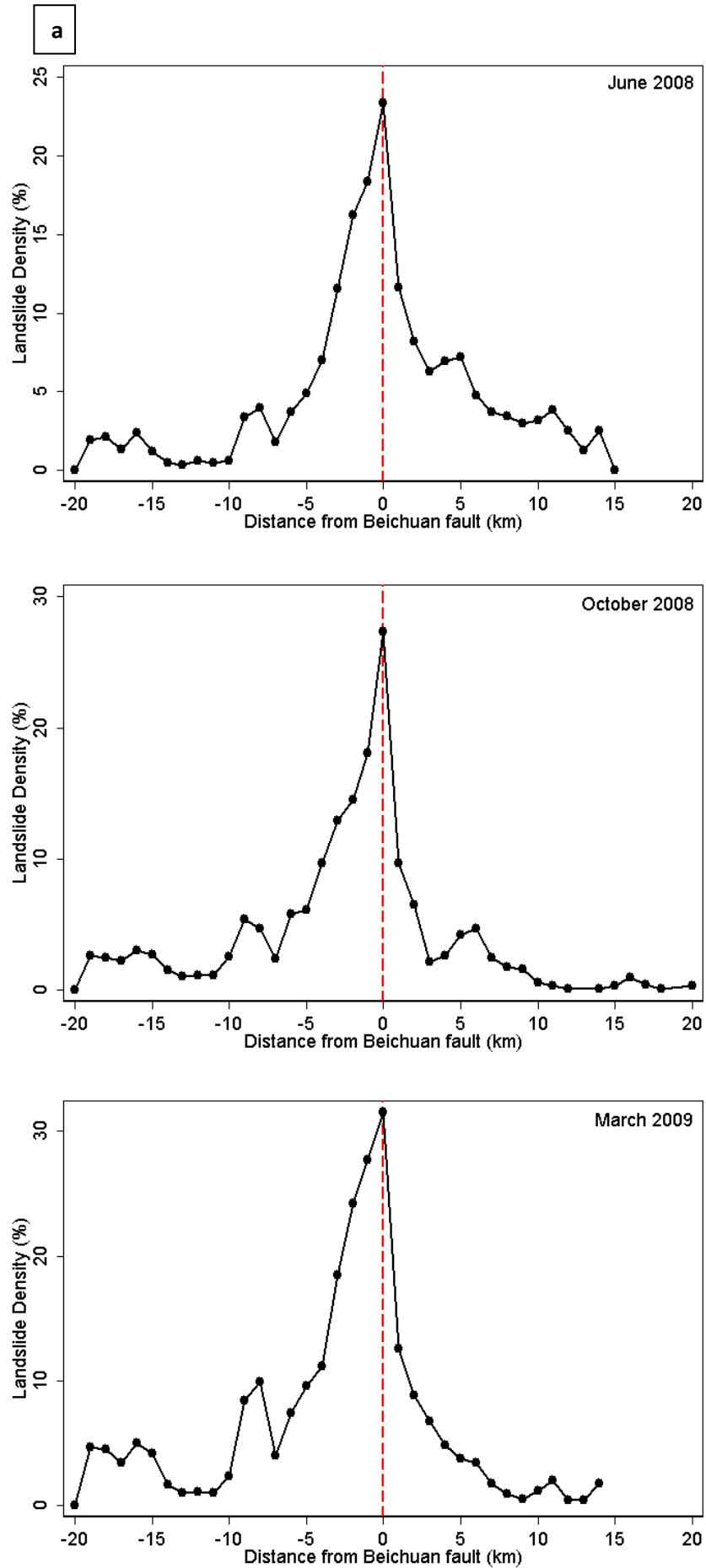
landslide density is above average for all gradients above 25°, i.e. the area of landsliding is disproportionately greater than the area of topography for those gradient values; the landslide density tends to 0 at 55° mostly because there is almost no topography with gradients above this value.

Landslide density plots (Figure 3.21) also agree with results from Parker (2010), showing an overall positive relationship between landslide density and gradient. However an inflexion occurs at higher slope values due to the small size of the sample area at these values (shown in Figure 3.21): the inflexion for this dataset occurs between 55° and 62° and between 62° and 67° in the data from Parker (2010). This indicates that due to decreasing sample size, variability in landslide density also increases with gradient.

Temporal changes in the data can be seen most clearly through comparison of the landslide density curves (Figure 3.21). Landslide density generally increases at all gradients over time (note the difference in scale for the March 2009 curve): between June and October the increase is most pronounced in the mid-high range of gradients, i.e. 35° - 55°; this is in contrast to the increase between October and March, which is most pronounced in the low-mid range of gradients, i.e. 20° - 40°. Despite these differences, the overall shape of the graph remains for all three distributions, including the inflexion between 55° and 62°.

To visualise the temporal changes between June 2008 and March 2009 a difference plot was created based on the June and March distribution curves. Figure 3.23 shows that post-seismic landslides are occurring on shallower slopes compared to the initial co-seismic failures, as indicated by the spike in the graph between 20° and 25°.

Overall these data supports the idea that post-seismic landslides occur on areas and gradients of hillslope that also experienced co-seismic landsliding (Chang *et al.*, 2007), shown by the general increase in landslide density between 25° and 55° over time.



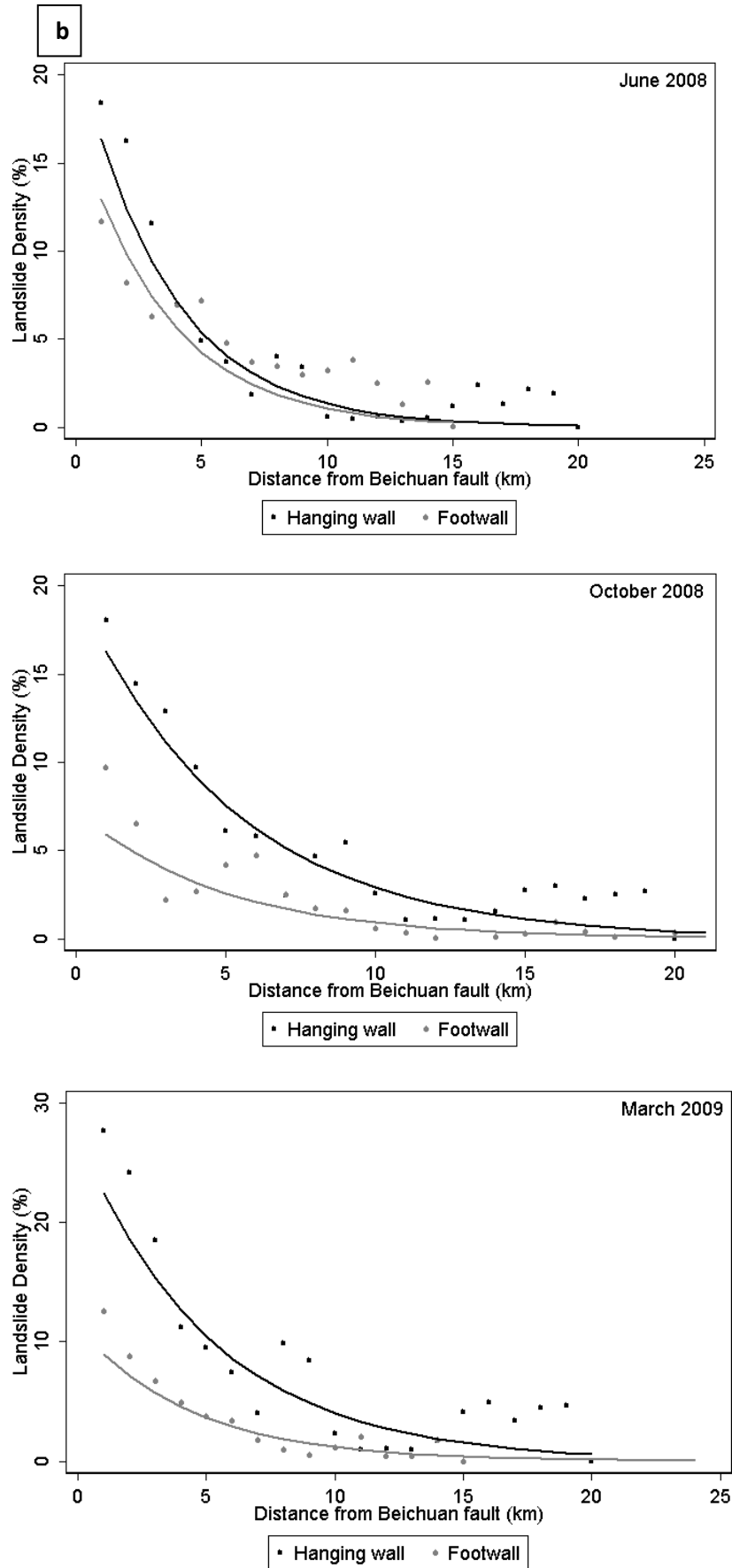


Figure 3.20: The relationship between landslide density and distance from the fault – **a**: Across-strike profiles of landslide density; **b**: Plots of landslide density decay at 1 km distance intervals from the fault for the hanging wall and footwall.

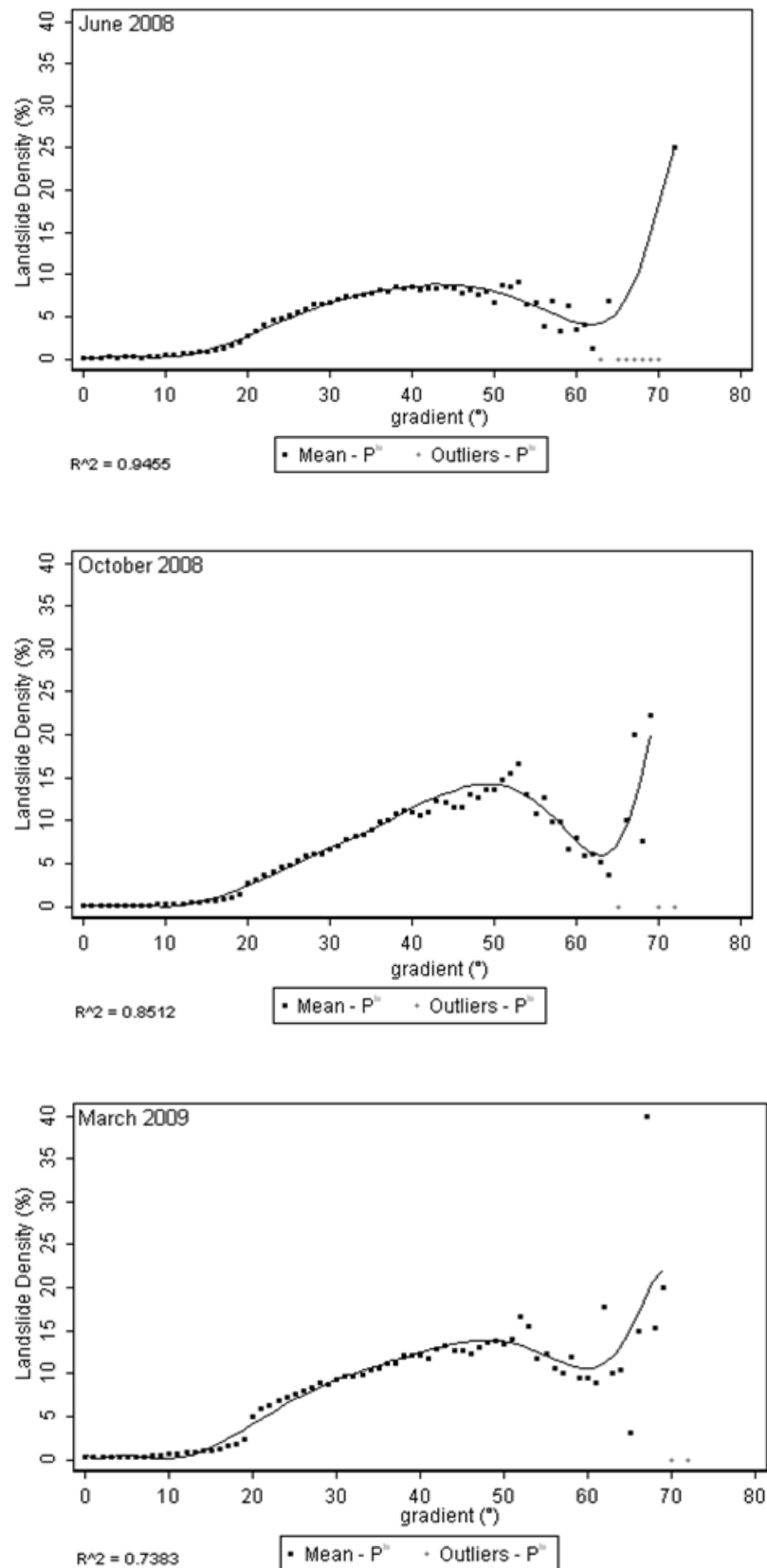
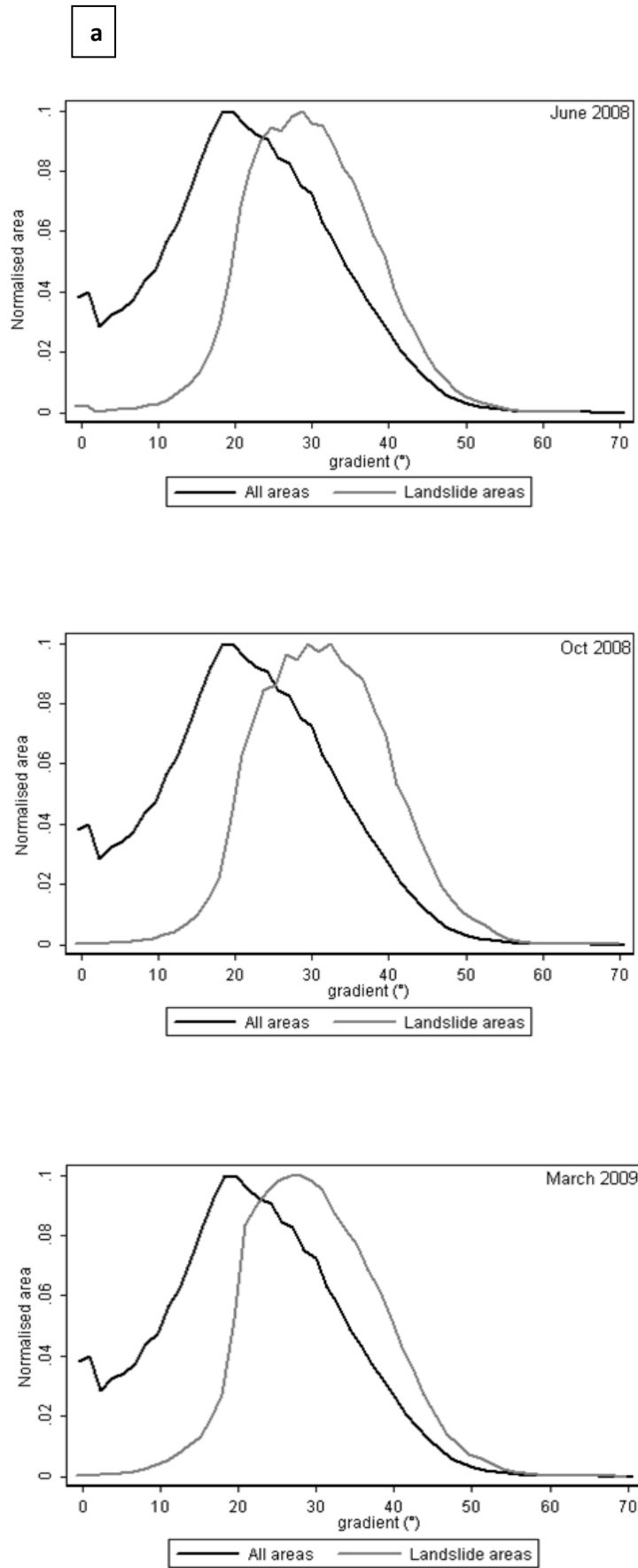


Figure 3.21: Landslide density distribution plots (with polynomial trendlines: order 5). The outliers (light grey) were not included when evaluating the trendline.



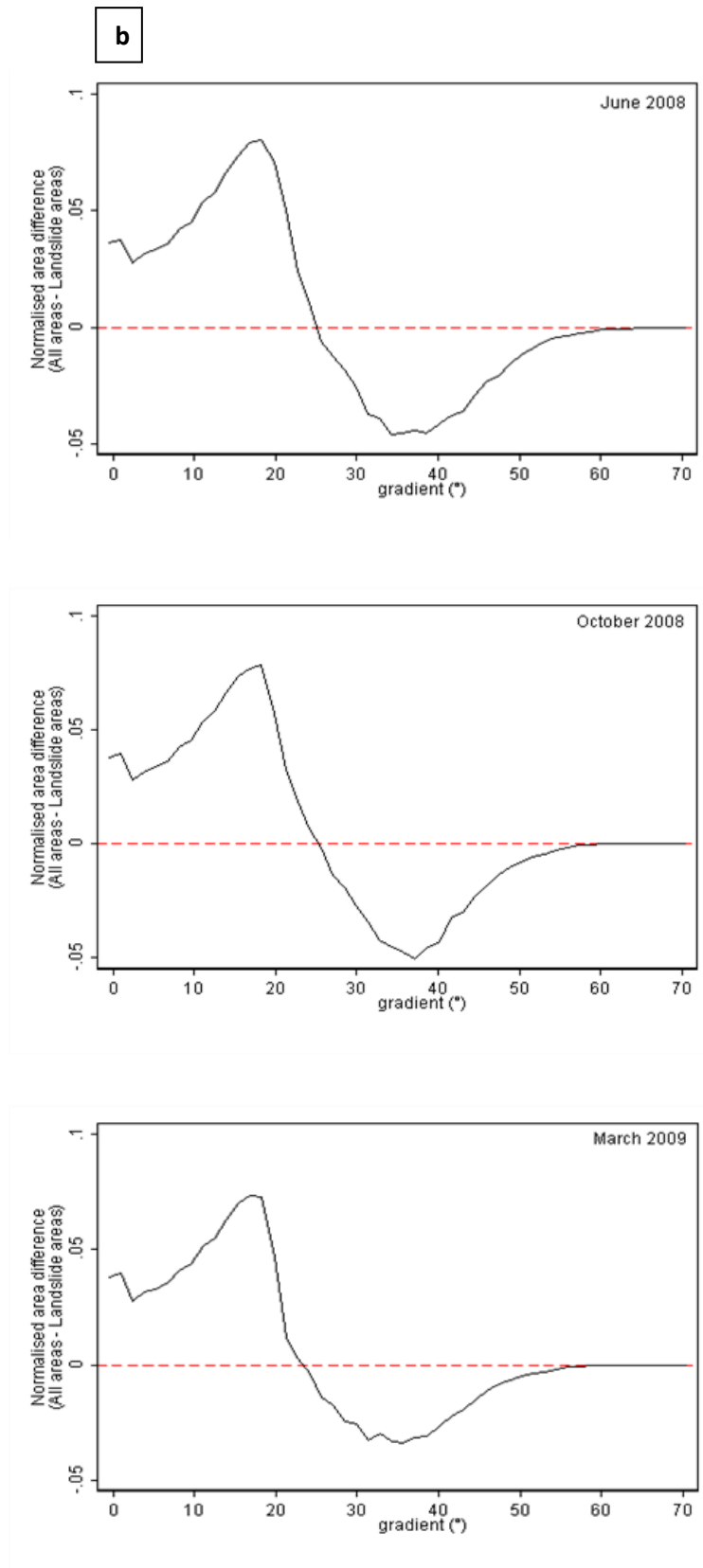


Figure 3.22: Normalised area plots (a) and associated difference plots (b) for the distribution of all areas and landslide areas across gradients in June 2008, October 2008 and March 2009. The red dashed line in the difference plots indicates the point at which all areas and landslide areas are distributed equally.

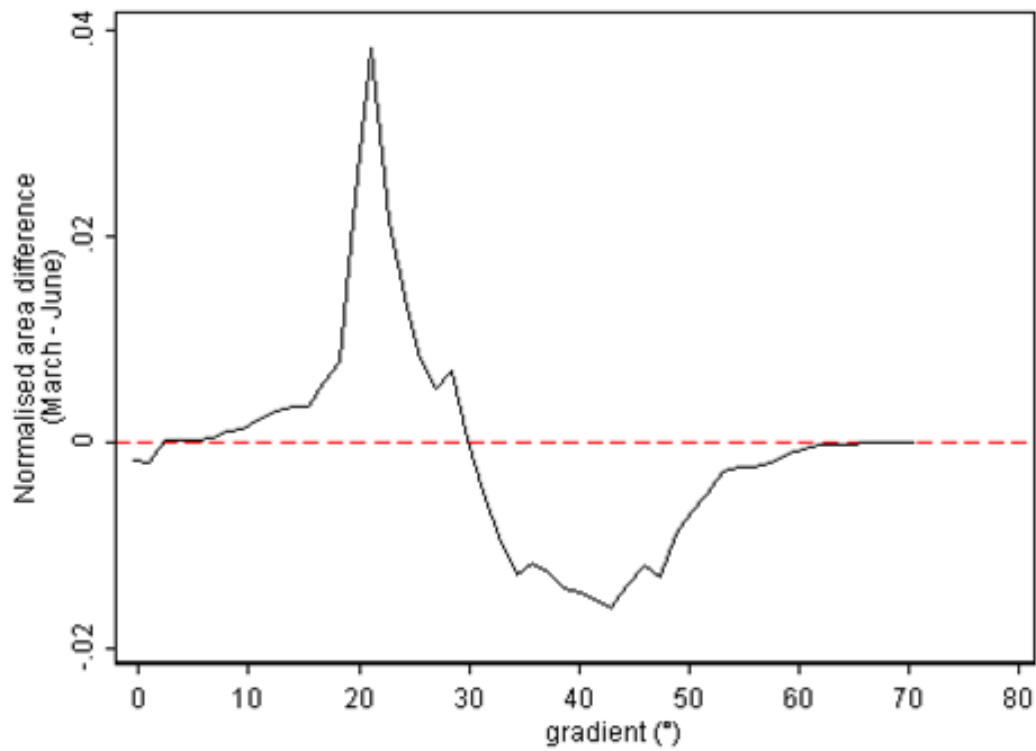


Figure 3.23: Normalised difference plot based on landslide area distributions for June 2008 and March 2009 (see Figure 3.25a). The red dashed line indicates the point at which both June and March landslide areas are equally distributed.

Local elevation

Local elevation provides a measure of elevation at a point with respect to the surrounding hillslope catchment. Raw elevation data is representative of the whole mountain range, however the processes that this study is concerned with occur at the catchment level. Local elevation values are calculated relative to the range of elevation within a defined search radius, thus providing an indication of where landslides are occurring within a hillslope catchment.

To calculate local elevation for this dataset a search radius of 4 km was selected to reflect the distance from valley bottom to mountain peak, ensuring that the longer hillslopes were represented. Using the *Neighbourhood* function in *ArcMap: Spatial Analyst Tools*, the sample grid was used to evaluate the absolute height of each grid cell and the minimum elevation within a 4 km range of that cell. The difference between these is the local elevation. The resulting data were then classified into 100 m bins and both normalised area plots and density distribution curves were produced (Figures 3.24 and 3.25).

The normalised distribution of landslide areas closely follows the distribution of all areas for each time interval, indicating a fairly even distribution of landslides across the catchment. There is a slight undersampling of landslides at areas of higher elevation values in June 2008, which is not seen in previous data for this time period (Parker, 2010). This is also shown in the landslide density plot, which decreases with increasing elevation beyond a value of 700 m. This highlights the value of a smaller study area as the differences noticed here are smoothed out by data which covers the entire earthquake affected zone (Parker, 2010).

By March 2009 the undersampling of landslides at higher elevations was no longer apparent. In the March distribution (Figure 3.24) the two normalised plots are most closely matched, supporting the notion that post-seismic failures exhibit a more uniform distribution across the catchment compared to co-seismic failures (Meunier and Hovius, 2006). This is also seen in the landslide density plots for October and March, which exhibit an increase in density relative to June, over a wide range of local elevation values.

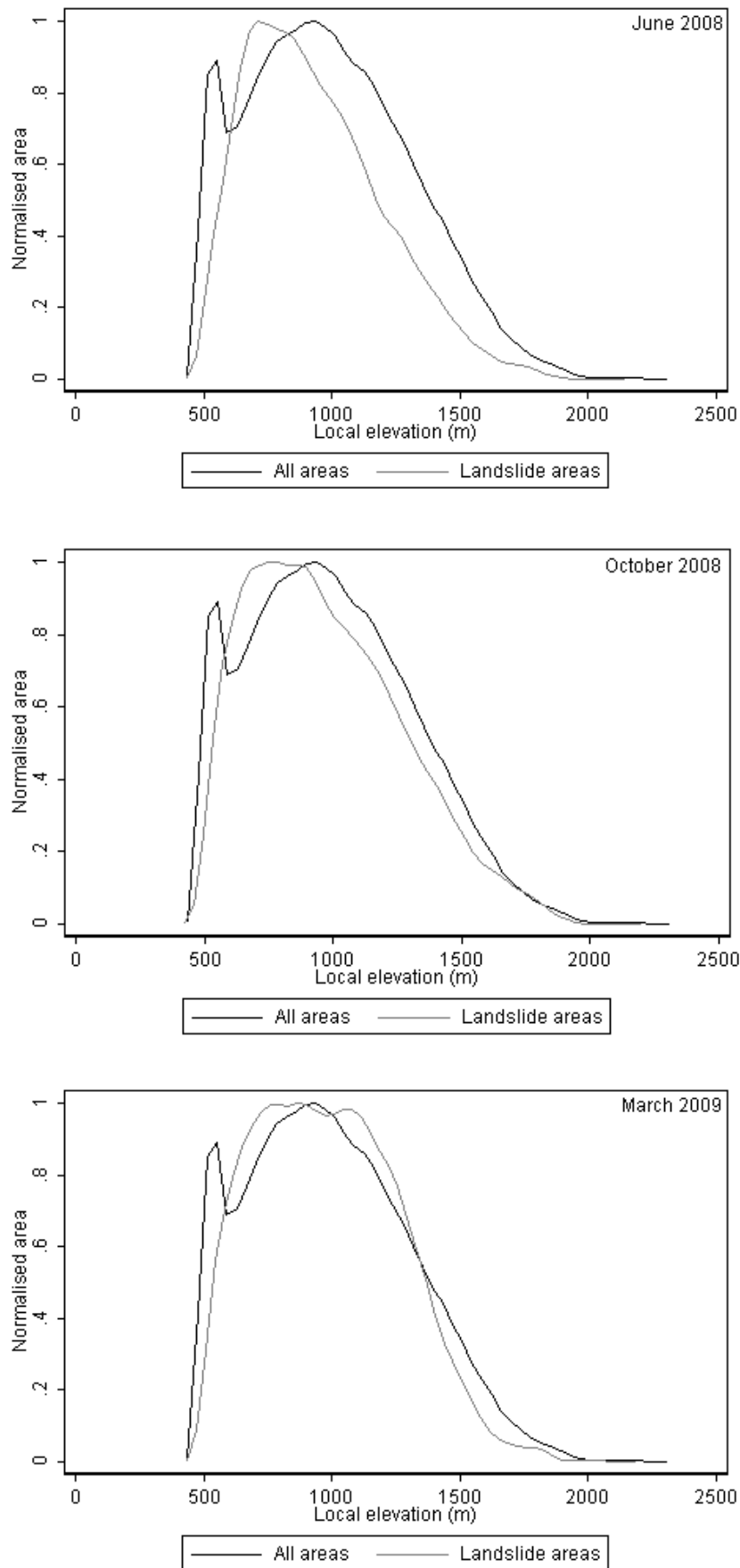


Figure 3.24: Normalised areas plots for the distribution of all areas and landslide areas across local elevation in June 2008, October 2008 and March 2009.

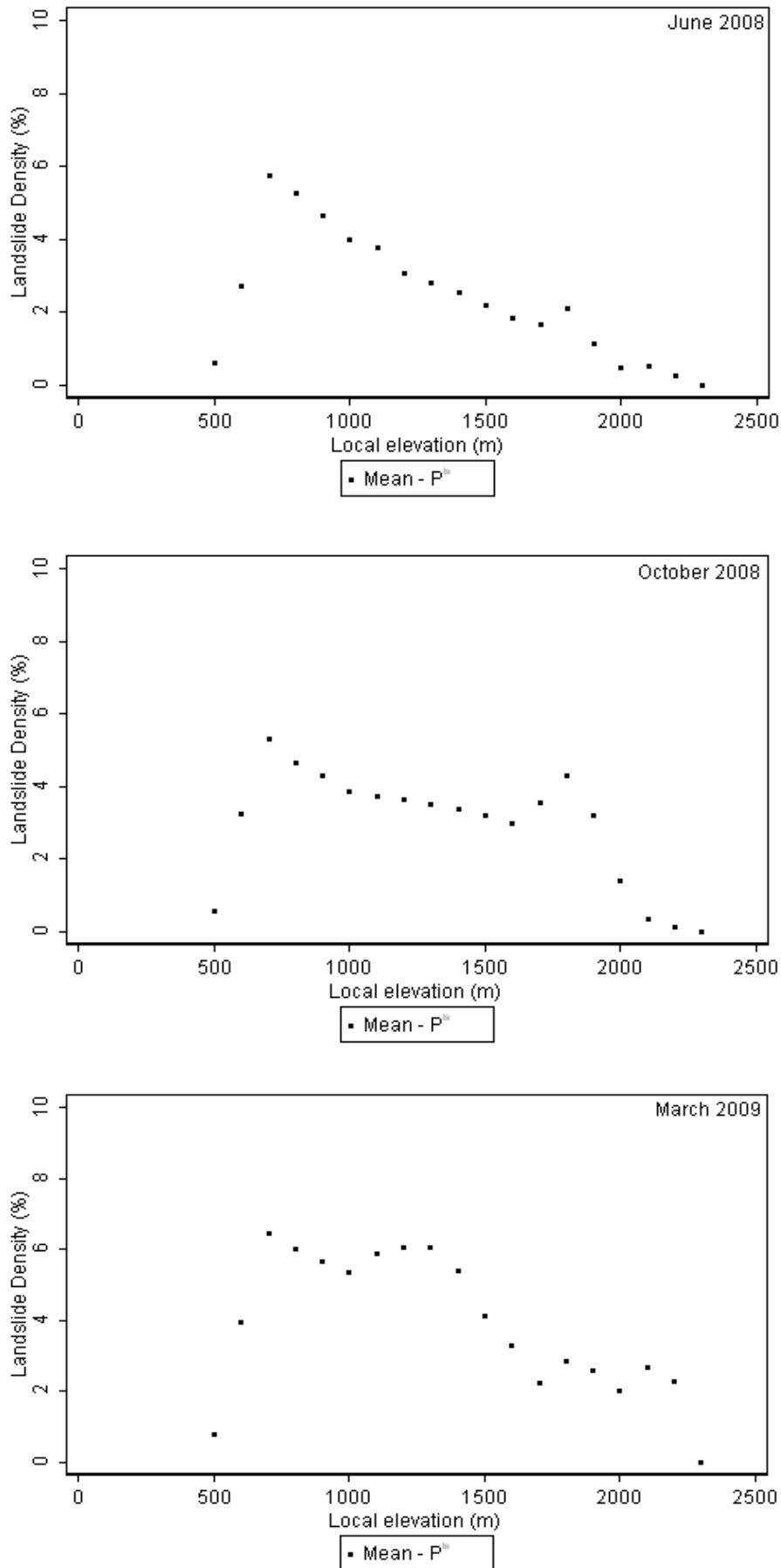


Figure 3.25: Landslide density distribution plots sampled in 100 m bins.

Geology

The pattern of landslide distribution relative to geological unit is commonly evaluated in studies of controls upon both seismic and non-seismic landsliding (see Keefer 1999; Keefer 1984). The structure of the rock, its composition and rock mass strength, determine its potential to fail when a trigger occurs, such as seismic shaking or heavy rainfall. Due to the variations between rock types each geological unit is likely to respond differently to the impact of multiple triggering factors (Yamagishi *et al.*, 2008).

In order to examine the relationship between landslide distribution and geological unit, a geological map of the region was compared with the landslide density maps (Figure 3.26). To allow for statistical analysis of the distribution, the 11 different geological units were digitised as polygons and landslide density data extracted through the sample grid. Normalised area plots were produced showing the distribution of different lithologies across both the whole study area and the landslide areas (Figure 3.27). Similarly, Figure 3.28 shows the landslide density distribution across these 11 units. Finally, Figure 3.29 examines the temporal change of landslide density for each geological unit.

The normalised area plot for co-seismic landslides (June 2008 data) displays a noticeably higher than average density of landsliding in Cambrian, Triassic, Devonian, Permian and Stenian geologies. Conversely a lower than average density of landslides is seen in the Jurassic and Quaternary units. This supports results of a recent study of this area (Yin *et al.*, 2010) which identified Cambrian rocks as particularly susceptible to co-seismic landsliding and the Jurassic and Quaternary units to have a particularly low rate of landsliding. For this study region the pattern also correlates fairly well with distance from the fault; those units with higher rates of landsliding are closer to the surface rupture as can be seen in the map of geologic units (Figure 3.26). An assessment of landslide density with age of geological unit (Figure 3.28b) shows a positive relationship in accordance with results from Parker (2010).

Overall, landslide density increased between June 2008 and March 2009, particularly in Cambrian, Ordovician, Carboniferous and Silurian geologies (Figure 3.28a and Figure 3.29). In the Jurassic and Triassic units a clear decrease in landslide density is noticed between June 2008 and March 2009, suggesting that widespread post-seismic landsliding did not occur in these units. Yamagishi *et al.* (2008) found that few rainfall-induced landslides occur in sandstone materials, which is a major lithological component of both the Jurassic and Triassic units in this region, thus supporting the suggestion that post-seismic landsliding did not occur here.

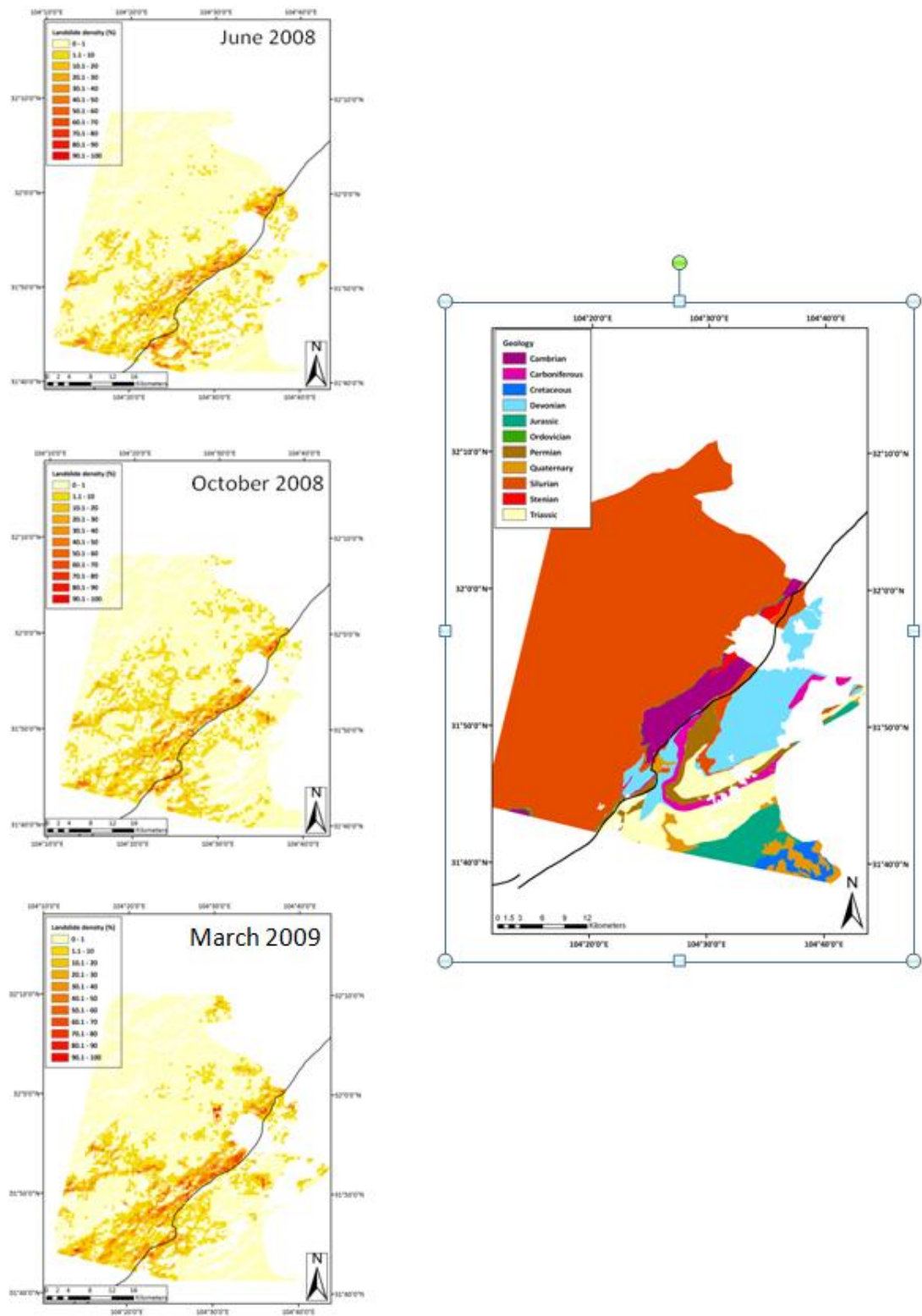


Figure 3.26: 500 m landslide density maps (left) and map of geological units (right)

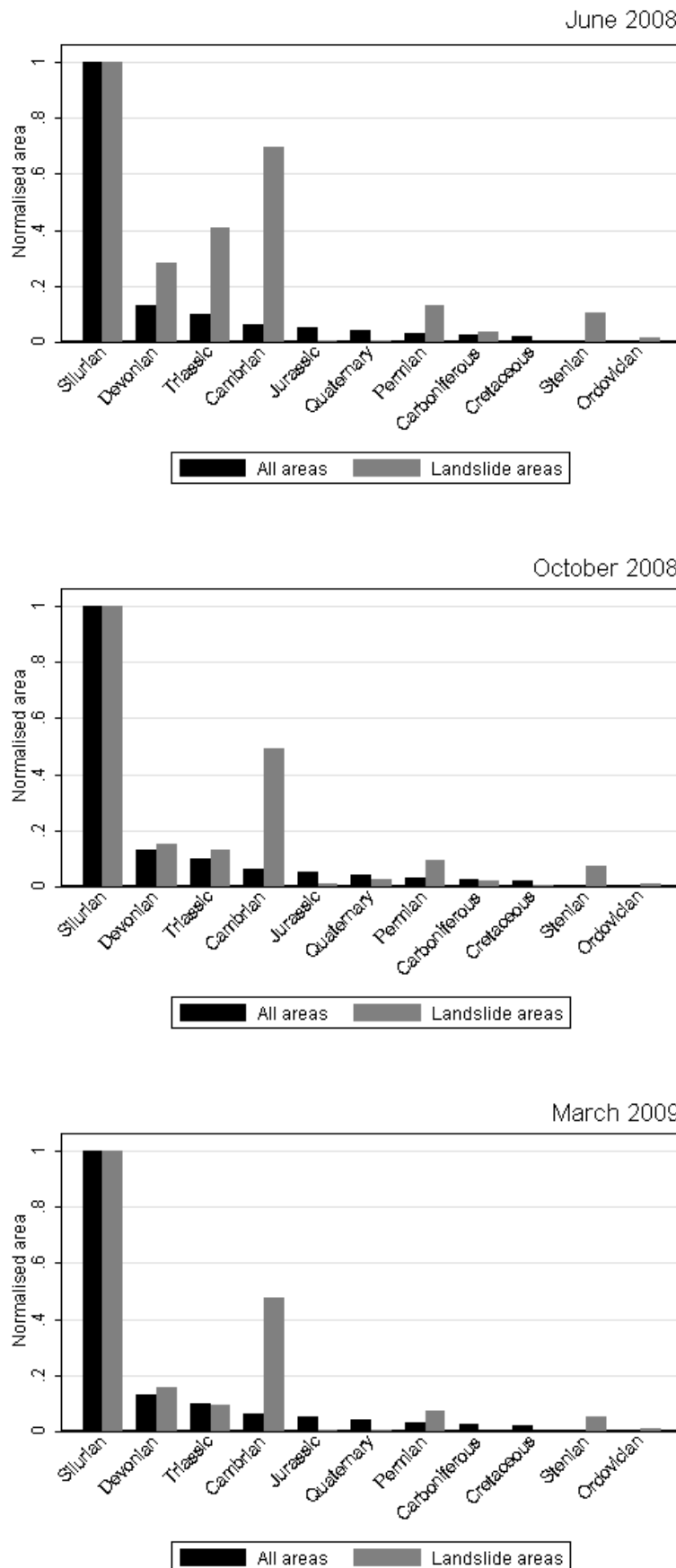


Figure 3.27: Normalised area plots for the distribution of all areas and landslide areas across geological units in June 2008, October 2008 and March 2009.

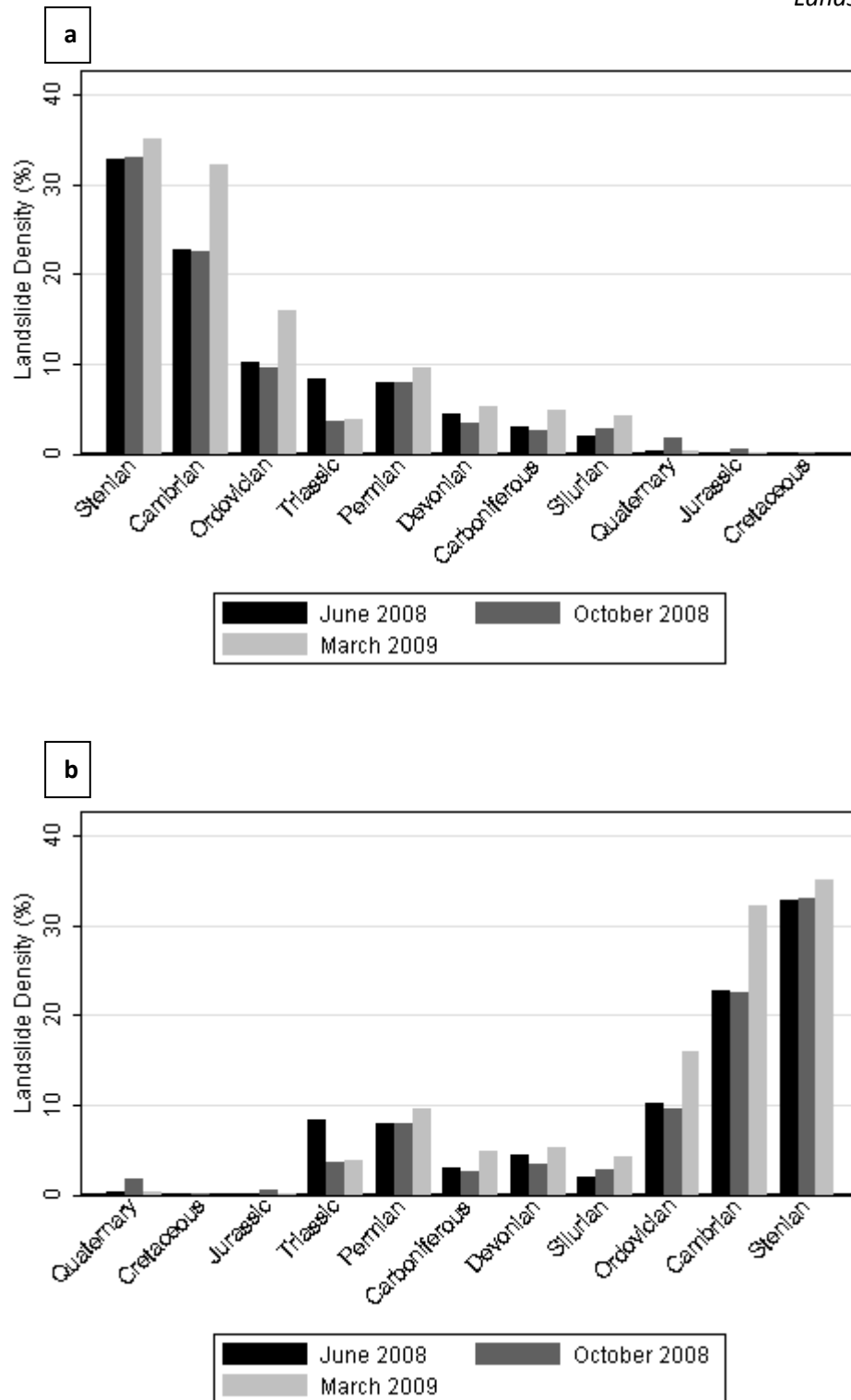


Figure 3.28: Landslide density distribution plots for June 2008, October 2008 and March 2009 across geological units: **a** – in order of decreasing landslide density; **b** – in order of geological unit age.

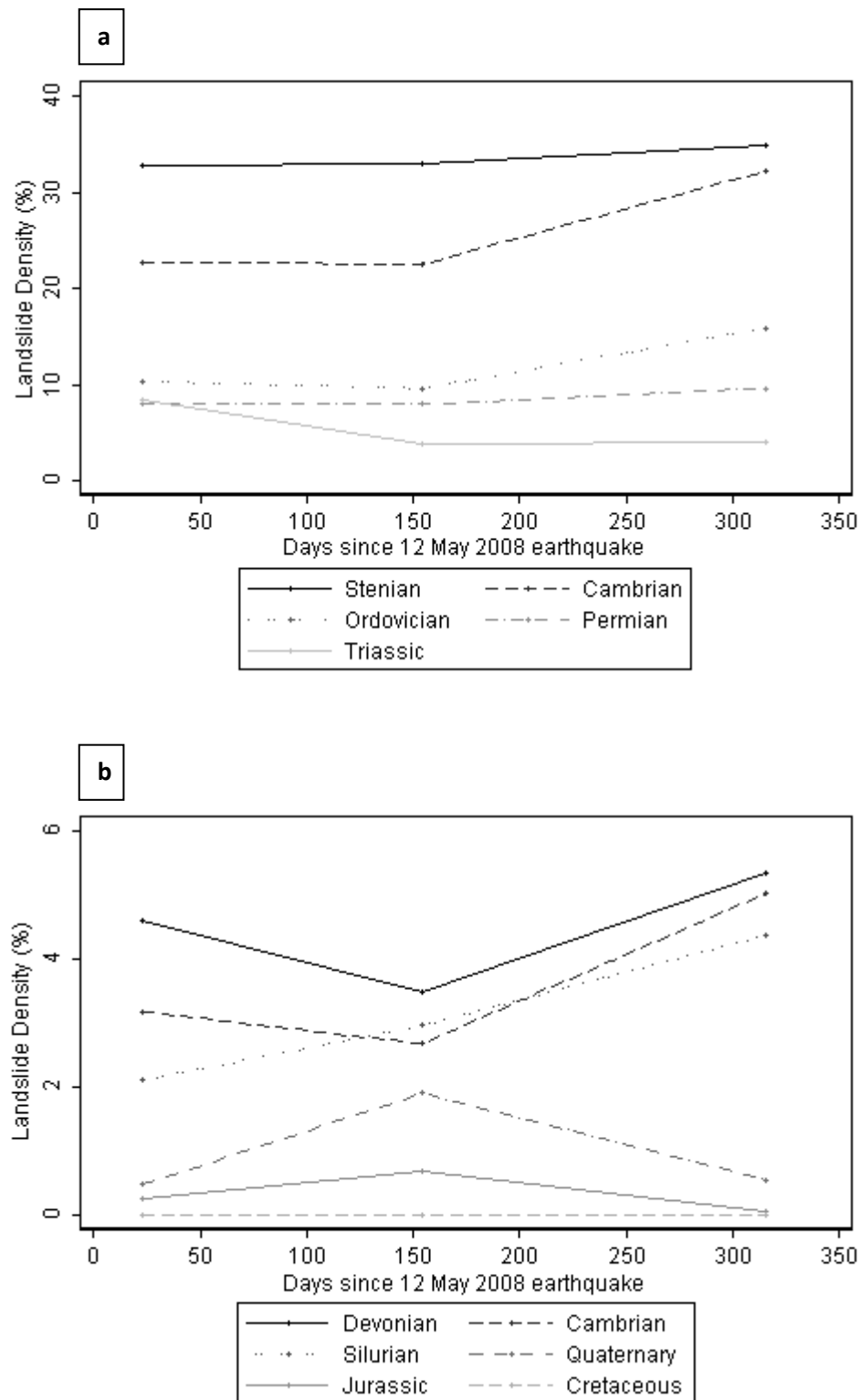


Figure 3.29: Plots of temporal change in landslide density for each geological unit. Note the different scales used on the y-axis of each graph: **a** – geological units with an overall higher landslide density (> 5 %); **b** – geological units with an overall lower landslide density (< 5 %)

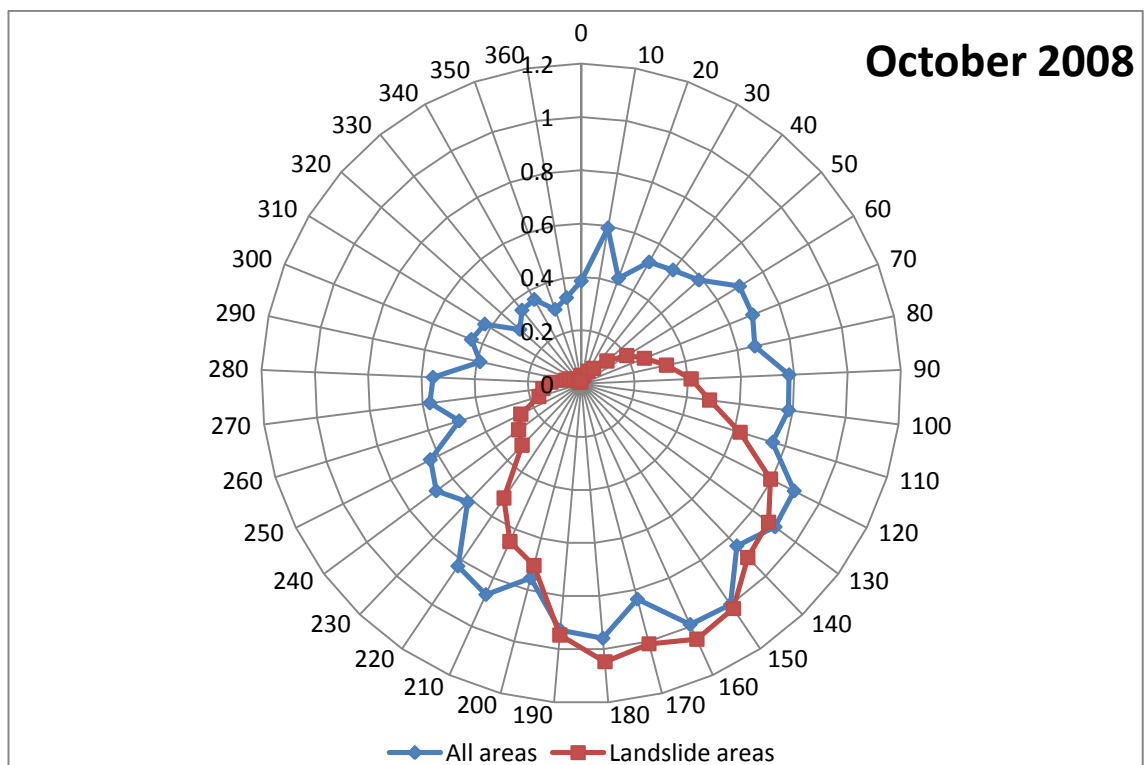
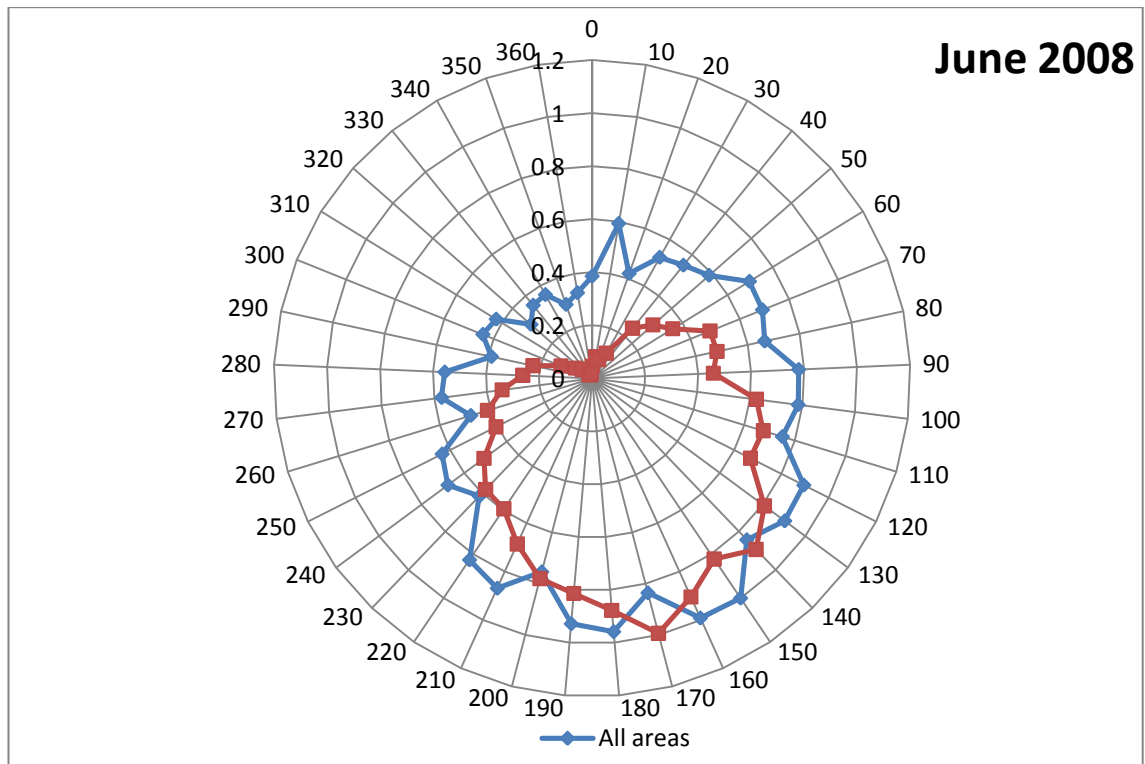
Aspect

According to Meunier *et al.* (2008), landslides tend to have a preferential aspect. The processes which link aspect with earthquake-related landslide occurrence are two-fold: firstly the direction of the movement of seismic waves causes slopes with an opposing aspect (i.e. those facing the oncoming seismic waves) to have a larger potential for failure (Chang *et al.*, 2007); secondly, the sub-aerial processes acting on the hillslope vary with aspect, resulting in variations in vegetation growth, soil strength and thus the potential for erosion (Chang *et al.*, 2007). In addition, certain aspects receive more rainfall due to the orographic effects in mountainous regions, thus increasing the likelihood of slope failure, particularly post-seismically.

To investigate this relationship between aspect and landslide occurrence the 30 m sample grid was used to obtain the aspect (in degrees) for each grid cell. These data were resampled into 10° aspect bins and plots were produced on radar graphs to visually display the landslide distribution. Normalised area plots are presented in Figure 3.30 based on the mean values of landslide density for each 10° bin.

Previous studies of earthquake-induced landsliding in the Wenchuan earthquake have noted that overall co-seismic landslides preferentially occurred on slopes facing south-east, i.e. slopes in the hanging wall facing the fault rupture (Chang *et al.*, 2007). This trend is shown in the normalised area plot for June 2008 (Figure 3.30) where it can be seen that areas of higher than average landslide density were found on slopes between 140° and 170° and all other slopes, particularly those facing north-west, displayed a lower than average landslide density. As a large proportion of the failures were located in the hanging wall (see Figure 3.20), then the areas of highest landslide occurrence (south-east facing) are primarily facing the co-seismic fault rupture.

Between June, October and March the distribution of landslide areas became focused on slopes within a marginally smaller range of aspect values facing in a south-easterly direction (Figure 3.30). This is the aspect of slopes regarded as most impacted upon by the seismic shaking of the Wenchuan earthquake and therefore supports the idea that the impact of an earthquake continues to affect the spatial location of landslides long after the event (Chang *et al.*, 2007). Conversely the narrower distribution of post-seismic failures disagrees with the findings of studies from other areas that report a wider distribution of post-seismic and rainfall induced failures compared to co-seismic failures (Chang *et al.*, 2007).



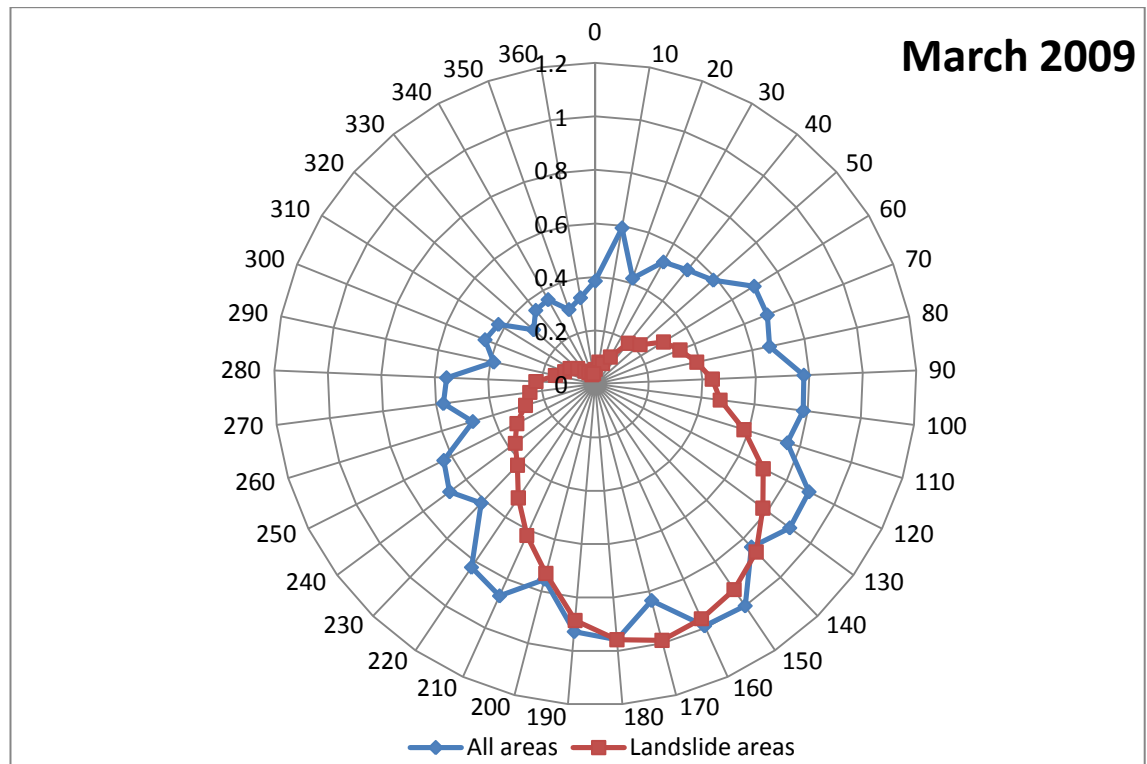


Figure 3.30: Normalised area plots for the distribution of all areas and landslide areas, sampled in 10° aspect bins.

4. Landslide volumes and erosion rates

Landslides are important as an immediate hazard to slopes and valleys below them and as a long-term driver of landscape change because of the material that they displace (Huang and Li, 2009; Korup *et al.*, 2009; Densmore *et al.*, 1997). Calculating volumetric estimates allows this material to be constrained, aiding our understanding of the material both as a short-term hazard and its longer-term impact on landscape evolution. This chapter presents the results of volumetric estimations of both co-seismic and post-seismic landslide material in the Beichuan area following the 2008 Wenchuan earthquake.

4.1. Methods

Although a range of scaling relationships to calculate volume from area currently exist (see Table 2.1; Guzzetti *et al.*, 2009; Larsen *et al.*, 2010), a scaling law specific to the Beichuan region was developed to avoid any significant error in subsequent estimates of erosion which can occur when applying a scaling relationship outside the region it was developed in (Larsen *et al.*, 2010). In order to quantify the relationship between volume and area for Beichuan, a combination of fieldwork measurements and imagery analysis were used.

Fieldwork

Based on the results of the landslide inventory maps and information from other studies (Parker, 2010; Huang and Li, 2009), areas of interest were identified as potential field sites. Eight locations were chosen for a combination of the following reasons:

- Areas of very high density landsliding;
- Areas that displayed significant change between June 2008 and March 2009;
- Areas of different geology;
- Areas which were safely accessible.

Figure 4.1 shows a map of the individual fieldwork locations; the grey boxes outline the eight areas initially identified. As is evident from the map, these sites are mostly located along the valley floors, next to the river. This was primarily due to accessibility constraints as areas further north-west in the Longmen Shan were cut off by landsliding. However the field sites used were all very close to the Beichuan fault line and thus enabled data collection from both the hanging wall and footwall of the fault.

Field data collection is necessary to assess landslide characteristics and to take measurements that cannot be obtained from satellite imagery (Bucknam *et al.*, 2001). With regards to

developing a relationship between volume and area of landslides in the Beichuan area, this relied upon fieldwork to obtain estimates of landslide scar depth. This also ensured reliable estimates of landslide volume – within the errors and constraints of the field measurements – when applying the scaling law as its formulation has been supported by field data (Hovius and Stark, 2002).

Measurements of scar depth for smaller failures were obtained using a *LaserAce Hypsometer*, which returns the distance between the laser and the target, calculated as half the time of flight (Geosolution, 2006). Therefore the difference between the landslide scar and undisturbed ground was calculated as a measurement of landslide depth (see Figure 4.2). The maximum range of the laser is 150 m: where landslide scars were at a distance > 150 m, estimates of depth were made. The estimates were determined by three people in the field in order to reduce the bias judgement of one estimation. In total, the depths of 41 landslide scars were estimated and each failure recorded with a GPS point to enable identification on the landslide inventory map and satellite imagery.

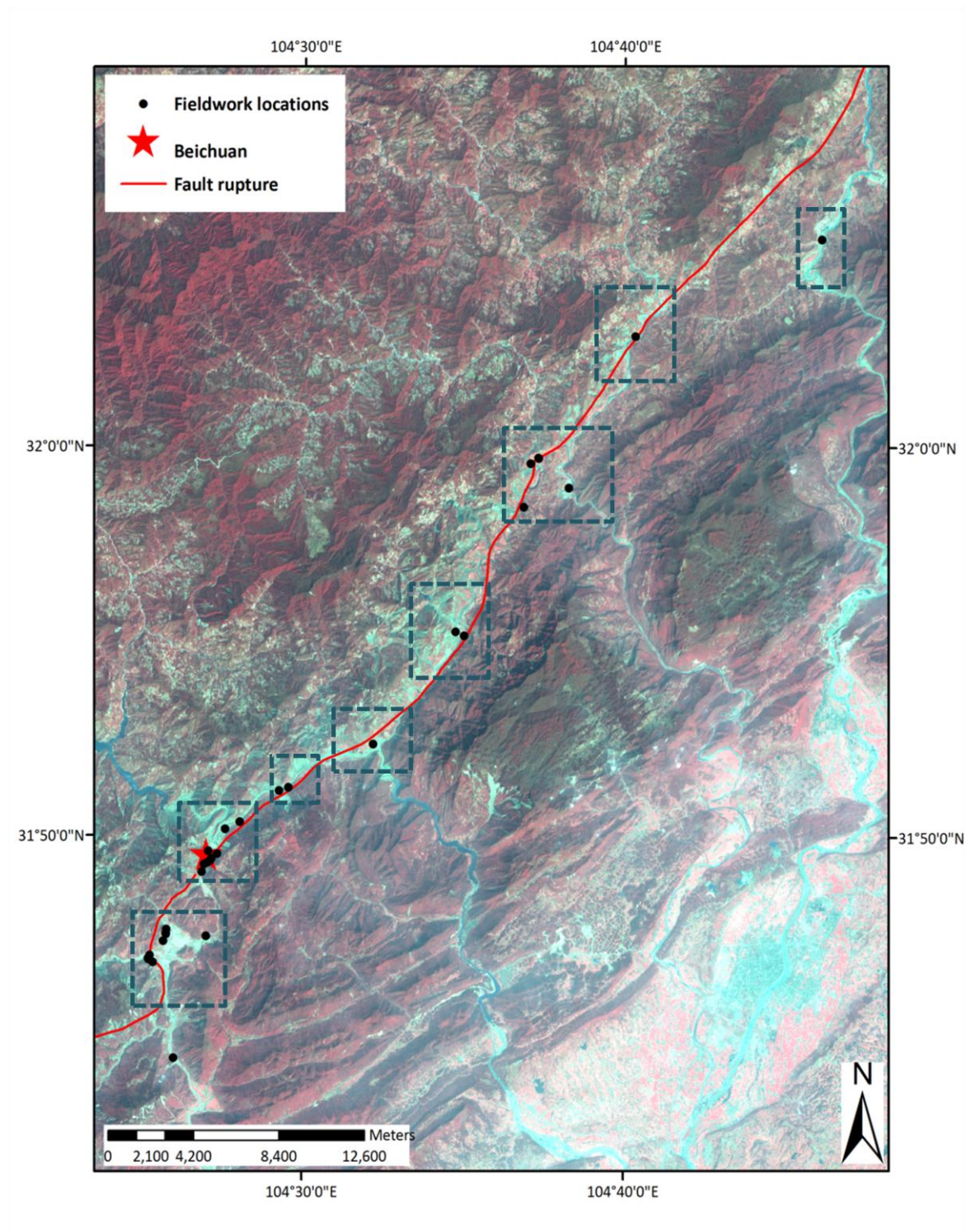


Figure 4.1: Fieldwork locations (represented by the black dots) displayed on a SPOT 5 multispectral image from March 2009. The grey boxes outline the areas initially identified for fieldwork, from SE to NW: Leigu; Beichuan, northern end of Beichuan new town; Huangjiaba; Chenjiaba; Fenghuang & Guixi; south Pingtong; north of Pingtong towards Nanba.

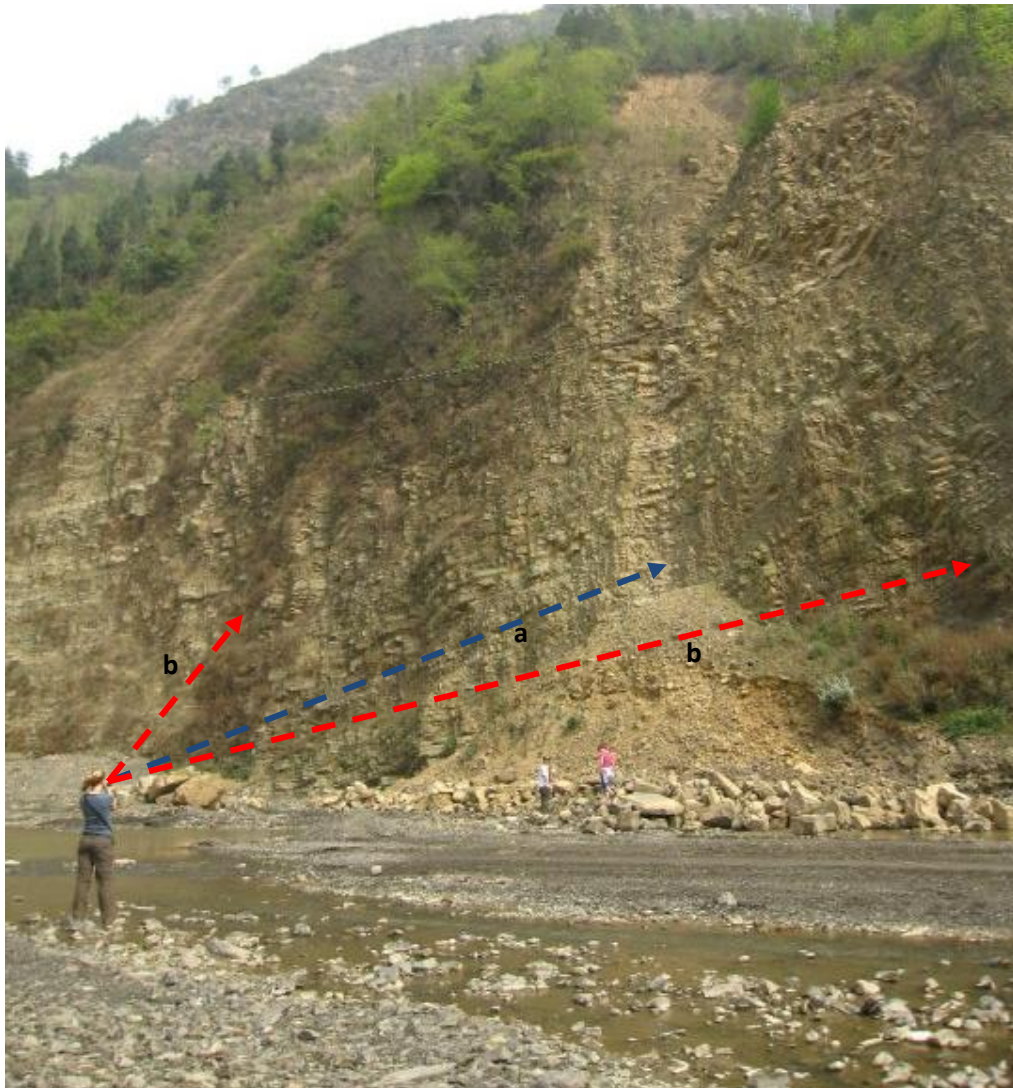


Figure 4.2: An annotated field photograph to illustrate the measurement of scar depth using the LaserAce Hypsometer. Beams were fired at the rock surface; in the centre of the landslide scar (a) and at the same elevation on undisturbed ground (b). The difference between the distance of a and b (calculated as half the time of flight) provides a measure of landslide scar depth.

Image analysis

It was not possible to obtain accurate measurements of landslide area in the field, therefore satellite imagery was employed. Using the GPS points taken in the field, individual failures were easily identified on the imagery and *ArcMap Tools: Measure* was used to measure the planimetric area of each one. Image S1 was used primarily for this task as it has a high spatial resolution (5 m) and provides the initial area of the co-seismic failures. In the case of post-seismic failures, image S3 was used instead.

Formulating a scaling law

The volume, V (in m^3) of material generated by landslides can be estimated using landslide area, A (in m^2) and average depth, D (in m) (Martin *et al.*, 2002). Adopting this basic principle in the form $V = A \cdot D$, estimates of landslide volume were calculated for the 41 failures measured in the field. Stata 11 was used to perform linear regression in order to determine the relationship between volume and area. In order to account for the multiple orders of magnitude covered by the data, both volume and area were log-transformed and linear regression performed on these values. From these results it was then possible to fit a scaling law to the data as an equation of the form $V = \beta \cdot A^\alpha$ (Guzzetti *et al.*, 2009), allowing estimates of landslide volume (m^3) based on landslide area (m^2).

4.2. Results

Linear Regression

Linear regression of $\log(V)$ with $\log(A)$ reveals the following relationship:

$$\log(V) = -0.974 + 1.388(\log(A)) \quad (4.1)$$

Using simple rules of logarithms, this relationship can be put into the form of a scaling relationship:

$$V = 0.1062 \cdot A^{1.388} \quad (4.2)$$

with a standard error of the scaling exponent (α) = 0.087. A plot of the area and estimated volume for the 41 failures measured in-field is shown on a log-log graph (Figure 4.3). Imposed upon this is a line representing the volume-area relationship defined by Equation 4.2. The plot displays a good fit of the original data to the scaling law, which is supported by an R^2 value = 0.86 and a Root Mean Square Error = 0.308. The few landslides with a calculated volume notably larger or smaller than the scaling law estimate were investigated to assess landslide

characteristics, location and geology. No pattern was found in any of these categories and therefore those failures can be classed as anomalous results. In addition it should be noted that the failure with the largest difference between calculated and estimated volume still remains within an order of magnitude from the scaling law estimate: with $A = 6,310 \text{ m}^2$, $V_{\text{calc}} = 3,160 \text{ m}^3$ and $V_{\text{est}} = 19,950 \text{ m}^3$.

Hanging wall and footwall trends

Individual scaling relationships were developed for failures in the hanging wall and footwall to determine if the scaling law for the whole dataset (equation 4.2) was suitable for both areas, and also to establish whether the relationship between volume and area was significantly different between the hanging wall and footwall.

Figure 4.4 displays the same data as seen in Figure 4.3, however the failures have been distinguished according to which side of the fault line they are located on. The separate scaling laws for each dataset are also displayed along with the R^2 values, indicating the strength of the relationship. Visual inspection of the plot shows that both datasets exhibit a trend very similar to the original scaling law (Equation 4.2), suggesting that it is not necessary to define separate scaling laws for each side of the fault. In addition, only a marginal difference can be seen between the hanging wall and footwall data trends, signifying that the volume-area relationship is not significantly different between the two. Based on this evidence and the reliable fit of the original scaling law, it is reasonable to adopt Equation 4.2 as the scaling law for the entire study region.

Comparison with other scaling laws

A comparison of the volume-area relationship for Sichuan with other volume-area relationships is shown in Figure 4.5. Line lengths are representative of the range in landslide area values over which the relationship was developed, with the exception of Sichuan (this work) which has been extrapolated to extend over the entire data range. The equations representing these relationships were obtained from a variety of literature sources: Larsen *et al.* (2010); Guzzetti *et al.* (2009; 2008); Rice *et al.* (1969); Simonett (1967) – see Table 2.1 for more detail on the data sources). The plot shows a very similar trend in volume-area relationships for six of the nine that are displayed. Slight disparity between these six trends is seen only at the upper end of the graph, i.e. $A > 10^7 \text{ m}^2$; here it becomes harder to evaluate the agreement between the trends because few data are collected from failures of this size and therefore the relationships shown are mostly extrapolations of scaling laws developed

based on only smaller failures. The three volume-area relationships that differ from the Sichuan data are those displayed in blue (Larsen *et al.*, 2010 – soil; Rice and Foggin, 1971; Rice *et al.*, 1969), which are all based on data collected from soil landslides only. This difference is shown more clearly in Figure 4.6, which presents the same data over the smaller area range than this work was based on ($10^3 - 2 \times 10^5 \text{ m}^2$). The volume-area relationship for Sichuan fits almost identically to that developed by Larsen *et al.* (2010) based on bedrock landslides, and produces a close fit to the relationship developed by Guzzetti *et al.* (2009), which calculates marginally larger volumes. The relationship based on soil landslides from Larsen *et al.* (2010) estimates landslide volumes approximately one order of magnitude lower than the other relationships for landslides with $A \geq 10^5 \text{ m}^2$.

In addition to the differences described above, the six volume-area relationships that display a similar trend and exhibit a steep gradient larger than 1, which serves to illustrate that failures with a larger area produce a greater sediment volume, proportional to their size, than failures with a smaller area. The three volume-area relationships based on soil landslides exhibit a shallower line gradient, however it is still greater than 1, meaning that large failures remain disproportionately high in volume.

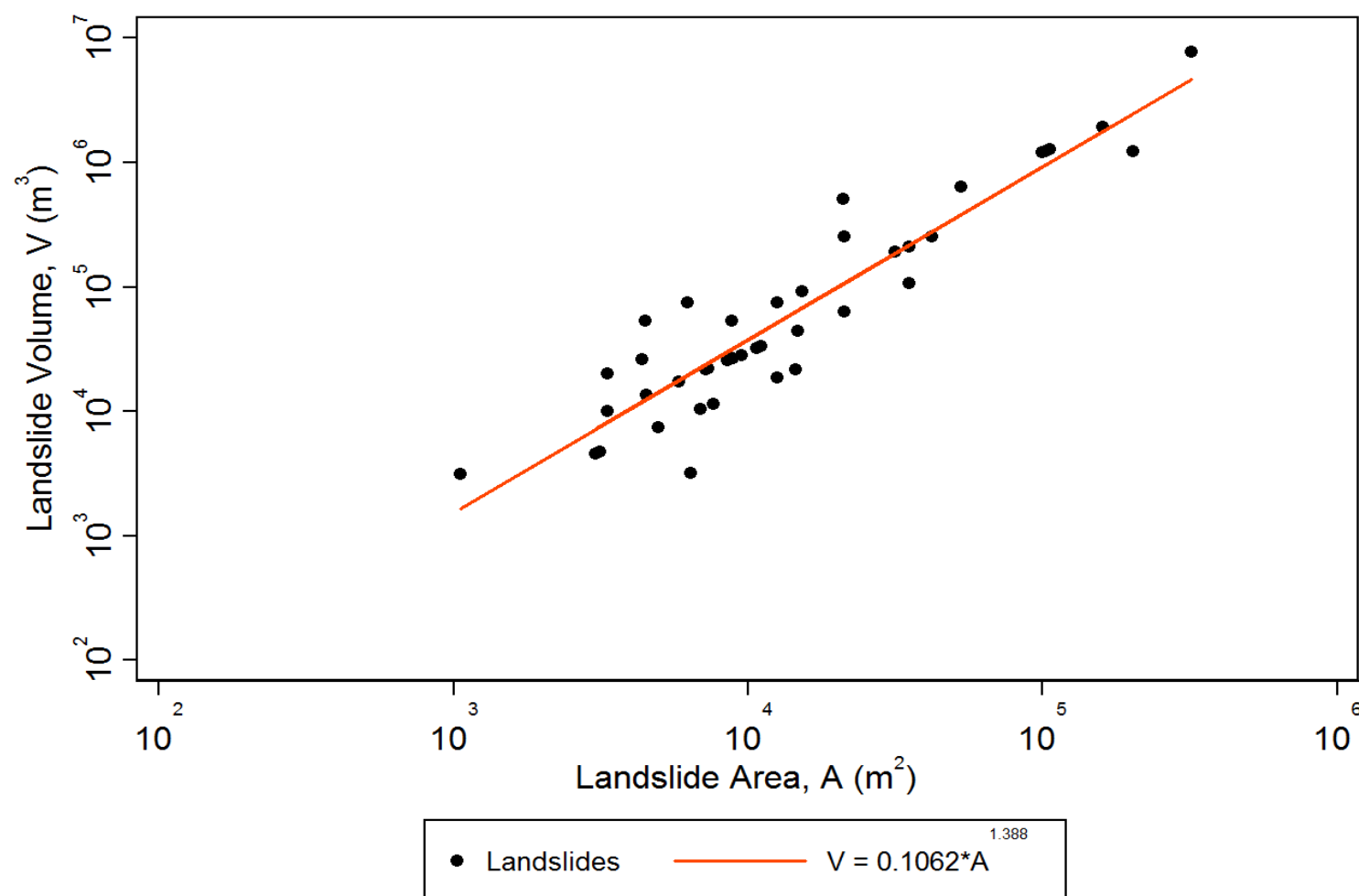
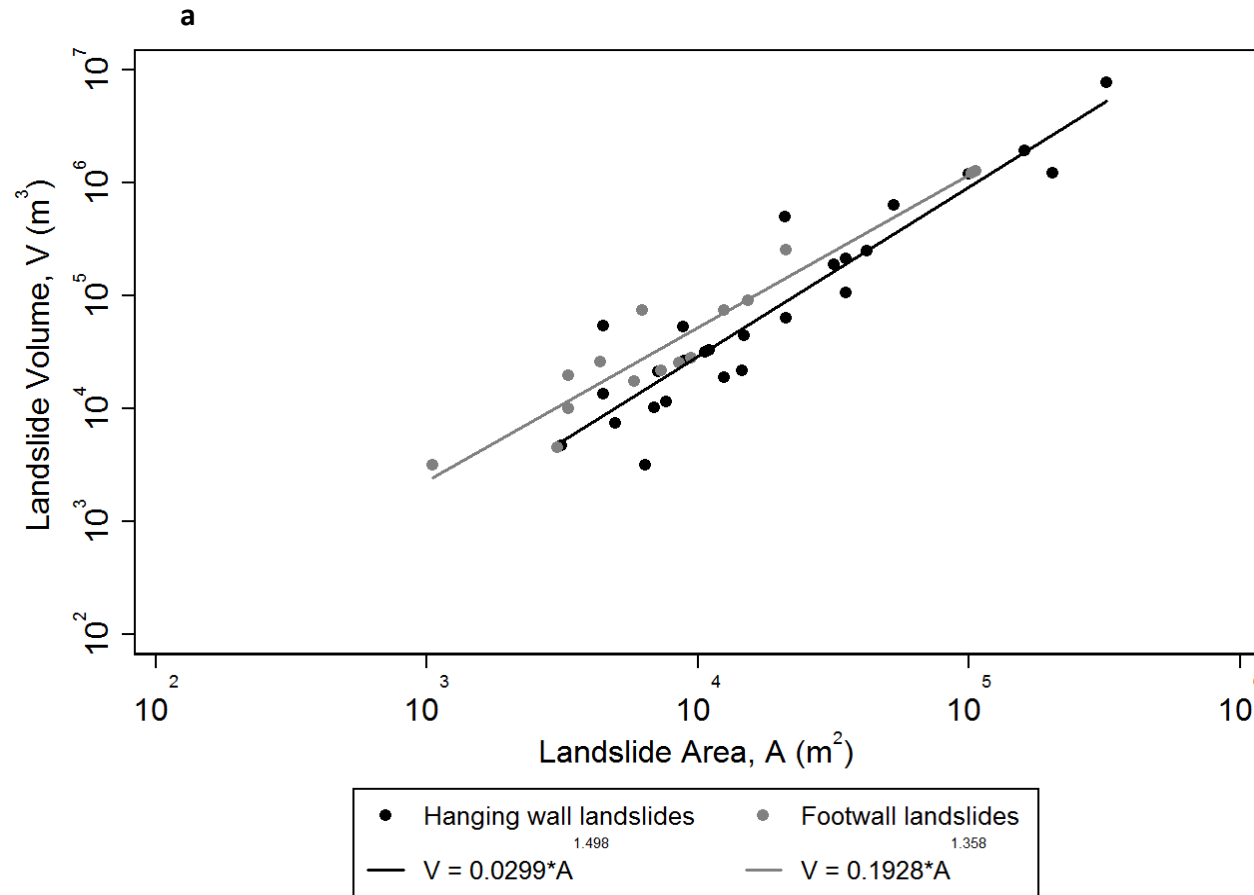


Figure 4.3: Log-log graph displaying the landslide area (A , m^2) and calculated landslide volume (V , m^3) of the 41 failures measured in-field. The red line represents the volume-area relationship as defined by the scaling law: $V = 0.1062 \cdot A^{1.388}$.

**b**

	Scaling law	R^2 value
Hanging wall	$V = 0.0299 \cdot A^{1.498}$	0.87
Footwall	$V = 0.1928 \cdot A^{1.358}$	0.92

Figure 4.4: **a** - Log-log graph displaying the landslide area (A , m^2) and calculated landslide volume (V , m^3) of the 41 failures measured in-field: the failures have been identified as either 'Hanging wall landslides' (black dots) or 'Footwall landslides' (grey dots). The volume-area relationships for failures on each side of the fault are represented by lines of the respective colours. **b** – The table displays the scaling laws used to define the volume-area relationships and associated R^2 values to illustrate their significance.

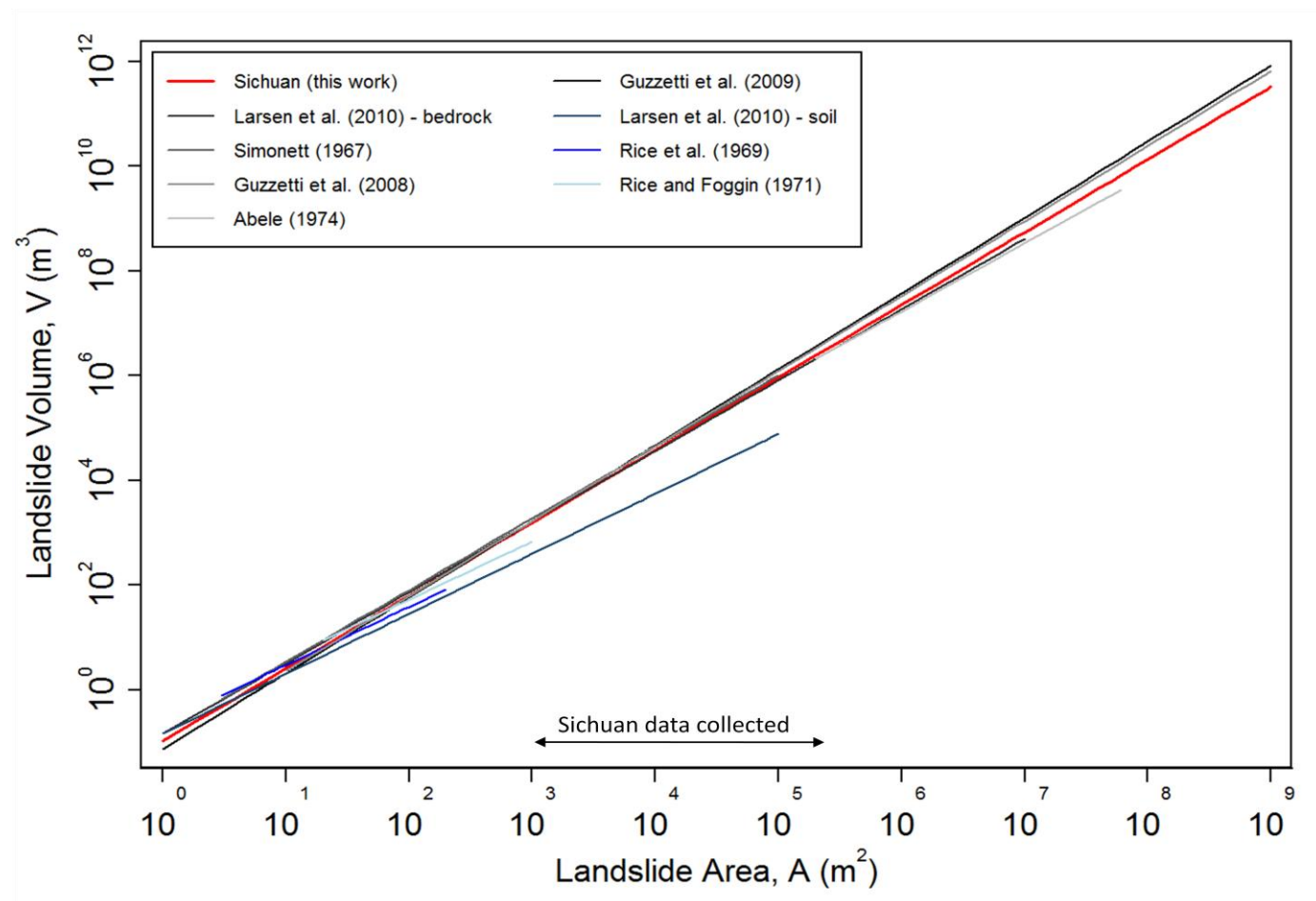


Figure 4.5: A log-log graph displaying relationships linking landslide area (A , m^2) and landslide volume (V , m^3) from various literature sources. The red line represents the relationship developed for Sichuan in this work. For more detail on the data sources and the equations that describe the relationships see *Table 2.1*.

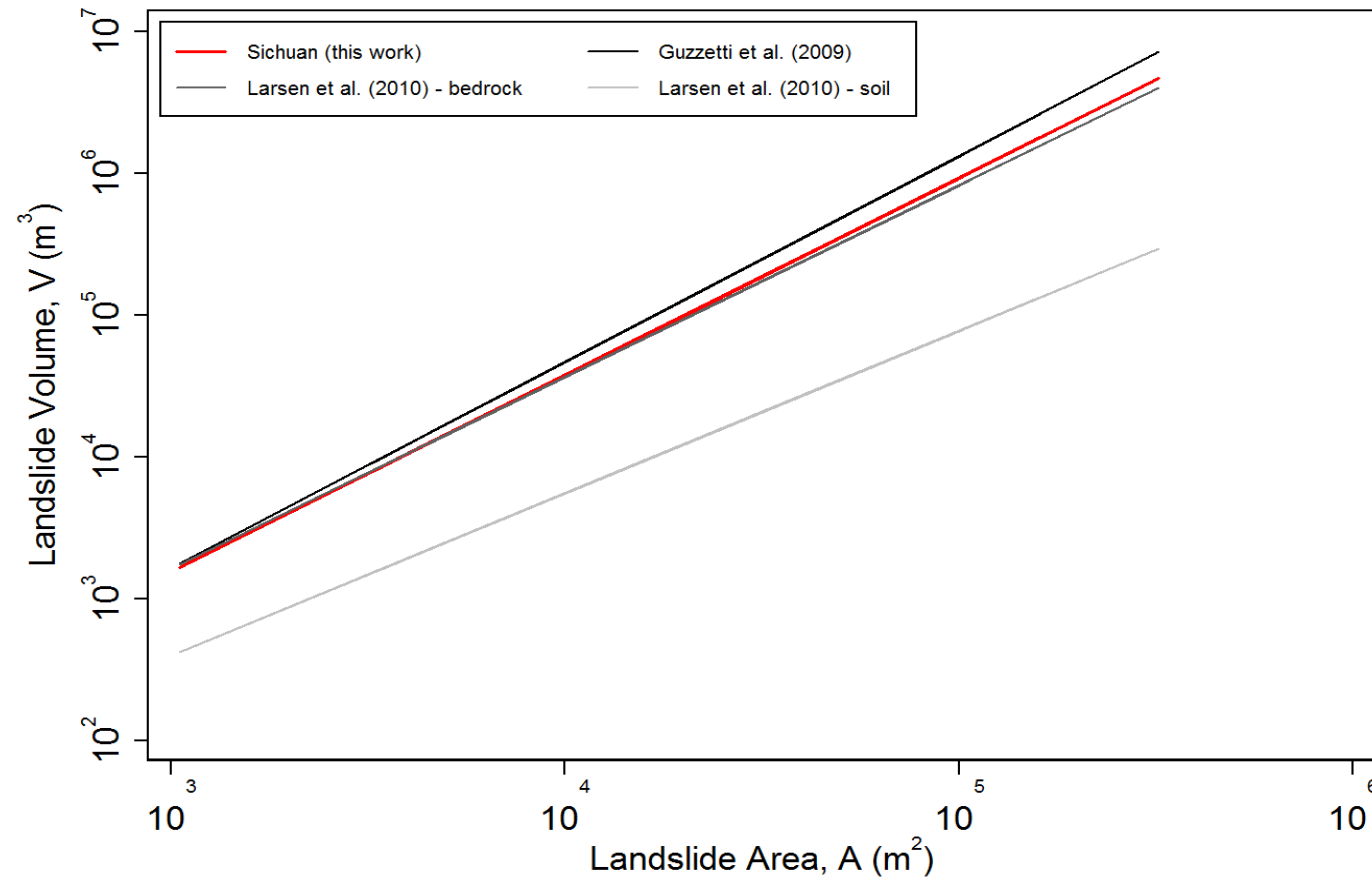


Figure 4.6: A log-log graph displaying 4 of the relationships shown in Figure 4.5 over a smaller data range, representative of the data collected in Sichuan (this work), i.e. $10^3 m^2 \leq A \leq 10^{5.5} m^2$. The red line represents the relationship developed for Sichuan in this work. For more detail on the data sources and the equations that describe the relationships see Table 4.1.

4.3. Application

The application of a volume-area scaling law to an area of landsliding can provide a quantitative estimate of the total volume of landslide material and also of the impact of an event, through the calculation of an mean erosion rate over a set time period. Guzzetti *et al.* (2009) provided an example of this by applying their scaling law to the Collazone area, central Italy. They demonstrated its function in calculating the volume of individual landslides, evaluating total landslide volume for the region, estimating landslide mobilisation rates, and determining the magnitude of individual landslide events.

For the Beichuan area, Equation 4.2 was applied to evaluate the change in volume of material produced from June 2008 to March 2009, to quantify the regional erosion rate, and to assess the influence of different geologic units on landslide volume.

4.3.1. Total landslide volume

Individual landslide areas (m^2) were evaluated for each landslide map using the *Calculate Geometry* function in ArcMap. Applying Equation 4.2, landslide volume (m^3) was calculated for each failure on the June 2008 landslide map and for each new failure on the subsequent October 2008 and March 2009 landslide maps. These calculations were repeated using the scaling laws from Guzzetti *et al.* (2009) and Larsen *et al.* (2010). The results of total landslide volume (m^3) alongside each respective equation are shown in Table 4.1; they most likely represent an upper bound on the volume estimation as area (A) was calculated for the whole landslide (i.e. scar and deposit) and therefore is expected to overestimate mobilized landslide volume (Guzzetti *et al.*, 2009).

Incremental change

Co-seismic landslides generated the largest volume of material as shown by the total landslide volume recorded for June 2008 of $5.91 \times 10^8 \text{ m}^3$. Post-seismic landslides that occurred between June and October 2008 generated a much smaller volume of material: $1.68 \times 10^8 \text{ m}^3$, which is approximately 28% of the co-seismic landslide volume. Subsequent post-seismic landslides that occurred between October 2008 and March 2009 generated a further $2.29 \times 10^8 \text{ m}^3$ of material, approximately 39% of the co-seismic landslide volume. These volumes only represent the study area of this investigation ($1.87 \times 10^3 \text{ km}^2$), which is 1.4 % of the total area affected by landsliding following the 2008 Wenchuan earthquake (based on a total affected area of 811 km^2 , from Dai *et al.*, 2010). However, the volume of co-seismically generated material for this study area alone is, for comparison, an order of magnitude higher than the

total estimates of co-seismic landslide sediment volume for the 1999 Chi-Chi earthquake, Taiwan (Chuang *et al.*, 2009).

Thus, initial post-seismic landsliding in this region that has occurred within five months of the earthquake event has generated the equivalent of almost one third of the co-seismic material again, and beyond this the volume of failures has continued to increase. This suggests significant potential for on-going changes to sediment production in this area. In an investigation following the 1999 Chi-Chi earthquake, Lin *et al.* (2006) suggested that the approach taken to assess temporal changes in sediment production should incorporate the responses to both initial (i.e. seismic) and subsequent (i.e. post-seismic rainfall) events. The results presented in Table 4.1 clearly provide support to that suggestion and highlight the need for this more complex approach.

Comparing scaling relationships

Comparison of the estimated volumes for the four scaling laws, including the relationship established in this work (Table 4.1), supports the trends noticed from visual inspection of Figures 4.5 and 4.6, confirming the very close agreement between the bedrock landslides relationship of Larsen *et al.* (2010_{rock}) to Sichuan (this work) and the significant difference seen with the Larsen *et al.* (2010) relationship based on soil landslides. This is as expected because the scaling law developed for Sichuan was based on predominantly bedrock landslides; only five of the forty-one measured failures were limited to soil landslides. It is reasonable to assume that this ratio of bedrock to soil landslides is representative of the study area: Larsen *et al.* (2010) investigate 4,231 landslides worldwide and note a transition from soil to predominantly bedrock landslides for $10^3 \text{ m}^2 \leq A \leq 10^5 \text{ m}^2$, which matches the landslide area range of the data collected in Sichuan. In addition, general fieldwork observations recognised predominantly bedrock landslides at all field sites.

The difference in volume estimations between this work (Equation 4.2) and other scaling laws is proportionally larger in June 2008 than in October 2008 or March 2009 (Table 4.1). For example, comparing the first two rows of data in Table 4.1 reveals that the volume estimate according to Guzzetti *et al.* (2009) is 54.1 % higher than this work for June 2008; 33.3 % higher for October 2008; and 35.4 % higher for March 2009. Similar trends are seen when comparing this work with the lower estimates from Larsen *et al.* (2010). Due to the changing scaling dependency of volume from area with increasing landslide size (Guzzetti *et al.*, 2009), i.e. landslides with a larger area produce a disproportionately larger volume, these results suggest

that the co-seismic failures recorded in June 2008 were on average larger and therefore deeper than subsequent post-seismic failures. This is in line with observations from Hovius and Stark (2002): storm triggered landslides are typically more limited to shallow depths, while earthquake triggered landslides are characteristically more deep-seated failures.

Table 4.1: Total landslide volume, calculated using the volume-area scaling relationships displayed in Figure 4.6. Column 1 lists the source of the established relationship; column 2 lists the equations (scaling laws) which describe the volume-area relationships; and column 3 list the results obtained from applying the scaling laws to the areas of landsliding identified on the three landslide maps (see Chapter 3).

Jun-08 represents the time from 12/05/2008 – 04/06/2008; Oct-08 represents 04/06/2008 – 13/10/2008; Mar-09 represents 13/10/2008 – 24/03/2009

Source	Scaling law	Total landslide volume (m ³)		
		Jun-08	Oct-08	Mar-09
Sichuan (this work)	$V = 0.1062 \cdot A^{1.388}$	$5.91 \cdot 10^8$	$1.68 \cdot 10^8$	$2.29 \cdot 10^8$
Guzzetti et al (2009)	$V = 0.0740 \cdot A^{1.450}$	$9.11 \cdot 10^8$	$2.24 \cdot 10^8$	$3.1 \cdot 10^8$
Larsen et al (2010)	$V_{\text{rock}} = 0.1458 \cdot A^{1.350}$	$5.04 \cdot 10^8$	$1.57 \cdot 10^8$	$2.11 \cdot 10^8$
Larsen et al (2010)	$V_{\text{soil}} = 0.1458 \cdot A^{1.145}$	$4.18 \cdot 10^7$	$2.06 \cdot 10^7$	$2.71 \cdot 10^7$

4.3.2. Regional erosion rates

Erosion rates are commonly based on three variables – volume of material (m^3) mobilised over a given area (m^2) in a certain period of time (yr), which are all components of the standard equation:

$$\text{Erosion rate } (m \text{ yr}^{-1}) = \text{volume/area/time} \quad (4.3)$$

Erosion rates provide a quantitative indication of the nature and magnitude of geomorphic processes acting on the landscape (Jen *et al.*, 2006). Importantly, they can be applied over any time frame (as time is a variable in equation 4.3) and therefore can be used to indicate both the short-term and long-term impact of an erosion event. However this is erosion based on a single event and must not be confused with long-term average erosion rates over many events. Two erosion rates were calculated for this study: regionally-averaged erosion and landslide-averaged erosion:

$$\text{Regional erosion rate } (m \text{ yr}^{-1}) = \text{volume of material } (m^3) / \text{study area } (m^2) / \text{time (yr)} \quad (4.4)$$

$$\text{Landslide erosion rate } (m \text{ yr}^{-1}) = \text{volume of material } (m^3) / \text{landslide area } (m^2) / \text{time (yr)} \quad (4.5)$$

The regional erosion rate indicates the amount of total denudation per year averaged across the entire landscape. The landslide erosion rate indicates the denudation averaged across landslide areas only. Whilst this is clearly counterbalanced by many areas where no (or minimal) erosion has occurred, the landslide erosion rate provides a useful indication of the geomorphic impact of the landslides. For regional and landslide erosion time is taken as the temporal period covered by the data providing a short-term erosion rate for this study area. Results of the application of equations 4.4 and 4.5 to the volume data produced are shown in Table 4.2. As the volume estimates most likely represent an upper bound on landslide volume, then the erosion rate will also represent an upper bound.

Incremental change

Regionally-averaged erosion is most commonly used in assessments of erosion due to landsliding (i.e. Guzzetti *et al.*, 2009; Martin *et al.*, 2002). Therefore the results of regional erosion (based on equation 4.4) will be used to examine the changes with time following the 2008 Wenchuan earthquake.

Within each time frame displayed in Table 4.2 (June 2008, October 2008 and March 2009), area remains constant in calculating the erosion rate, and volume varies according to the results from different scaling laws. Thus the variation in erosion rates that is seen within each time frame reflects the same variations seen in calculations of total landslide volume. This further illustrates the impact of the scaling law(s) used and enforces the warning raised by Larsen *et al.* (2010): that significant error in erosion estimates can occur when applying a scaling relationship outside the region it was developed in. Therefore, focusing on the results from the scaling law developed for this work, the following temporal changes are seen in short-term erosion rates: firstly a significant decrease of greater than one order of magnitude from 6.238 m yr⁻¹ in June 2008 to 0.311 m yr⁻¹ in October 2008; secondly a comparatively small change between October 2008 and March 2009 shown by an increase of approximately 10 %, from 0.311 m yr⁻¹ to 0.343 m yr⁻¹.

A short-term erosion rate of 6.238 m yr⁻¹ for the June 2008 period (12/05/2008 to 04/06/2008) indicates a very high volume of co-seismic failures and a large amount of erosion over a very short time frame. With the understanding that this erosion rate does not reflect a time-averaged process, but that rather the majority of failures in this period would have occurred almost instantaneously following the earthquake, it seems somewhat meaningless to average the erosion over this time. In effect, the time variable can be removed from equation 4.4 to give a measure of denudation (i.e. landscape lowering):

$$\text{denudation (m)} = \text{volume of material (m}^3\text{)} / \text{study area (m}^2\text{)} \quad (4.6)$$

This illustrates the impact of an event by quantifying the total erosion for a single time frame. The results of applying equation 4.6 to June 2008 and the two subsequent time periods are shown in Table 4.3. Denudation has also been calculated for landslide areas only, providing an indication of average landslide depth (m). Regional denudation for June 2008 suggests an average lowering of 0.393 m across the landscape as a result of co-seismic landsliding. Subsequently, post-seismic landsliding between June and October 2008 contributed to a further 0.112 m of denudation; and a further 0.152 m of denudation occurred between October 2008 and March 2009. Reinforcing what was indicated by the results of the volume calculations, this also illustrates the magnitude of the seismic event and the significance of continued post-seismic failures.

Comparing regionally- and landslide-averaged denudation

Regional denudation is reflective of the total volume of material generated by landsliding and provides a quantitative estimate of this with respect to the extent of the study area; in this case the study area is of equal size for all three time periods. Conversely, the area that landslide denudation is based upon varies between time periods, dependent on the total planimetric area of the landslides. Therefore the resulting measures of landslide denudation effectively equate to average landslide depth (m), providing an indication of the mean geomorphic work done by all failures.

A similar temporal pattern is seen in both measures of denudation (Table 4.3): a significant decrease from June 2008 to October 2008 and a relatively smaller increase from October 2008 to March 2009. However the difference between each temporal period is more exaggerated in the regionally-averaged denudation compared to the landslide-averaged denudation. Estimates of regional denudation display a 71.5 % decrease between June and October 2008 compared to a 56.7 % decrease in estimates of landslide denudation; the increase in regional denudation from October 2008 to March 2009 is calculated as 35.7 %, compared to a much smaller increase in landslide denudation of 3.9 %.

These results show that differences in both landslide depth and total landslide area account for the changes seen in regionally-averaged denudation amounts. Between June 2008 and October 2008 (i.e. co-seismic and post-seismic time periods) the difference in landslide depth appears to be the primary controlling factor on denudation; there is a 56.7 % difference in average landslide depth during this time period, compared to a 71.5 % difference in regionally-averaged denudation. Landslide depth appears to exert less of a control over the post-seismic difference in regional denudation from October 2008 to March 2009, with only a 3.9 % increase in landslide-averaged denudation compared to a 35.7 % increase in regionally-averaged denudation. This provides further evidence for the distinctions in depth and therefore volume between co-seismic and post-seismically triggered landslides, such as the observations from Hovius and Stark (2002), that storm triggered (post-seismic) landslides are typically shallower than co-seismic failures.

Table 4.2: Erosion rates (m yr^{-1}) calculated from landslide volume estimates using equations 4.4 and 4.5; rates are based on the temporal period covered by the data (i.e. from May 2008 to the date shown).

Source	Scaling law	Regional erosion rate (m yr^{-1})			Landslide erosion rate (m yr^{-1})		
		Jun-08	Oct-08	Mar-09	Jun-08	Oct-08	Mar-09
Sichuan (this work)	$V = 0.1062 \cdot A^{1.388}$	6.238	0.311	0.343	169.33	73.25	76.19
Guzzetti et al (2009)	$V = 0.0740 \cdot A^{1.450}$	9.616	0.415	0.465	261.01	97.66	103.14
Larsen et al (2010)	$V_{\text{rock}} = 0.1458 \cdot A^{1.350}$	5.320	0.291	0.316	144.40	68.45	70.20
Larsen et al (2010)	$V_{\text{soil}} = 0.1458 \cdot A^{1.145}$	0.441	0.038	0.041	11.98	8.98	9.02

Table 4.3: Denudation (m) based on landslide volume estimates: Regional denudation = total landslide volume (m^3)/total study area (m^2); Landslide denudation = total landslide volume (m^3)/total area of landslides (m^2).

Source	Scaling law	Regional denudation (m)			Landslide denudation (m)		
		Jun-08	Oct-08	Mar-09	Jun-08	Oct-08	Mar-09
Sichuan (this work)	$V = 0.1062 \cdot A^{1.388}$	0.393	0.112	0.152	10.67	4.62	4.80
Guzzetti et al (2009)	$V = 0.0740 \cdot A^{1.450}$	0.606	0.149	0.206	16.45	6.15	6.50
Larsen et al (2010)	$V_{\text{rock}} = 0.1458 \cdot A^{1.350}$	0.335	0.104	0.140	9.10	4.31	4.42
Larsen et al (2010)	$V_{\text{soil}} = 0.1458 \cdot A^{1.145}$	0.028	0.014	0.019	0.755	0.566	0.569

4.3.3. Geologic influence

Within the extent of the study area for this work there are 11 recognised geological units: Cambrian, Carboniferous, Cretaceous, Devonian, Jurassic, Ordovician, Permian, Quaternary, Silurian, Stenian and Triassic. The influence of geology on the distribution and magnitude of landslides is recognised by many previous studies (Owen *et al.*, 2008; Parise and Jibson, 2000; Keefer, 1999 and many more), and therefore it is expected that variations in landslide volume would be found in accordance with areas of different geology. Qualitative field observations support this idea as clear differences in the shape and depth of landslides was noticed in different geologic units along the fault rupture.

Fieldwork data

The 41 landslides measured in the field cover five different geological units, as shown in Figure 4.7. From visual inspection of the plot it can be seen that failures in Quaternary rocks are all relatively small landslides: area (A) $\leq 10^4 \text{ m}^2$ and volume (V) $\leq 10^5 \text{ m}^3$. However, no further trends are visible as the failures in the other four geological units all have a range of areas from $< 10^4 \text{ m}^2$ to $> 10^5 \text{ m}^2$. The greatest scatter of data is seen in failures from the Silurian rock, which range in area from $3.14 \times 10^3 \text{ m}^2$ to $1.60 \times 10^5 \text{ m}^2$.

It is probable that the lack of association between volume and geology seen in this data is due to the small sample size (41). Additionally, this plot only analyses five of the eleven geological units. Therefore the scaling relationship developed for all units and landslide volumes across the entire study area (equation 4.2) was used to assess the relationship between landslide volume and each of the eleven geological units.

Full study area analysis

The total landslide volume contained within each geological unit was calculated using equation 4.2, where area (A) is the planimetric area obtained from the landslide inventory maps. Landslide volume was calculated for each time period (June 2008, October 2008 and March 2009) in order to observe temporal changes in the relationship between volume and geology. The results are presented in Figure 4.8, which expresses the landslide volume of each unit as a percentage of the total landslide volume for the full study area.

In all three time periods more than 50 % of the total landslide volume is distributed within the Cambrian and Silurian units, whilst less than 10 % of the total landslide volume is contained in each of the following units: Stenian, Ordovician, Devonian, Carboniferous, Quaternary, Jurassic and Cretaceous. Differences between the distribution of co-seismic and post-seismic volumes

are evident in the comparison of June 2008 and March 2009 data. The volume of landslide material generated co-seismically (calculated from the June 2008 image data) is more widely distributed among the different units compared to the volume of landslide material generated post-seismically (calculated from the March 2009 image data). Approximately 50 % of the volume of co-seismic landslide material is distributed between two geological units – Cambrian and Silurian; the remaining 50 % is distributed over a further seven geological units. In contrast, almost 70 % of the volume of post-seismic landslide material is distributed between the Cambrian and Silurian units; the remaining 30 % of landslide material is found primarily in the Permian unit, with less than 15 % of the total landslide volume in March 2009 distributed over a further six geological units. This suggests that the geological influence on landslide volume is greater for post-seismic (i.e. rainfall induced) failures than for seismically triggered failures.

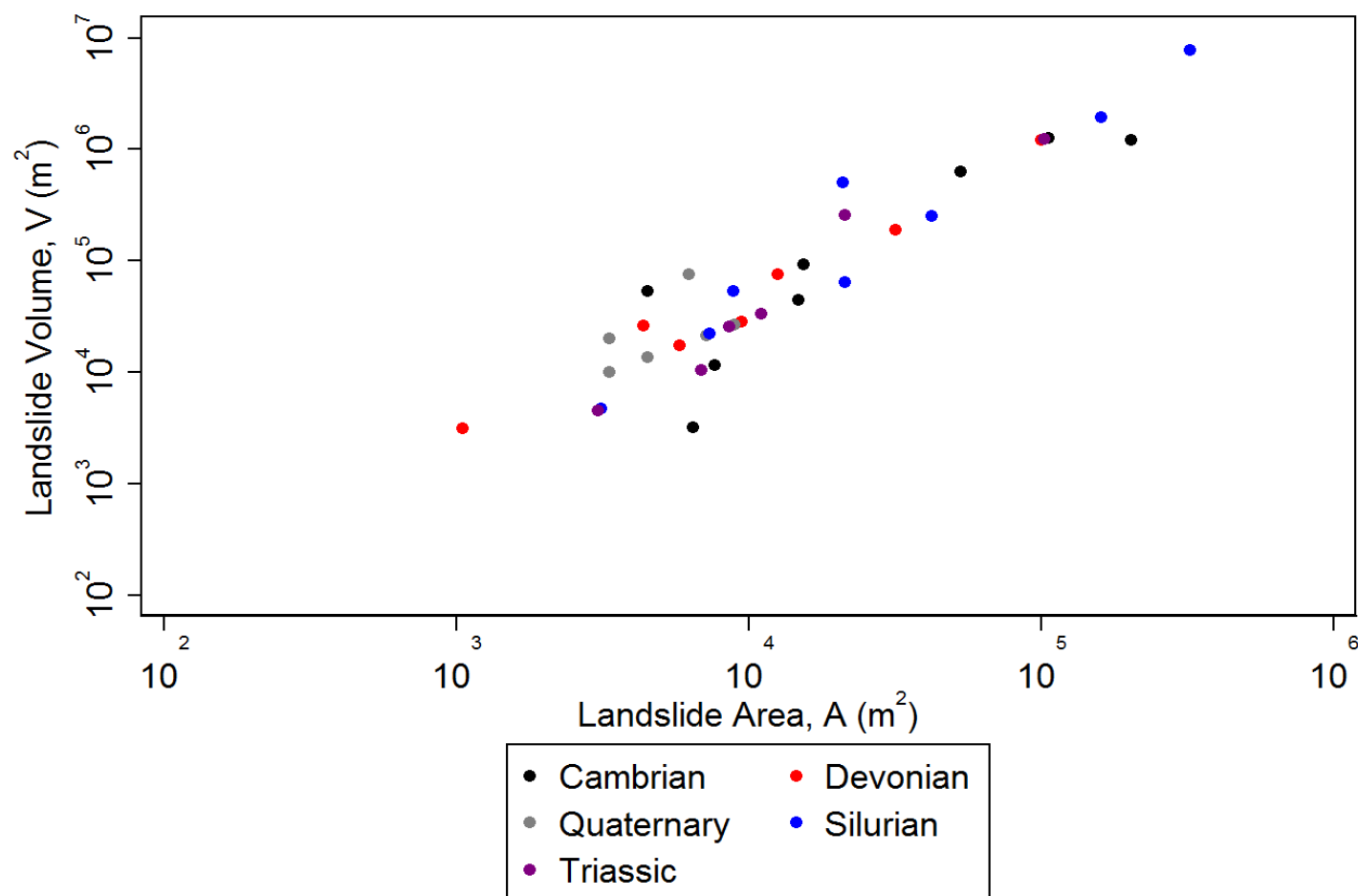


Figure 4.7: A log-log plot of the landslide area (A , m²) and calculated landslide volume (V , m³) of the 41 failures measured in-field: the failures have been identified according to geologic unit.

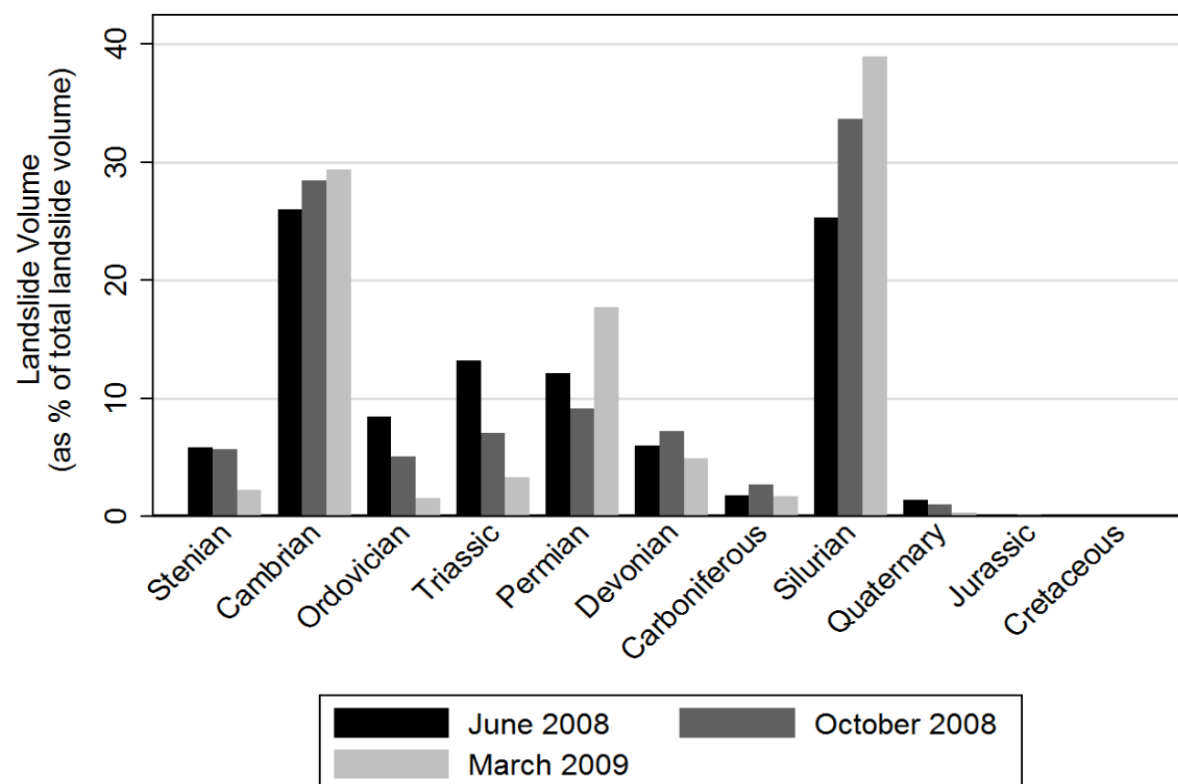


Figure 4.8: The distribution of landslide volume across the 11 geological units in the study area: landslide volume (m^3) in each geological unit is expressed as a percentage of total landslide volume. The three bars for each unit represent the three time periods: June 2008 (12/05/2008 – 04/06/2008); October 2008 (04/06/2008 – 13/10/2008); March 2009 (13/10/2008 – 24/03/2009).

5. Sediment aggradation: storage within the catchment

Using volume-area scaling relationships, the previous chapter illustrated how the volume of sediment displaced by landsliding can be determined using information gained from satellite imagery processing. Calculating the amount of displaced sediment provides a quantitative measure that can be used to assess the potential wider impact of landslides. However, in order for this information to be meaningful it is imperative to establish what happens to this sediment once it leaves the hillslope and its subsequent contribution to the broader orogen sediment budget (Korup et al., 2009). Three stages are possible, although the time spent by landslide sediment in each stage will vary considerably across the area and with the size of catchment (Figure 5.1):

- i. The sediment remains temporarily stored on the hillslope with the potential for remobilisation;
- ii. The sediment is transported off the hillslope (either through hillslope or channel processes), however remains temporarily trapped within the catchment, perhaps as temporary storage on the valley floor;
- iii. The sediment reaches the main channel network and is transported downstream, out of the catchment it originated in.

Over sufficiently long time scales it is expected that the majority of sediment (perhaps excluding the very coarsest material) will eventually reach the third of these stages and be discharged from the catchment (Hovius et al., 2000).

Quantifying the movement of sediment through a catchment, i.e. the amount of material at each stage and the fluxes between stages, is needed in order to understand the variability in landslide sediment production and delivery (Korup et al., 2009). In particular, quantifying the amount of sediment storage (i and ii) provides a fundamental link between sediment dynamics and landscape evolution (Otto et al., 2008). For both stages of temporary sediment storage, i.e. where sediment is stored on the hillslope (i) and in areas of the valley floor (ii), however, this may be very difficult, as many areas are inaccessible and information from satellite imagery alone does not allow the depth of material to be constrained sufficiently. Therefore, additional resources and new techniques are required.

This chapter explores an innovative technique utilising oblique ground-based photographs in order to evaluate spatial and temporal changes in the depth of sediment which has aggraded on the valley floor and remains temporarily trapped within the catchment (ii). This allows calculations of sediment volume at this stage, which are a significant indication of the scale of the mismatches between landslide sediment supply and fluvial sediment transport

(Korup et al., 2009) and thus provide a unique insight into post-earthquake sediment storage in part of the area affected by the Wenchuan earthquake. Figure 5.1 shows the flow of sediment through a typical catchment to illustrate the specific aspects which are covered by this chapter.

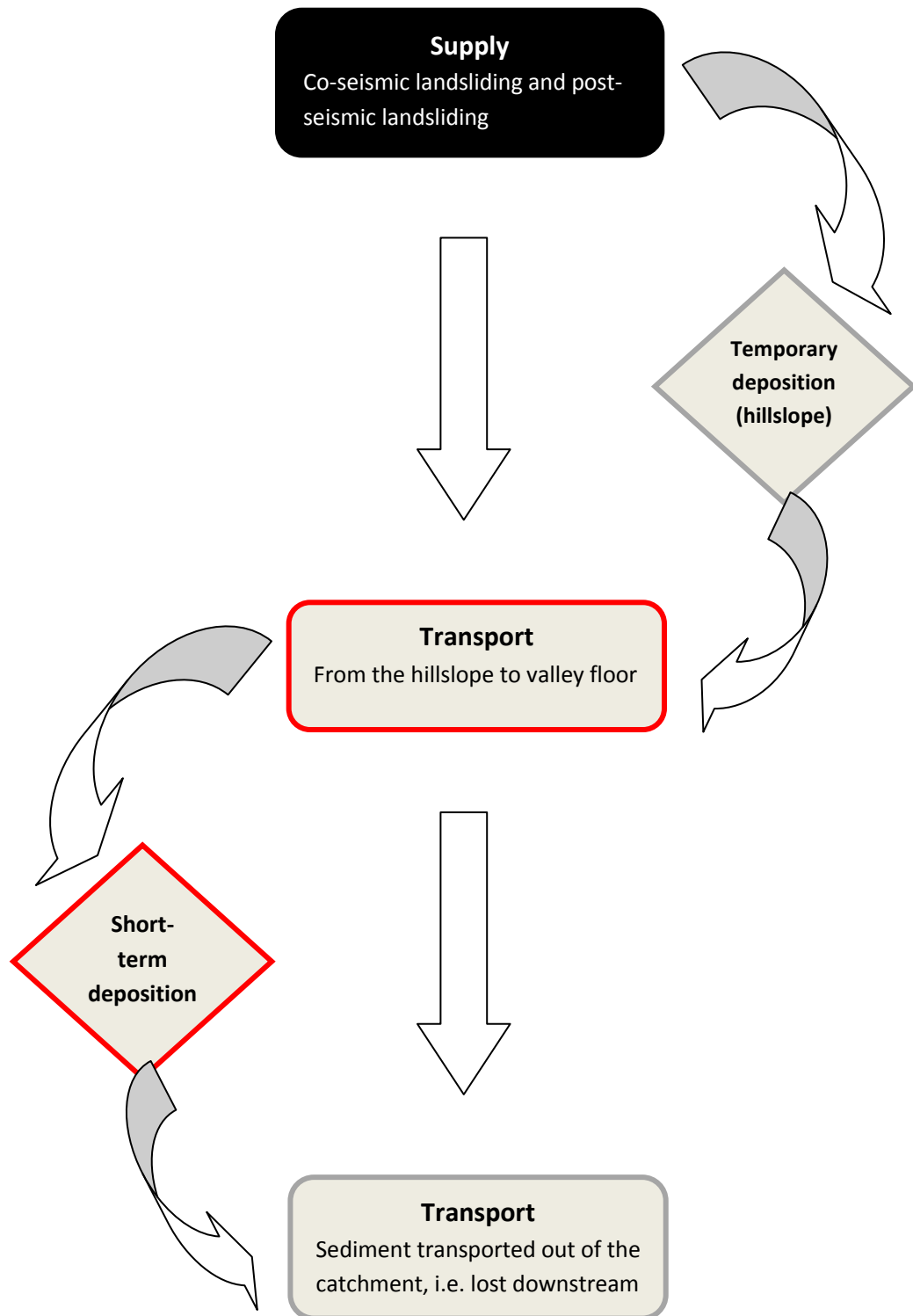


Figure 5.1: Flow diagram of sediment movement through a typical catchment. Highlighted areas (black) indicate what has already been addressed in previous chapters and areas outlined in red indicate the focuses of this chapter.

5.1. Methods

Developing the oblique photograph technique

Measurements of sediment depth are not attainable from satellite imagery and many areas of significant sediment aggradation in Sichuan are inaccessible, so that field measurements could not be relied upon as a method of constraining sediment depth. Consequently a method was required that allowed sediment depth to be evaluated remotely. The idea for adopting the use of oblique photographs was developed when viewing a collection of photographs of Beichuan town from different time periods (Figure 5.2), and from the proliferation of photographs of the post-event situation on the internet. These photos indicate that (1) a substantial amount of sediment aggradation had occurred post-earthquake; and (2) the changes in this over time were easily identified against buildings and other fixed structures in the photographs. Using these as benchmarks on the ground, it is possible to gain a crude estimate of the depth of aggraded sediment. Based on this idea, the following method was developed in order to constrain the depth of sediment deposits.

- i. Collect a range of photographs that cover the spatial extent of a catchment valley floor; in addition collect photographs of the same locations from different dates, covering a wide temporal range and ensuring both pre-event and post-event coverage of the area.
- ii. Identify buildings/structures as benchmarks in the photographs and take repeated measurements of sediment depth as multiples or fractions of floor to floor heights.
- iii. Optionally: convert relative measurements to absolute measurements using estimates or direct field measurements of floor to floor height.
- iv. Create an interpolated surface of sediment aggradation for each time period, taking depth at points across the catchment where measurements were taken and taking area as the planimetric extent of sediment aggradation visible from the satellite imagery.
- v. Calculate sediment volume from each of the interpolated surfaces.

Application to Beichuan

Beichuan town was identified as one of the 'worst-hit areas' following the 2008 Wenchuan earthquake (Huang and Li, 2009). Located in an area of very high co-seismic displacement (Shen et al., 2009), Beichuan experienced high intensity shaking and severe landsliding during and immediately following the earthquake (Huang and Li, 2009a, 2009b; Ouimet, 2009). Subsequently the summer monsoon rains that strike this region annually have caused further

landsliding and sediment flows into Beichuan Town. As a result, significant sediment aggradation has been seen in this area and due to its high media profile, a wide collection of photographs was available. The town was also accessible for field data collection, making it an ideal location in which to apply the oblique photograph technique.

Photographic analysis

Photographs were collected from a range of sources (Table 5.1) and covered the majority of the valley bottom in the Beichuan town in addition to other locations in the fault rupture zone. The temporal range of the photographs provided data from June 2008 to October 2009, allowing a full annual cycle of changes to be observed. From this collection of available photographs, buildings were selected as benchmarks based on their level of visibility in the photograph and also ensuring that there was an even spatial distribution of benchmarks as much as possible. Figure 5.3 displays the location of the 12 benchmarks.

Alongside each benchmark building, measurements were taken from the roof to the sediment and expressed as multiples of floor height. Using the pre-earthquake photograph to establish the original building height (in floors), the depth of sediment could then be determined. Several measurements were taken alongside each building and the average of these is presented in Table 5.1 (see columns 3 to 5).



Figure 5.2: Initial photograph collection of Beichuan town, illustrating the temporal changes in sediment aggradation.

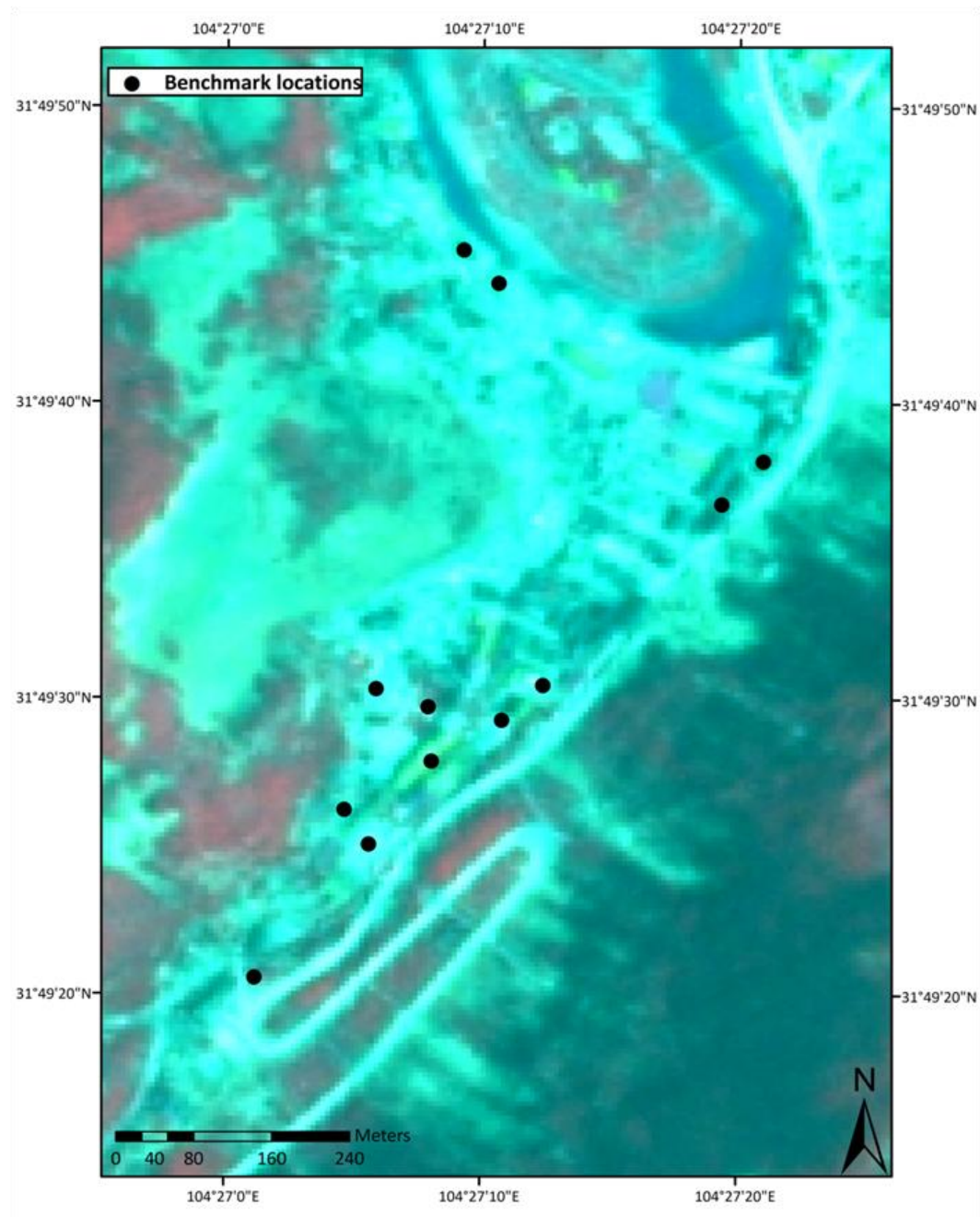


Figure 5.3: Location of the benchmarks used in photographic analysis of Beichuan town (background is the March 2009 SPOT 5 image).

Table 5.1: Sources, locations and dates of photographs collected for analysis

Source	Location	Dates
Internet sources: - Flickr (www.flickr.com) - Panoramio (www.panoramio.com)	Beichuan Leigu Yingxiu	June 2008 – October 2009
Lynn Highland (USGS)	Donghekou Yingxiu Beichuan	June – July 2008
Melanie Rodriguez (BBC)	Beichuan Town	November 2008
Dr. Alexander Densmore (Durham University)	Beichuan Town	August 2008
Prof. David Petley (Durham University)	Beichuan Leigu Chenjiaba Yingxiu Donghekou	March 2009
Harriet Tomlinson (Durham University)	Beichuan Town	August 2009

Field data collection

In order to establish absolute measures of sediment depth, fieldwork was used to measure the floor height of benchmark buildings in Beichuan town (Figure 5.4a). In places where the buildings were not directly accessible then a photograph containing a scale was taken and an accurate measure of floor height was obtained from this.

Many areas outside Beichuan town experienced large sediment flows and consequent sediment aggradation during the post-earthquake monsoon rainstorms, including Huangjiaba, a small settlement north-east of Beichuan. Two main sediment flows occurred in Huangjiaba after the earthquake: the first on 24/09/2008 and the second in July 2009 (information from local sources), however photographs of this area were not available and therefore the oblique photograph technique could not be applied. Instead, current measurements of sediment depth were made at accessible sites in the field and photographs were taken of areas not directly accessible (Figure 5.4b). It was also possible to establish an estimate of maximum sediment depth following the two sediment flows since the earthquake, based upon splash marks that were visible on building walls.



Figure 5.4: Photographs of fieldwork in Sichuan – **a**: measuring the floor height of benchmark buildings in Beichuan; **b** – assessing sediment depth (current and previous) in Huangjiaba.

Post-fieldwork analysis

Relative measurements of sediment depth in Beichuan were transformed to absolute measures based on the measurements of floor heights, and the results are shown in column 6 of Table 5.2. Enough data were available to examine sediment aggradation in Beichuan at the following time intervals: June 2008, October 2008, March 2009 and August 2009. For each time period, measures of sediment depth from the 12 benchmarks were interpolated using a spline function in ArcMap (Spatial Analyst tools) to the extent of the area identified from satellite imagery. The resulting surface models of sediment aggradation can be seen in Figure 5.6.

Adopting the same interpolation technique, estimates of sediment depth from Huangjiaba were also used to create surface models of sediment aggradation for the following time periods: October 2008, March 2009 and July 2009.

5.2. Technique evaluation**Precision**

In order to assess the precision and reliability of the oblique photograph technique, it was important to quantifiably constrain any error in making such measurements from photographs, i.e. to account for the bias judgement of the user. Therefore a similar technique was applied to a collection of photographs of buildings in Durham (UK) which could then be accurately measured on the ground to quantify any measurement error. The photographs were all taken from a central location in order that the distance from the camera to each building was known. Distances between the camera and buildings ranged from a few hundred meters to a kilometre; similarly in Beichuan the distances between the common photographic viewpoint and the buildings used as benchmarks ranged from 150 m to 1.42 km. On the ground in Durham, measurements of building height were taken using the height function of a handheld *LaserAce Hypsometer* laser ranging device (Geosolution, 2006).

Results show a range of error in the height estimations from photographs, compared to ground measurements, from 0.01% - 15%. These errors are both under- and over-estimations and there appears no bias towards either: the average error (bias) is 6.49% and the standard deviation (precision) is 5.72% (Figure 5.5). Generally the magnitude of error increases with an increasing distance between the camera and measured building:

- iv. ≤ 300 m from the camera, all errors are $< 5\%$;

- v. ≤ 500 m from the camera, all errors are $< 10\%$;
- vi. The largest error was of a building located 630 m from the camera.

However the most precise measurement was of a building located 720 m from the camera, suggesting that additional factors other than distance, i.e. photograph quality, lighting, ease with which the benchmark features can be identified etc, have influenced the measurements made.

To ensure that the range of possible error is accounted for, a conservative uncertainty estimate of $\pm 15\%$ was assumed for the results that are presented in the following section (5.3).

Limitations

The oblique photograph technique is reliant on a wealth of available photographs from a wide spatial and temporal range. Consequently, this places certain limits and conditions on the general application and use of the technique:

- The area and the timescale over which aggradation measurements can be made are both limited by the availability and quality of the photographs, in addition to the reliability of the published date;
- A pre-event photograph is required in order to view the area with zero aggradation;
- Relative measurements can be determined from the photographs, however some groundwork or prior knowledge (i.e. of floor height) is required to gain absolute measurements. This works well in Sichuan, where the buildings are very uniform and therefore all have a similar floor height. However this may be more challenging in other locations;
- The frequency of available photographs determines the detail that is seen in temporal change as each photograph provides only a snapshot of sediment aggradation.

Specific to the Sichuan region, two primary limitations are acknowledged and have been accounted for in the following ways:

- i. Photographs of different areas were not always available for the same dates, i.e. a photograph of one location in October 2008, another location in November 2008 and another in December 2008. In order to gain a series of pictures of sediment aggradation across the entire area of Beichuan town, the results have been grouped into time periods corresponding to the availability of photographs and extreme rainfall events, which are regarded as a primary trigger of large sediment transport events;
- pre-September 2008: after the earthquake event and before the first heavy rains;

- September – October 2008: the time during and immediately following the heavy rains that began on 24th September 2008;
 - November 2008 – March 2009: no significant rainfall events recorded;
 - April – August 2009: prior to and during the annual summer monsoonal rain; on average 79 % of the annual rainfall falls from June to September (Xu and Dong, 2009). However, this ultimately reduces the temporal precision of the technique.
- ii. Photograph quality varies due to restricted access into Beichuan town: the majority of photographs were taken from a single viewpoint and thus photographs of benchmarks further from this point are of a lower resolution. The error calculated based on photographs of Durham (UK) should account for the potential error associated with this limitation.

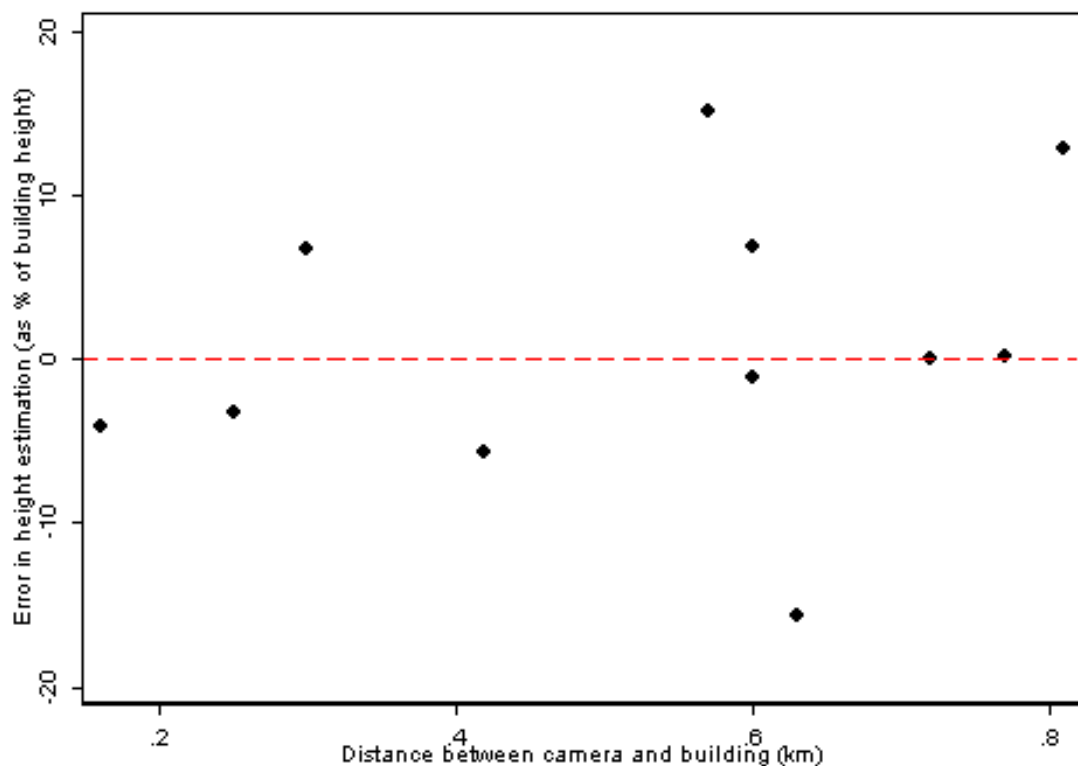
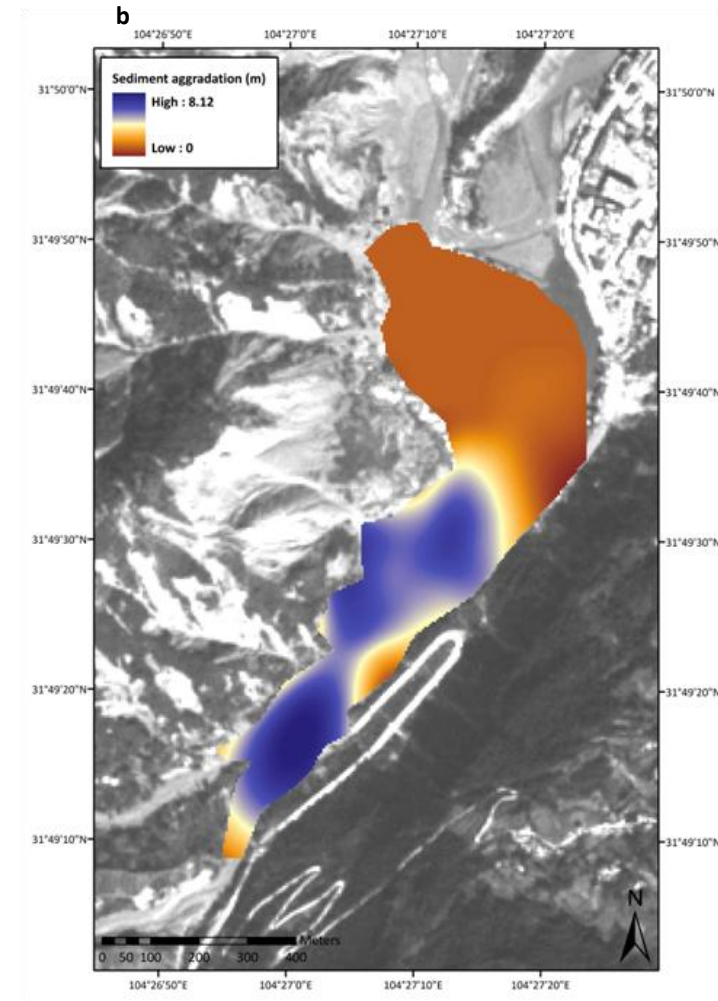
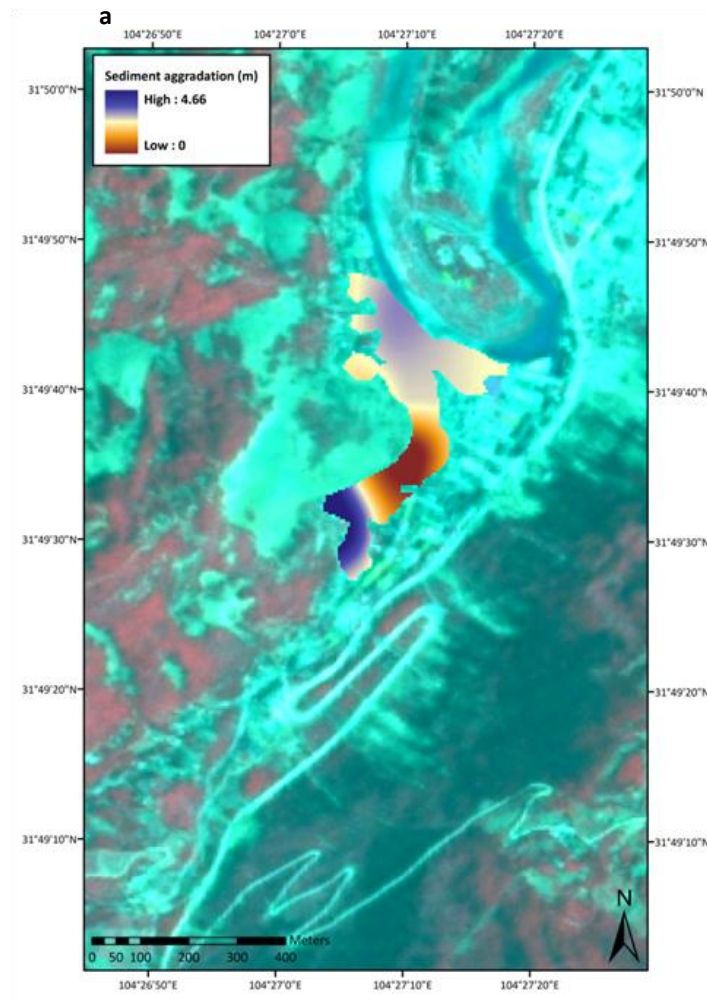


Figure 5.5: Plot displaying the error in building height estimations based on measurements taken in Durham, UK. Error is expressed as a percentage of the building height as plotted according to the distance between the camera and building. The red dashed line represents zero error.

Table 5.2: Measurements associated with the photographic analysis: columns 3 – 5 display data collected from the oblique photographs; column 6 displays fieldwork data; column 7 displays the resulting measures of sediment depth.

Building ID	Date of photo-graph	Roof to sediment (x fl)	Original building height (x fl)	Sediment depth (x fl)	Floor height (m)	Sediment depth (m)
1	26.06.08	5	5	0	2.4	0
	20.09.08	5	5	0	2.4	0
	26.11.08	1.74	5	3.26	2.4	7.82
	09.08.09	1.53	5	3.47	2.4	8.33
2	26.06.08	6	6	0	2.4	0
	20.09.08	6	6	0	2.4	0
	26.11.08	2.62	6	3.38	2.4	8.11
	09.08.09	2.57	6	3.43	2.4	8.23
3	26.06.08	5	5	0	2.4	0
	20.09.08	5	5	0	2.4	0
	26.11.08	1.89	5	3.11	2.4	7.46
	23.01.09	1.70	5	3.30	2.4	7.92
	20.03.09	1.33	5	3.67	2.4	8.81
4a	28.10.08	2.88	6	3.12	2.4	7.49
	26.11.08	3.07	6	2.93	2.4	7.03
	23.01.09	2.69	6	3.31	2.4	7.94
	20.03.09	2.48	6	3.52	2.4	8.45
4b	24.07.09	1.62	4	2.38	2.4	5.71
5	28.10.08	2.70	6	3.30	2.4	7.92
	26.11.08	2.45	6	3.55	2.4	8.52
	23.01.09	2.80	6	3.20	2.4	7.68
	20.03.09	2.49	6	3.51	2.4	8.42
	19.07.09	2.61	6	3.39	2.4	8.14
	24.07.09	2.58	6	3.42	2.4	8.21
6	26.06.08	6	6	0	2.4	0
	20.09.08	6	6	0	2.4	0
	28.10.08	3.20	6	2.80	2.4	6.72
	26.11.08	3.06	6	2.98	2.4	7.15
	23.01.09	3.10	6	2.90	2.4	6.96
	20.03.09	3.02	6	2.98	2.4	7.15
7	26.06.08	4.06	6	1.94	2.4	4.66
	28.10.08	2.64	6	3.36	2.4	8.06
	26.11.08	2.72	6	3.28	2.4	7.87
	20.03.09	2.60	6	3.40	2.4	8.16
	24.07.09	2.44	6	3.56	2.4	8.54
8	31.08.08	1.21	2	0.79	2.4	1.90
	09.08.09	1.07	2	0.93	2.4	2.23
9	31.08.08	2.31	3	0.69	2.4	1.66
	09.08.09	2.15	3	0.85	2.4	2.04
10	24.07.09	4.36	7	2.64	2.4	6.34
	24.10.09	5.16	7	1.84	2.4	4.42
11	24.07.09	5.16	7	1.84	2.4	4.42
	24.10.09	5.09	7	1.91	2.4	4.58
12	03.12.08	4.5	7	2.50	2.4	6
	09.08.09	4.5	7	2.50	2.4	6



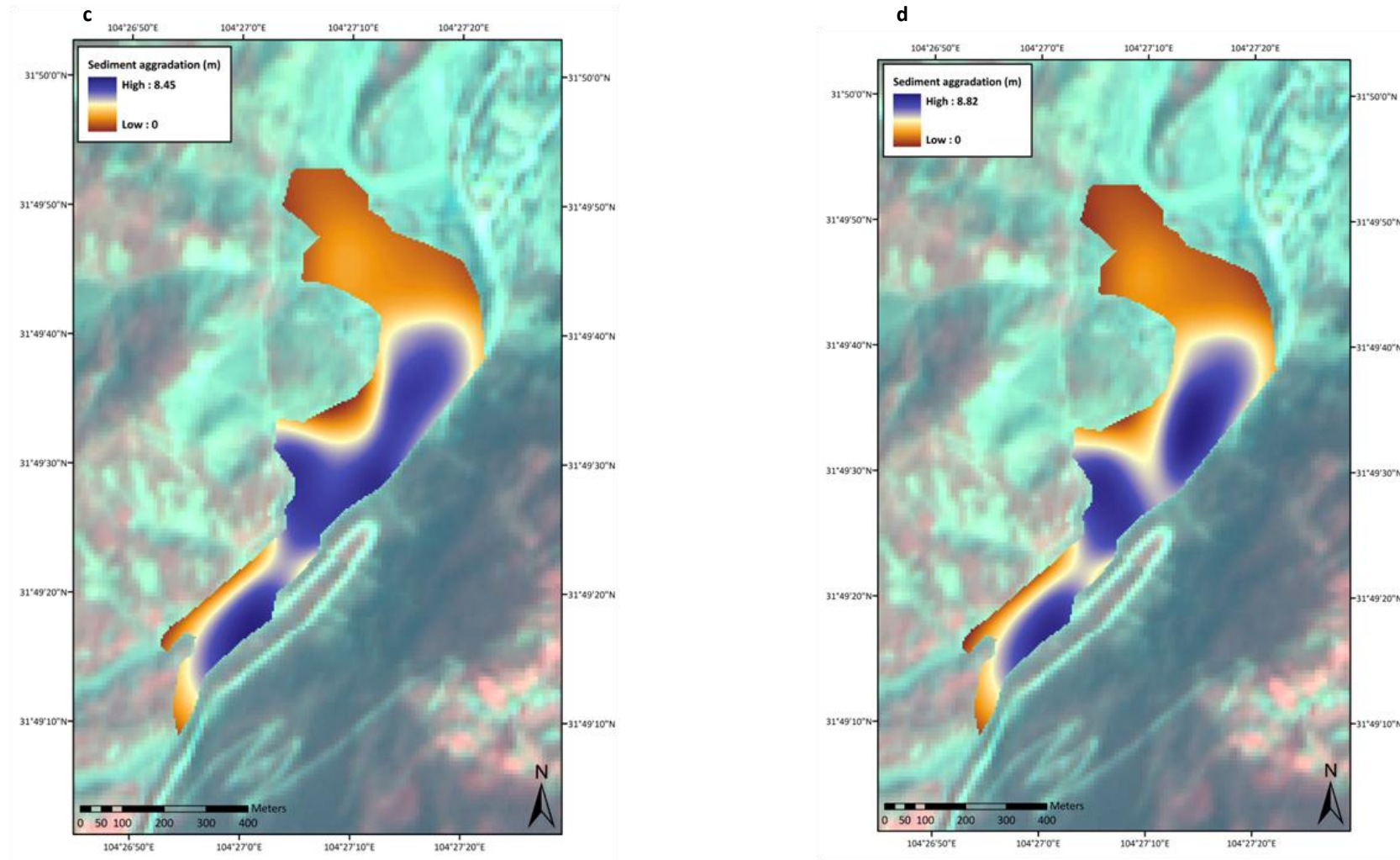


Figure 5.6: Surface models of sediment aggradation in Beichuan town: **a** – June 2008 (background: June 2008 SPOT 5 image); **b** – October 2008 (background: October 2008 SPOT 5 image); **c** – March 2009 (background: March 2009 SPOT 5 image); **d** – August 2009 (background: March 2009 SPOT 5 image).

5.3. Results

Volume calculations

Surface models of sediment aggradation in the Beichuan catchment are shown in Figure 5.6. The models display the temporal change in sediment aggradation between June 2008 and August 2009. Initially the most striking observation is the considerably smaller aerial extent of deposited sediments in June 2008 compared with all later models. The June 2008 surface model represents co-seismic sediment deposition, most probably as a result of landslides with a long runout; conversely all other surface models represent post-seismic sediment deposition, which was likely aided by heavy rainfall increasing transport capacity. The area covered by deposited sediments in March and August 2009 was smaller than in October 2008, especially towards the northern end of Beichuan town near the river channel; this suggests that a large amount of initial post-seismic deposition in this area was transported into the river network between October 2008 and March 2009. In addition to changes in the aerial extent of deposited sediments, the surface models display an increasing depth of sediments over time, indicating a continual transport of landslide material from the hillslopes to the valley bottom.

From the surface models the volume of aggraded sediments was obtained for both the Beichuan and Huangjiaba catchments. To allow a comparison between sediment storage and sediment supply (Figure 5.1), the volume of landslides within each catchment was calculated from each satellite image using the volume-area relationship developed in chapter 4 ($V = 0.1602 \cdot A^{1.388}$, equation 4.2). The results of both volume calculations are displayed in Table 5.3. In both catchments, landslide sediment volume (cumulative) and volume of aggraded sediment increased over time. Reassuringly, sediment deposit volume is always less than the landslide volume. For the Beichuan catchment, the amount by which sediment volumes increased was significantly reduced after October 2008, whereas in the Huangjiaba catchment sediment volumes increased by at least a factor of 2 between October 2008 and March 2009.

Results from the Beichuan catchment are displayed graphically in Figure 5.7, where the significant difference between landslide volume and volume of aggraded sediment can be clearly seen. This disparity is greater than an order of magnitude and represents the material that has remained stored on the hillslope or has been lost to the fluvial system downstream. Taking the pre-earthquake value of sediment volume as essentially negligible (Parker, 2010), the most significant increase in landslide sediment volume (supply) occurred co-seismically ($4.07 \cdot 10^7 \text{ m}^3$ – June 2008). After this, landslide sediment volume continued to increase in

smaller increments ($1.55 \times 10^7 \text{ m}^3$ – October 2008; $3.52 \times 10^7 \text{ m}^3$ – March 2009). Conversely, the most significant increase in aggraded sediment volume (deposition) occurred between June and October 2008, when the volume increased by approximately a factor of 5: from $1.52 \times 10^5 \text{ m}^3$ (June) to $9.93 \times 10^5 \text{ m}^3$ (Oct). The volume of sediment aggradation in Beichuan continued to increase after this, but by much smaller amounts (Table 5.3). These differences between the patterns of change in landslide sediment and aggraded sediment volume indicate a lag time of between 2 and 5 months between sediment supply and deposition in the Beichuan catchment.

Conceptual model of temporal changes

As shown by the results in Figure 5.7, the sediment volume of both supply (landslides) and deposition (aggradation) initially increase rapidly post-earthquake. Beyond a certain point (which differs for landslide sediment and aggraded sediment) the rate of increase begins to slow. Based upon previous examples of post-earthquake sediment dynamics (i.e. Chi-Chi, Taiwan: Chen and Petley, 2004) it is expected that the total volume of material will continue to grow before eventually approaching a maximum or limiting value. This trend is illustrated in the conceptual model shown in Figure 5.8, which can be described by the following equation:

$$V(t) = k(1 - \exp^{-t/t^*}) \quad (5.1)$$

Taking time = 0 as the earthquake event, the following stages can then be identified:

- i. *Initial rise in both sediment volumes:* The volume of landslide sediments increases very quickly as co-seismic landslides produce a high volume of material; the initial rise in aggraded sediment volume is much smaller and is most likely a representation of co-seismic landslides that run out directly onto the valley floor.
- ii. *Continued rise to 90% of peak volume:* Landslide sediment volume rises at a faster rate than the aggraded sediment volume due to the time taken for sediment to be transported from the hillslope to the valley bottom (Hovius and Stark, 2002). This is illustrated by the lag time between the points at which each sediment volume reach the 90 % value. During this time, various processes will act to rework the landslide sediments on the hillslope and transport them away (Keefer, 1994). Due to spatial variation in the location of landslides and associated sediments, these processes and thus the subsequent transport of material will also vary (Bull, 2009). Consequently, the lag time seen in this conceptual model represents an average lag time between supply and deposition, which is likely to vary throughout the catchment. This point is well illustrated in the work of Imazumi and Sidle (2007) who described differences in sediment transport based on the location of landslides with respect to the channel network. They also suggested that over shorter timescales (most relevant to this work)

sediment supply is the most dominant influence upon yield, reinforcing the idea of a lag time as sediment supply impacts upon deposition.

- iii. *Approaching a plateau:* Equation 5.1, which describes this graph suggests that the sediment volume approaches a maximum value (v) = k as time (t) approaches t/t^* ; as shown by the graph, both curves begin to plateau as they approach this value, however because of the exponential trend the sediment volume will never reach a value of k .

Table 5.3: A comparison of landslide sediment volume (m^3) and aggraded sediment volume (m^3) over time for the Beichuan and Huangjiaba catchments: the landslide volume displayed represents the incremental change between each satellite image, i.e. new landslides; the bracketed number represents the cumulative landslide volume since the earthquake.

Time period	Beichuan			Huangjiaba		
	Watershed landslide (LS) volume (m^3)	Aggraded sediment (AG) volume (m^3)	AG volume as a % of LS volume	Watershed landslide volume (m^3)	Aggraded sediment volume (m^3)	AG volume as a % of LS volume
Pre-September '08	4.07×10^7	1.52×10^5	0.373 %	1.37×10^7	n/a	n/a
September – October '08	1.55×10^7 (5.62×10^7)	9.93×10^5	6.41 % (1.77 %)	4.62×10^7 (5.99×10^7)	7.40×10^4	0.160 % (0.124 %)
November '08 – March '09	3.52×10^7 (9.14×10^7)	1.35×10^6	0.384 % (0.148 %)	2.00×10^8 (2.60×10^8)	1.48×10^5	0.074 % (0.057 %)
April – August '09	<i>Unknown</i>	1.36×10^6	<i>Unknown</i>	<i>Unknown</i>	1.88×10^5	<i>Unknown</i>

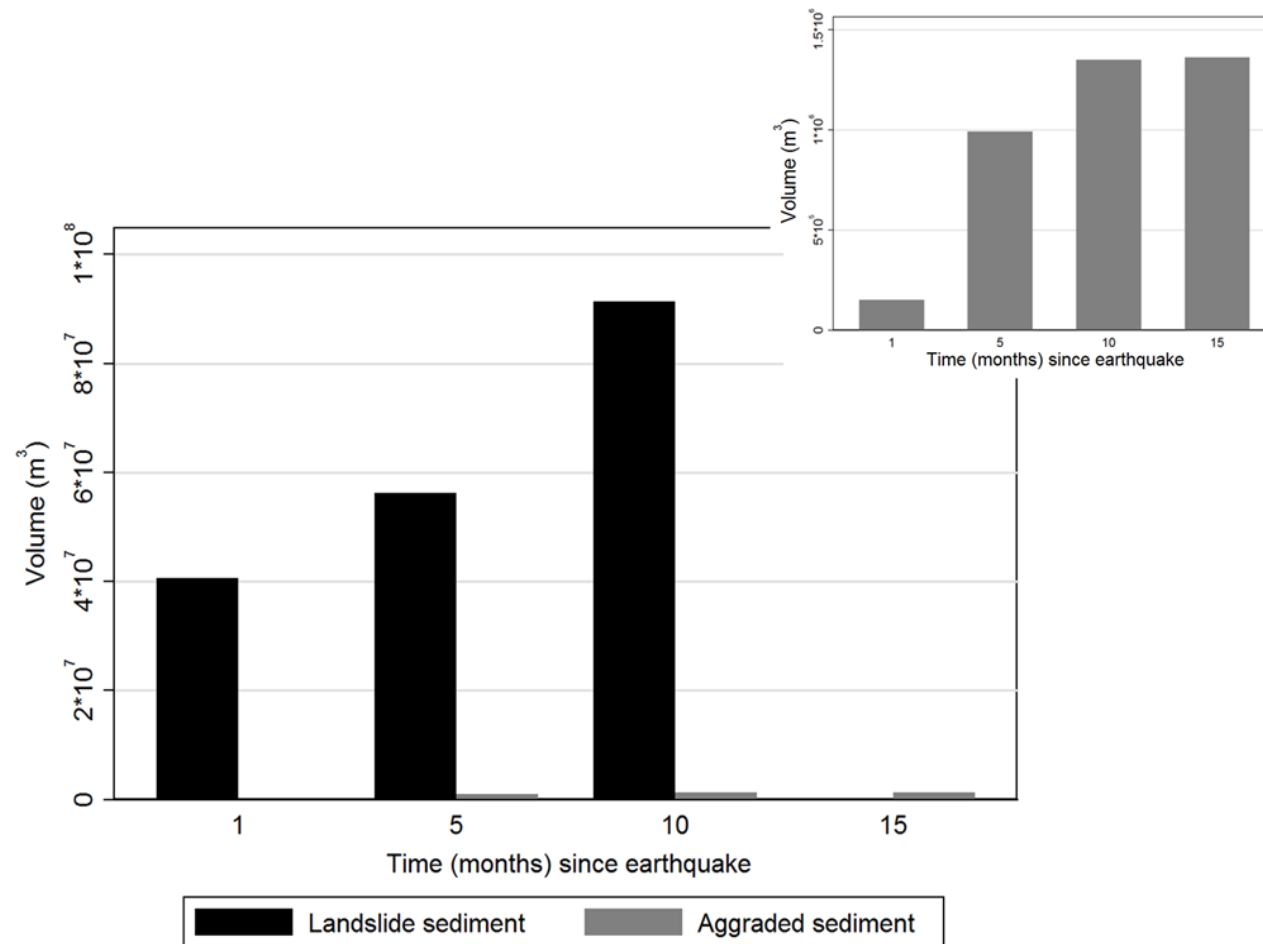


Figure 5.7: Temporal changes in landslide sediment (cumulative) and aggraded sediment volume for the Beichuan catchment based on data in Table 5.2. (*Inserted graph displays the aggraded sediment volume only.*)

Application to Beichuan

As the most comprehensive dataset regarding sediment aggradation is from the Beichuan catchment, this has been used to examine temporal changes in landslide sediment and aggraded sediment volumes by fitting the data to the negative exponential growth model (Figure 5.8). Owing to the difference (> an order of magnitude) between aggradation volume and landslide volume, the results have been presented on two separate graphs in Figure 5.9 (a and b).

Landslide sediment volume: Based on what can be seen in the range of oblique photographs used in this work, the low volume of landslide generated sediments in October 2008 is likely to be an underestimation; ground-based photographs taken in late September and early October 2008 display a notable increase in landslide density compared with photographs from June – August 2008; in addition, previous studies have highlighted the significance of the monsoon rains that began on 24th September 2008 for inducing numerous additional slope failures (Lin and Tang, 2009). It is likely that this error can be attributed to the different satellite imagery (panchromatic) used to map the landslides from October 2008 and thus the different mapping algorithm that was employed in comparison to the mapping of multispectral satellite imagery for June 2008 and March 2009. To allow for these inconsistencies, three additional curves have been added to the landslide sediment volume graph (Figure 5.9a): one based on the October data increased by 30 %, another based on the October data increased by 50 % and the final curve based on the June and March data only.

Fitting the original dataset and the three additional versions with a negative exponential decay based on the conceptual model (Figure 5.8), the following equations are obtained:

$$- V = 8.43 \cdot 10^7 (1 - \exp^{-0.3802t}) \text{ (original data)} \quad (5.2)$$

$$- V = 8.60 \cdot 10^7 (1 - \exp^{-0.5617t}) \text{ (October data +30\%)} \quad (5.3)$$

$$- V = 9.01 \cdot 10^7 (1 - \exp^{-0.5839t}) \text{ (October data + 50\%)} \quad (5.4)$$

$$- V = 9.17 \cdot 10^7 (1 - \exp^{-0.5871t}) \text{ (June and March data only)} \quad (5.5)$$

This suggests that the potential values for the maximum volume of landslide sediments in the Beichuan catchment range from $8.43 \cdot 10^7 \text{ m}^3$ – $9.17 \cdot 10^7 \text{ m}^3$. It is probable that this value is towards the higher end of the range, based on the results of equation 5.5 and the associated curve of June and March data: whilst this may present a false impression of how quickly landslide sediment volume rises between June and October 2008, the values of landslide

sediment volume in June 2008 and March 2009 are both reliably based upon the same established landslide mapping technique (see Parker, 2010).

Aggraded sediment volume: Fitting the sediment aggradation data for the Beichuan catchment with a negative exponential decay based on the conceptual model (Figure 5.8) produces the curve (solid line) shown in Figure 5.9b with the following equation:

$$V = 1.48 \cdot 10^6 (1 - \exp^{-0.2073t}) \quad (5.6)$$

This suggests that the maximum volume of aggraded sediments in the Beichuan catchment will reach $1.48 \cdot 10^6 \text{ m}^3$. However allowing for the +/- 15 % error margins, as established from the technique evaluation, this maximum volume could range from c. $1.2 \cdot 10^6 - 1.6 \cdot 10^6 \text{ m}^3$.

As suggested by the conceptual model (Figure 5.8), landslide sediment volume rises at a faster rate than the aggraded sediment volume. This is demonstrated by the lag time between the curves, identified by the points at which each sediment volume reaches its 90 % value: based on the original landslide data (equation 5.2) the lag time is 3.9 months, however this could be as long as 5.6 months based on the upper range of landslide data (equation 5.5). The lag time is based upon data that encompasses the onward transport and deposition of both co-seismic and post-seismic landslide material, however it is likely that the lag time will vary between co-seismic and post-seismic material. The onward transport of co-seismic landslide material is more difficult than post-seismic material (Hovius and Stark, 2002) thus suggesting a longer lag time between the supply and deposition (landslide and aggradation) of co-seismic material. Hovius and Stark (2002) suggest that the coarseness of the material; the spatial distribution of failures (co-seismic nearer ridge crests and post-seismic nearer hillslope toes); and the enhanced river transport capacity at times of post-seismic landslide activity, all contribute to easier and faster transport of post-seismic landslide material. This idea has been well illustrated by the recent storms and widespread post-seismic landsliding in Sichuan, China (BBC, 2010): many failures occurred at low points on the hillslopes and the heavy rains meant that subsequent transport of material into the valley areas below was almost instantaneous (BBC, 2010). In addition to newly generated landslide material, the heavy rains also remobilised co-seismic landslide sediments, which were temporarily stored on the hillslope – this further demonstrates the potential variation in the supply-deposition lag time.

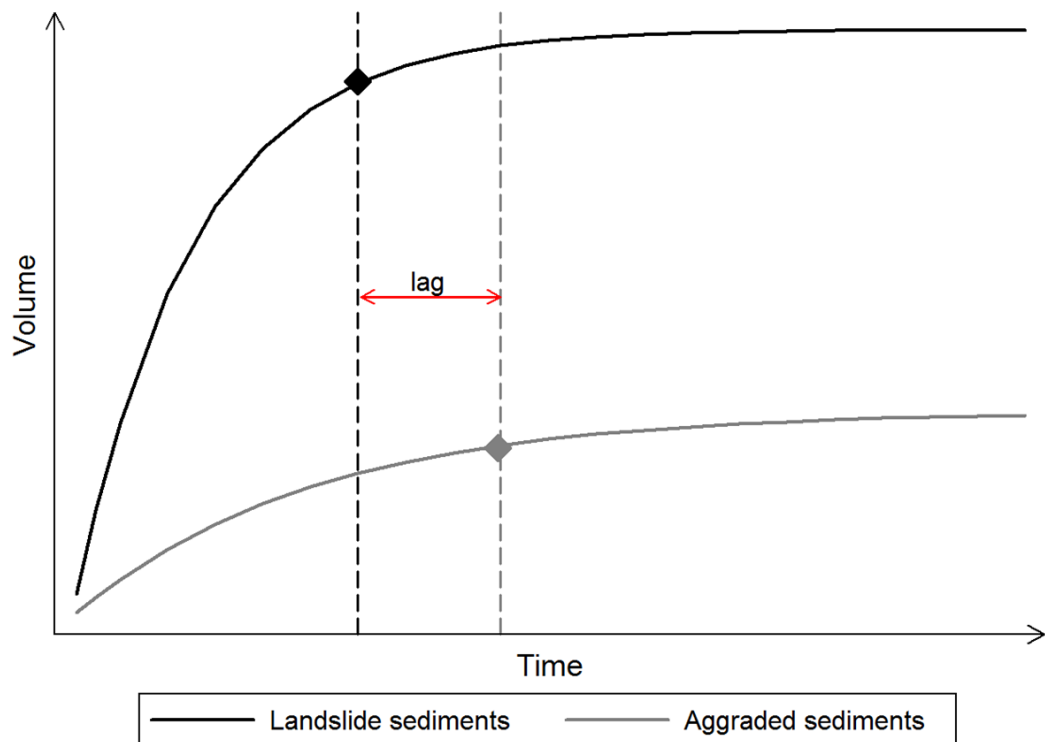


Figure 5.8: Conceptual model of the temporal changes in landslide sediment and aggraded sediment volumes post-earthquake for a typical catchment. The diamonds represent the point at which each volume is at 90% of its peak value: the lag time between these points is shown by the red arrow.

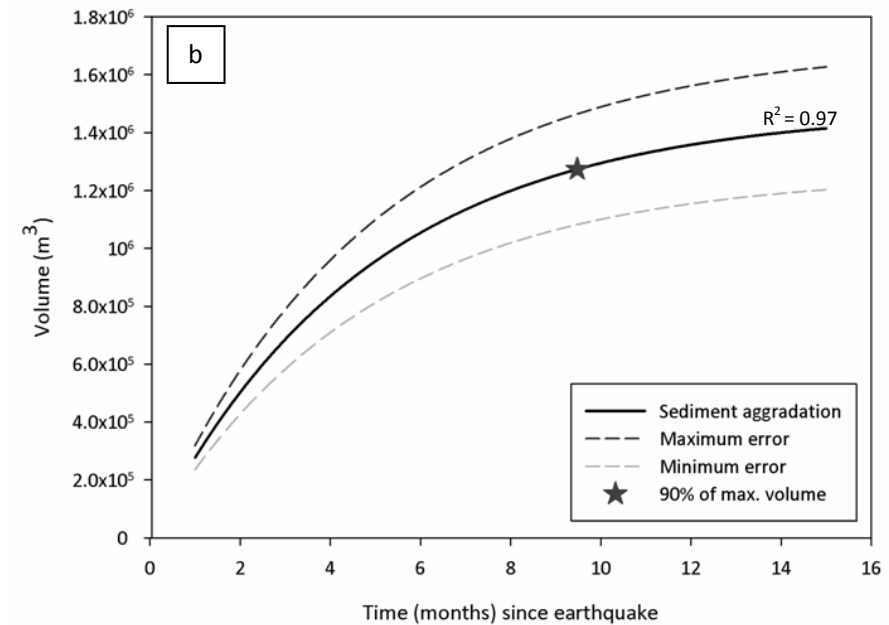
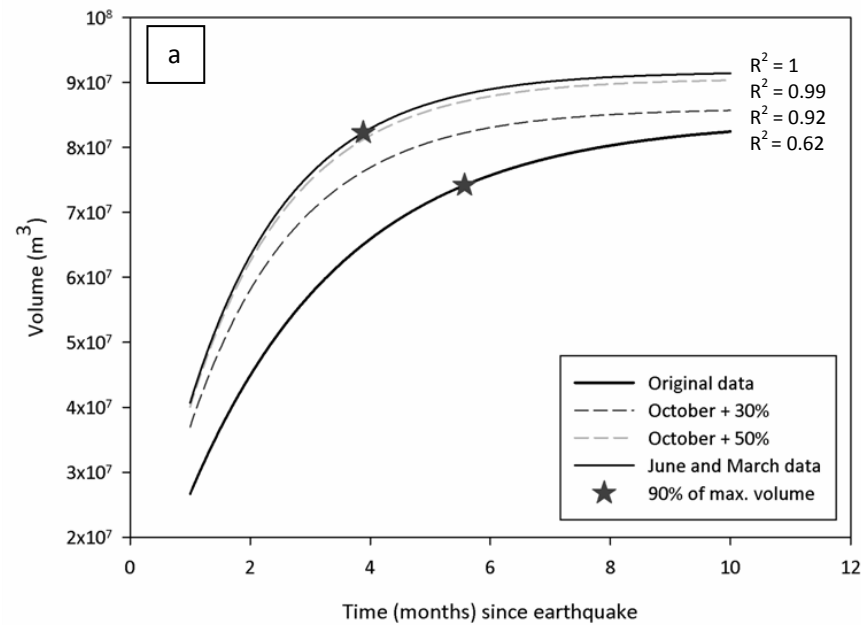


Figure 5.9: Cumulative landslide sediment volume (a) and aggrated sediment volume (b) data for the Beichuan catchment, fitted with a negative exponential decay:

a – landslide sediment volume curves based on original data ($V = 8.43 \cdot 10^7 (1 - \exp^{-0.3802t})$); original June and March data with increased October volumes (Oct +30%: $V = 8.60 \cdot 10^7 (1 - \exp^{-0.5617t})$; Oct +50%: $V = 9.01 \cdot 10^7 (1 - \exp^{-0.5839t})$); and June and March data only ($V = 9.17 \cdot 10^7 (1 - \exp^{-0.5871t})$).

b – aggradation volume curve ($V = 1.48 \cdot 10^6 (1 - \exp^{-0.2073t})$) with +/- 15% error margins shown by the dashed curves.

6. Analysis and Discussion

The results presented in the previous chapters illustrate the complex sediment dynamics that have occurred in the Beichuan area of Sichuan, China in the two years following the 2008 Wenchuan earthquake. In order to discuss these findings, the following chapter is broadly split into four sections:

- i. The first section addresses the sediment source, by examining the relationship between landscape characteristics and the occurrence of landslides;
- ii. The second section considers the movement of sediment through discussion of the impact of the volume of material that has been displaced by landsliding in the Beichuan area.
- iii. The third section addresses the wider literature regarding sediment dynamics of the Wenchuan earthquake and discusses the findings of this study within that context.
- iv. The final section evaluates the resources and techniques used to obtain these findings.

6.1. Landscape characteristics and landslide occurrence

6.1.1. Comparing Beichuan to the wider earthquake affected region

Since the Wenchuan earthquake in May 2008, numerous studies have been conducted to investigate the earthquake-induced landsliding. Some of these investigations have been field-based (Zifa, 2008), others relying on imagery for a remote study (Sato and Harp, 2009), and many have combined both methods of research (Yin *et al.*, 2009) as has been done in this work. A large proportion of post-earthquake investigations following Wenchuan are larger, regional based studies, which investigate the wider earthquake-affected area (i.e. Parker, 2010). Therefore the results of this study, which are focused on the Beichuan area, have provided an opportunity to compare Beichuan as one of the worst affected areas (Wang *et al.*, 2009) with the wider earthquake-affected region.

The spatial distribution of landslides with respect to seismological controls has been evaluated for the Beichuan area using the relationship between landslide occurrence and distance from the fault rupture. Larger studies of the earthquake-affected area observe that the distribution of landslides follows the fault rupture, with landslides mostly located within 10 km wide zone around the fault (Parker, 2010; Sato and Harp, 2009). This observation also holds true for the Beichuan area.

In examining this relationship, most of the larger studies note a marked hanging wall effect, which is common to such thrust events due to significantly higher levels of peak ground acceleration (PGA) in the hanging wall of the fault compared to the footwall (i.e. Parker, 2010; Sato and Harp, 2009; Huang and Li, 2009b). Parker (2010) also suggest that in addition to the seismological control of PGA, the hanging wall effect upon the Wenchuan earthquake landslide distribution could be attributed to the nature of the topography on either side of the fault: overall the topography of the hanging wall is higher and steeper than the shallower hillslopes of the footwall. Whilst the hanging wall effect can be seen in the Beichuan area, it is not as striking as is seen in other studies. Considering the reasons attributed to the hanging wall effect, the following explanations seem reasonable to explain the increased landsliding observed in the footwall of the Beichuan area compared to the overall trend. Firstly, PGA was sufficiently high in the Beichuan area that the footwall was likely to be more affected by seismic shaking compared to the footwall for the entire earthquake-affected area, thus triggering further landsliding. Secondly, the study area used in this work sits within a 20 km wide zone of the fault rupture; within this area the topography of a large proportion of the footwall is equally as steep as the hanging wall, thus providing the topographical setting in the

footwall of the Beichuan area, which Parker (2010) suggests as an influence upon the high density landsliding in the hanging wall.

In addition to the marked hanging wall effect, Yin *et al.* (2010) note differences in the relationship between landslide occurrence and distance to the fault rupture between the hanging wall and the footwall: graphs displaying this relationship show a linear trend in the hanging wall but an exponential trend in the footwall (Yin *et al.*, 2010: 454). Comparatively, this work has observed similar trends in both the hanging wall and the footwall, both displaying an exponential decay in landslide density with distance from the fault rupture (see Chapter 3: Figure 3.20).

The topographical controls on landslide distribution in the Beichuan area are assessed by examining the relationship that landslide occurrence has with and slope angle; elevation; and aspect. In general, landslides preferentially occur on steeper and higher slopes as they are more susceptible to fail (Dai *et al.*, 2010). Additionally, certain aspects are also more prone to landsliding due to the direction of peak ground accelerations from the fault rupture; slopes with a south-east orientation, i.e. an aspect facing the fault rupture and thus facing oncoming seismic waves, are more likely to fail (Chang *et al.*, 2007). This has been seen both in results from this work in the Beichuan area (see Chapter 3: Figure 3.30) and in larger studies, i.e. Dai *et al.* 2010.

In agreement with many regional studies following the Wenchuan earthquake (i.e. Dai *et al.*, 2010; Parker, 2010; Yin *et al.*, 2009), co-seismic landslides in the Beichuan area oversample on steeper slopes. Whilst this is also true for post-seismic landslides, the distinction between oversampling of steeper slopes and undersampling of shallower slopes is less notable. In addition, Sato and Harp (2009) observe that co-seismic landslide density in Sichuan increases with slope angle to a peak at around 35°; beyond this point landslide density decreases (see Figure 6.1). This trend has also been seen in studies of earthquake-induced landsliding following the 1994 Northridge earthquake, California (Parise and Jibson, 2000) and can be seen in the results from the Beichuan area (see Chapter 3: Figure 3.22). The trend is more notable in the results from June 2008 compared to March 2009 suggesting that the relationship with slope angle as recognised by Sato and Harp (2009) is related primarily to the seismic influence upon slope failure; a slight difference in this trend is seen in relation to the influence of post-seismic triggers of slope failure. As heavy rainfall has been recognised as a primary trigger of post-seismic landsliding, this provides support for the notion that heavy rainfall and storm activity is very significant in determining the distribution of slope failures (Owen *et al.*, 2008).

Landslide density around the Beichuan area also displays a significant increase on higher slopes as expected (Dai *et al.*, 2010). However, in contrast to regional studies (Parker, 2010; Huang and Li, 2009a; 2009b) landslides in the Beichuan area do not display above average landslide densities on higher slopes; whilst landslides were limited to areas of higher elevation, they did not occur disproportionately in those areas. The difference in sample size between this work and other studies is most likely to account for the difference in results.

The relationship between landslide distribution and geologic unit has been used to assess the influence of geological controls upon landslide occurrence. Each type of material will respond differently to triggers of slope failure, both seismic activity and rainfall (Yamagishi *et al.*, 2008) and thus these results significantly indicate the susceptibility of each geologic unit to slope failure. In addition, it is imperative to recognise that not only the type of material but also the location of the geologic unit with respect to seismic impact will particularly influence its susceptibility to failure.

Geological controls on landsliding in the Beichuan area reflect the results of regional studies; Yin *et al.* (2010) investigate the relationship between landslides and geologic unit and find that the Lower Cambrian unit is the most susceptible to seismically triggered landslides, whereas both the Quaternary and Jurassic units appear less susceptible to landsliding than all other geologic units in the study area. The results of this study support this observation as higher than average landslide densities have been observed in the Cambrian geologic unit amongst others, whilst lower than average landslide densities are observed in the Quaternary and Jurassic units. Similar distributions have been seen in studies from Dai *et al.* (2010) and Qi *et al.* (2010) amongst others. Crucially, this pattern also reflects the distance from the fault rupture: those geologic units that appear most susceptible to landsliding are those located closer to the fault rupture. This raises the question as to which is more important: the geologic or seismic influence upon landslide occurrence? Some studies conclude that geology does not play an important role (i.e. Yin *et al.*, 2010); however, investigations into seismically influenced landsliding following the Wenchuan earthquake cannot separate the two controlling factors due to the spatial distribution of geologic units. Therefore whilst one factor may be more or less influential than the other, it is clear that in combination they exert a strong influence over landslide occurrence (Wang *et al.*, 2009b).

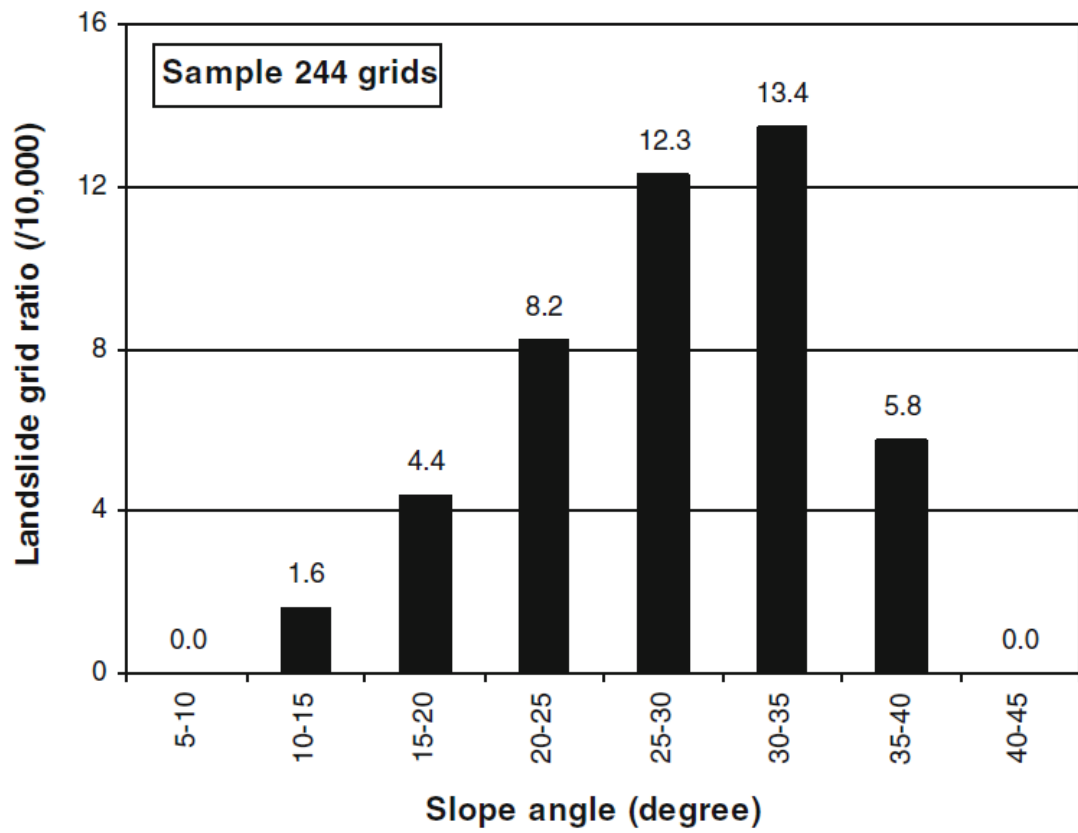


Figure 6.1: Landslide density with respect to slope classes for the co-seismic landslides triggered within 3 days of the Wenchuan earthquake (taken from: Sato and Harp, 2009).

6.1.2. Temporal changes in landsliding: June 2008 – March 2009

Sequential satellite imagery and a collection of oblique photographs spanning a wide temporal range post-earthquake have provided a crucial insight into the temporal changes in landslide occurrence and sediment movement, which few other Wenchuan studies to-date have investigated. The following paragraphs discuss the main changes noticed in the post-seismic evolution of landslides in the Beichuan area, using examples from recent post-seismic landslide investigations following the 2005 Kashmir earthquake, Pakistan and the 1999 Chi-Chi earthquake in Taiwan.

The overall distribution of post-seismic landslides indicates a shift to a higher proportion of failures in the hanging wall of the fault rupture compared with co-seismic landslides, which are distributed more evenly across each side of the fault. Whilst the intensity of seismic shaking was high on both sides of the fault in the Beichuan area, it is recorded as higher in the hanging wall (Huang and Li, 2009b) and therefore a larger proportion of slopes are likely to have been weakened during the earthquake. This illustrates the trend of post-seismic landslides occurring in locations that were weakened by the earthquake; this has been recognised in investigations of post-seismic activity in Kashmir, Pakistan (i.e. Saba *et al.*, 2010) and in Taiwan, following the 1999 Chi-Chi earthquake (Dadson *et al.*, 2004).

The distribution pattern of post-seismic failures with respect to slope angle also highlights the influence of pre-weakened slopes as post-seismic failures follow a similar pattern to co-seismic failures (see Chapter 3: Figure 3.26). However, post-seismic landslides are distributed over a wider range of slopes, indicating the failure of shallower slopes and therefore also highlighting the importance of post-seismic triggers in influencing landslide location, as demonstrated by the influence of heavy rainfall on post-seismic landslide occurrence in Taiwan following the 1999 Chi-Chi earthquake and subsequent typhoons (Dadson *et al.*, 2004). This distribution pattern is reinforced in Sichuan by a more uniform distribution of post-seismic landslides across the hillslope, as shown by results of the relationship between post-seismic landsliding and local elevation (see Chapter 3: Figure 3.25), which indicate the presence of landslides on lower slopes that hadn't failed co-seismically.

Whilst other topographical controls including slope angle and local elevation indicate that post-seismic landsliding is more widespread than co-seismic, results of the changes in aspect of landslides over time would suggest otherwise. The distribution of landslides becomes more focused on a smaller range of aspect values over the temporal range of the study (i.e. between June 2008 and March 2009), with a greater proportion of failures located on south-east facing slopes, i.e. those most seismically impacted. Although this differs from the more

widespread distribution of post-seismic landslides, it further supports the idea that post-seismic landslides occur on seismically pre-weakened hillslopes.

Overall there was no major change in the pattern of landsliding with respect to geologic unit over time; generally landslide density increased in most units, in line with the widespread distribution of post-seismic failures, with the exception of Jurassic and Triassic units where a decrease in landslide density was seen between June 2008 and March 2009. This distribution pattern can be partly attributed to the location of both Jurassic and Triassic units in the footwall of the fault rupture, where post-seismic landsliding was comparatively low. In addition to the influence of location and pre-weakened slopes, Yamagishi *et al.* (2008) found that few rainfall-induced landslides occur in sandstone materials, which is a major lithological component of both the Jurassic and Triassic units in this region; therefore providing further explanation for the indication that post-seismic landsliding did not occur here.

6.1.3. The influence of landslide location

Landsliding is both spatially and temporally clustered due to the nature of its triggers (Peart *et al.*, 2005). Seismic triggering of landslides in the 2008 Wenchuan earthquake occurred within a very short, intense time frame and was unevenly spatially distributed; similarly, high intensity rainstorms that triggered post-seismic landsliding also occurred over a relatively short time period (i.e. 2-3 days), acting on slopes particularly susceptible to failure. Subsequently there is considerable spatial (and temporal) variability in rates of sediment transfer, which is a recognised characteristic of mountain environments (Warburton, 2006). Due to both the spatial and temporal clustering of landslides and the discontinuity in the transport of material from the hillslope to the valley floor, the volume of landslide material is often not reflected in downstream sediment loads (Hovius *et al.*, 2000). The following section will briefly discuss the influence of landslide location upon the volume of material generated by landslides and upon the delivery and subsequent storage of this material.

Volume-area relationship

The relationship between volume and area of the landslides measured in-field exhibited a very similar trend in both the hanging wall and the footwall of the fault rupture; additionally there was little variation in the relationship between landslides in different geologic units. Therefore the scaling of landslide depth (and thus the volume of material) with respect to the landslide area did not appear to be influenced by landslide location. However the total volume of landslide material generated did vary with landslide location based on the different geologic

units. In particular, the Cambrian and Silurian units contributed to more than 50 % of the total volume of material generated in this study area. This can be partly attributed to the large aerial extent of the Silurian unit and the higher density of landslides in both Silurian and Cambrian units; however the larger size of landslides in the Cambrian and Silurian rocks is also responsible for the large proportion of the material generated in these two geologic units. Therefore catchments located over Cambrian and Silurian rocks have received a higher volume of landslide material with the potential for onward delivery and storage: in this way, landslide location has influenced the volume of generated material.

Additionally, this is likely to influence the longer term evolution of the area: higher rates of landsliding and mobilised sediment volume mean that erosion rates will be greater in the Cambrian and Silurian units. As a result of their location in the hanging wall of the fault rupture, increased erosion rates in Cambrian and Silurian units are partly compensated for by the uplift during the earthquake, which was greater than in the footwall (Xu *et al.*, 2009). However the difference in landslide sediment volume between geologic units suggests that erosion rates are non-uniform across the Beichuan area.

Sediment delivery and storage

Generally, high rates of sediment production in mountain environments, translate into elevated rates of sediment transfer and deposition (Warburton, 2006). However it is important to recognise that sediment delivery in tectonically active environments depends on the nature of the geomorphological processes operating (Warburton, 2006).

The type of failure and hence the landslide material are both key factors in determining the significant effects of the landslide (Keefer, 1999). Geological characteristics of the slope control the type and the nature of the landslide, which in turn establishes the material composition, i.e. how it breaks up and subsequent grain size: such characteristics of the material will determine its potential for transport (Warburton, 2006). For example the average grain size (D_{50}) of a rockfall will be large and therefore difficult to transport, most likely resulting in a short runout; conversely the D_{50} of a debris flow is likely to be small to medium and the higher proportion of fluid in the mixture provides increased energy for erosion, resulting in a fast moving flow which is easily transported and therefore most likely to have a long runout into the channel network. During field studies in the Beichuan area a variety of failure types were observed and the associated variations in runout and onward transport were also seen. Variations appeared to occur with changes in rock type throughout the region: for example, failures in the Cambrian rocks of the hanging wall around Beichuan town were composed of fine to medium grains and had a long runout (Figure 6.2a); conversely failures in

the Permian and Carboniferous rocks of the footwall around Beichuan town were larger rock falls with a very large D_{50} and correspondingly short runouts (Figure 6.2b).

These observations from the Beichuan area are in agreement with observations from the wider earthquake affected region: In a preliminary investigation into some of the larger landslides triggered by the Wenchuan earthquake, Wang *et al.* (2009b) note that long-runout, mass movements occur predominantly in slate, mudstone and shale (typical lithologies of the Silurian, Triassic and Jurassic units); conversely large rockfalls were primarily found in dolomite (typically found in Devonian rocks).

In addition to the geological control on sediment delivery, Hovius *et al.* (2000) stress the importance of landslide location within the landscape in determining the rate of landslide sediment delivery into the channel network. The transport capacity of a river generally increases downstream and therefore the rate of landslide debris removal can be considered as a function of its downstream position (Hovius *et al.*, 2000). Subsequently the shift seen in landslide position following the Wenchuan earthquake, from higher and steeper slopes co-seismically to lower and shallower slopes post-seismically, suggests that the post-seismic landslide material is likely to reach the river network and be transported downstream more efficiently than the co-seismic landslide material. Results from the investigation into sediment aggradation in Beichuan could provide support for this claim as negligible amounts of aggradation were seen in the valley bottom following co-seismic landslide activity, whereas considerable levels of aggradation were noticed following the post-seismic landslide events in late September 2008 (Lin and Tang, 2009). However, the enhanced transport of material during and following post-seismic landsliding can also be attributed to increased levels of rainfall at this time. It is recognised that sediment transport and delivery is enhanced by high intensity rainfall due to high energy levels in the fluvial system and thus increased transport capacity (Preston, 2008). The influence of precipitation on the sediment system can be summarised as two main controls as suggested by Hovius *et al.* (2000): firstly as a trigger of landsliding, thus generating sediment supply; secondly as a supply of water, which aids sediment transport by enhancing surface runoff and the transport capacity of the channel network. Thus it is likely that the post-seismic increase in downstream sediment transport in the Beichuan area has been influenced by the heavy rainfall events (Lin and Tang, 2009) in addition to the location of landslides further downstream in the catchment. Work by Imazumi and Sidle (2007) further illustrates the influence of landslide positioning with respect to the river network in determining onward transport of sediment downstream.

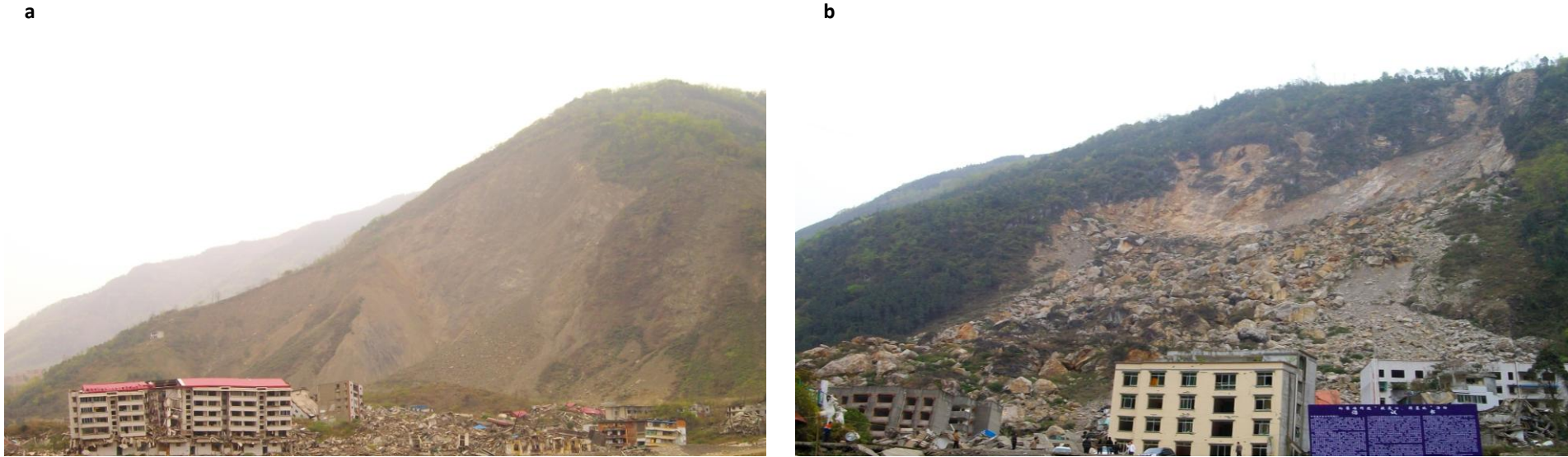


Figure 6.2: Differing landslide failures around Beichuan town – **a)** shows a long-runout slide in the hanging wall of the Beichuan fault; **b)** shows a large rockfall with a short runout in the footwall

6.2. Sediment movement: the impact of the volume of displaced material

Following landslide events, the volume of material which has been displaced has the potential to impact upon the landscape over both short-term and long-term time scales. In the following section the results from this study, particularly chapters 4 and 5, will be used to discuss both short-term and long-term impacts in the context of wider literature.

6.2.1. Short-term

Over shorter time scales, i.e. the 10 years following the earthquake event, the impacts of displaced material fall broadly into two categories: the potential for sediment transport; and the temporary storage of material both on the hillslope and valley floor. Following an earthquake, vast areas of highly unstable ground are left with the potential to contribute large volumes of sediment to downstream locations (Bucknam *et al.*, 2001). As has been shown by the results of this study, the Wenchuan earthquake is no exception to this statement as large volumes of material have been generated by both co-seismic and post-seismic landsliding (see section 4.3.1). The potential for onward transport of this material has been shown to be influenced by a variety of factors, primarily landslide location with respect to the channel network and the timing of landslide events in accordance with periods of intense rainfall.

Results of this study have illustrated the significant post-seismic landslide events and subsequent transport that occurred following the heavy monsoonal rains in September 2008 (Lin and Tang, 2009); and further transport that occurred up to August 2009. These results indicate that sediment dynamics are remaining very active post-earthquake, as expected (Matsuoka *et al.*, 2008) and further evidence indicates that they are continuing to do so: Annual monsoon storms have continued to devastate the region, causing increased widespread landsliding and sediment transport, as seen in the recent events of summer 2010 (BBC, 2010).

In addition to the material generated by landsliding and its transport downstream through the catchment, much of the material becomes temporarily stored at some stage as it moves from the hillslope to the river network. Material that becomes temporarily stored on the hillslope has the potential to be remobilised in future triggering events, i.e. heavy rainfall. From examination of satellite imagery and oblique photographs, in addition to field observations, many areas where material is stored on the hillslope can be identified. Some of this material has since become remobilised, i.e. during the monsoonal rains in summer 2010 (BBC, 2010) and much remains a potential hazard. Lower in the catchment, material also becomes

temporarily stored on the valley floor, as shown by the levels of sediment aggradation in Beichuan town (see section 5.3). As this material builds up it changes the potential for sediment transport out of the catchment: the angle of deposition increases as sediment aggrades to a point where sediment can no longer be deposited, rather it is transported directly into the river network. At this stage, the potential for sediment transport has become set primarily by the base level, (i.e. the angle of sediment deposition between the hillslope toe and the river) rather than by sediment supply. The catchment has become transport limited rather than supply limited (Hovius *et al.*, 2000).

Temporal changes in the volume of landslide material available for transport and in the volume of aggraded material on the valley floor have been illustrated in the graphs shown in Figure 5.8. This data was based on the 15 months following the earthquake event; a relatively short time frame with respect to longer-term trends, and therefore it is difficult to make assumptions as to how long such elevated rates of landslide activity will last. In the two years following the 2005 Kashmir earthquake (7.6 M_w) in Pakistan, elevated rates of sediment production and delivery to the river network were seen in monsoon and snowmelt seasons (Saba *et al.*, 2009; Owen *et al.*, 2008; Sato *et al.*, 2007). Long-term major slope failures were forecast beyond this (Dunning *et al.*, 2007), however Saba *et al.* (2010) discovered that after two years post-earthquake most slopes began regaining stability, re-vegetating and landslide activity significantly decreased. Similarly elevated rates of landslide activity and material transport were observed in the years following the 1999 Chi-Chi earthquake in Taiwan (Lin *et al.*, 2006). However subsequent typhoons for up to 6 years following the earthquake acted on the seismically weakened hillslopes to cause elevated rates of sediment activity to remain far beyond the initial post-earthquake period.

These examples illustrate the variation in post-earthquake sediment dynamics with different seismic events and locations, suggesting that the trends shown in these curves (Figure 5.8) provide a snapshot of post-earthquake sediment movement and do not show the full extent of the earthquake related sediment dynamics following the 2008 Wenchuan earthquake.

6.2.2. Long-term

Over longer timescales, i.e. 10s to 1,000s of years post-earthquake, it is expected that most of the material generated by earthquake-related landsliding will be transported out of the catchment and downstream through the river network. Whilst the sedimentary record of a landscape is likely to be dominated by the post-seismic inputs of sediment that occur as a

result of heavy rainfall, much of this material will have a co-seismic origin and have been remobilised by post-seismic activity (Hovius and Stark, 2006).

A comparison of landslide sediment volumes with downstream sediment volumes can provide an indication of the impact of landsliding on erosion, however it is questionable how well this erosional signature is preserved (Hovius *et al.*, 2000; 1997). This has been illustrated by the results from Beichuan, which display a significant difference in the volume of material between the landslides and aggraded sediment (see Chapter 5, Table 5.2). The difference in volumes can be attributed to material that is either temporarily stored on the hillslope or that has been transported downstream and out of the catchment; however it suggests that using only one assessment of downstream sediment volume is unlikely to provide an accurate measure of the erosion signature resulting from landsliding.

Assessing the significance of this one event, i.e. its erosional impact, is less problematic when viewed in the context of a longer time period. Erosion rates calculated from the volume of landslide material (see section 4.3.2) have been evaluated for the entire earthquake affected region (Parker *et al.*, in review) and compared with calculated rates of co-seismic rock uplift (deMichele *et al.*, 2010). This has revealed that co-seismic landsliding has eroded a much greater volume of material than rock uplift has generated suggesting that large earthquake events, such as the Wenchuan earthquake in 2008, are eroding more material than they are building. Whilst this may seem controversial when considered against the common theory that large earthquakes build mountains (Stein *et al.*, 1988), it is widely recognised that landslides are a principal supply of sediment in a mountain catchment (Pearce and Watson, 1986) and subsequently have been acknowledged as a dominant erosional agent (i.e. in the Southern Alps – Hovius, 1997). Therefore, it is not entirely surprising that the volume of material removed by earthquake generated landsliding is comparable to, if not greater than, the surface uplift (i.e. new material) generated by an earthquake (Guzzetti *et al.*, 2009; Larsen *et al.*, 2010).

6.3. In the context of wider literature on the Wenchuan earthquake

In the months following the Wenchuan earthquake a large amount of research was undertaken in the region, primarily in the form of post-earthquake hazard assessments, for example Chen *et al.* (2008) and Stone (2008). As a result a significant volume of literature exists that is focused upon details of the earthquake, immediate hazards (both geohazards and

infrastructure damages) and the subsequent production of hazards maps (i.e. Zifa, 2008). In the two years following, many investigations of co-seismic landsliding have been undertaken across the region focusing principally upon landslide mapping (Gong *et al.*, 2010; Parker, 2010; Sato and Harp, 2009); the distribution of landslides with respect to seismological parameters (Qi *et al.*, 2010; Yang *et al.*, 2010); and the relationship between landslide occurrence and geophysical variables, including slope, aspect and geology as key parameters (Chigira *et al.*, 2010; Dai *et al.*, 2010). The following discussion outlines the areas where this work has significantly contributed to this existing body of literature, detailing specifically where it has addressed outstanding issues and provided new information as an extension to these studies.

6.3.1. Post-seismic landslide evolution

As a result of many previous studies, co-seismic landslides across large areas of the earthquake affected region have been mapped and analysed (Yin, 2010). Subsequently a large volume of literature exists, which describes the distribution of co-seismic landslides and offers explanations for the parameters that control this (i.e. Sato and Harp, 2008; Dai *et al.*, 2010). Whilst this is crucial in understanding the impact of the earthquake event, previous events suggest that equally (if not more) significant geomorphic activity can occur post-seismically (Chen and Petley, 2005). For example, studies following the 1999 Chi-Chi earthquake in Taiwan showed that the rate of landsliding remained high for a number of years after the earthquake (Dadson *et al.*, 2004; Lin *et al.*, 2006; 2008). In this case, large rainstorms caused by typhoons triggered the failure of slopes that had been pre-weakened by the earthquake (Dadson *et al.*, 2004). Often such post-seismic activity is less well documented than the co-seismic activity (Chen and Petley, 2005), which can be seen in the collection of studies (to date) following the Wenchuan earthquake. This is as expected considering the time frame, however many co-seismic investigations have alluded to potential post-seismic geohazards and highlighted the need for further study: for example, both Yin *et al.* (2009) and Yang *et al.* (2010) describe the co-seismic landslide distribution and note more than 10,000 potential geohazard sites that have resulted from the seismic activity. They highlight the concern amongst researchers as to what will happen at these sites during the annual rain seasons (Yang *et al.*, 2010). Thus, the results of this work (specifically chapter 3), has critically provided information on the post-seismic landslide activity; the distribution of failures and the relationship between landslides and seismic, geologic and topographic variables. This allows the temporal changes in landscape response to the earthquake to be observed and provides further information that can be significantly used in geohazard planning and prediction (Yin *et al.*, 2010).

6.3.2. (Re) mobilisation of material

Providing an extension not only to previous studies but also to the analysis of post-seismic landslides in the Beichuan region, the assessment of landslide volume and sediment aggradation volume for the Beichuan area has contributed to the understanding of the mobilisation of landslide deposit materials. Parker (2010) highlights the remobilisation of sediment as an additional hazard in relation to rainfall events and specifies landslide mapping and sediment volume estimation as essential components required in order to study this. In addition to the mobilisation of hillslope deposits, other investigations have also noted the mobilisation of valley floor materials in relation to a build up in water pore pressure (i.e. Chigira *et al.*, 2010), highlighting the significance of the rainy season.

Some of the co-seismic landslide investigations had addressed the issue of landslide volume by applying an established, global volume scaling law (i.e. Larsen *et al.*, 2010; Guzzetti *et al.*, 2009) to the entire study area (Parker, 2010). Whilst this provided an estimate of total landslide material, the results were weakly constrained with a range over an order of magnitude. Thus the development and application of a volume scaling law specific to the Beichuan area, has significantly improved upon the accuracy of landslide volume estimations and subsequently allows the hazard of sediment remobilisation to be more correctly assessed. In addition to estimating landslide sediment volume, developing a method to quantify the volume of aggraded sediments on the valley floor has provided an additional measure of mobilised sediment in the Beichuan area. Valley-floor deposits from landslide material provide an indication of the geomorphic impact of landslides associated with the Wenchuan earthquake (Parker, 2010). However, within the current literature regarding sediment dynamics following the Wenchuan earthquake, the volume of aggraded valley-floor sediments has not been quantified and thus the results of this for the Beichuan area (Chapter 5) add essential, new information to the catchment model (Figure 6.3).

Improved estimations of sediment volume also provide more accurate erosion rates (section 4.3.2), which can be used to better understand the role of the 2008 Wenchuan earthquake in the long-term landscape evolution of the Longmen Shan. Prior to the earthquake, calculations of short-term erosion rates, i.e. for the last 2000-3000 years, were much lower than the long-term erosion rates, i.e. for the last 8-10 Ma (Ouimet *et al.*, 2009). A study by Ouimet (2010) suggests that the landslide erosion associated with the Wenchuan earthquake should be integrated into the short-term rate in order to account for the discrepancy between the short- and long-term erosion rates. However, they are clear that there are many assumptions in

calculating the landslide erosion rate associated with the earthquake and call for an improved estimate of the eroded sediment budget through both landslides and subsequent sediment transport processes. This work has begun to provide this for the Beichuan area through the development of a volume scaling law and the calculation of aggraded sediment volumes.

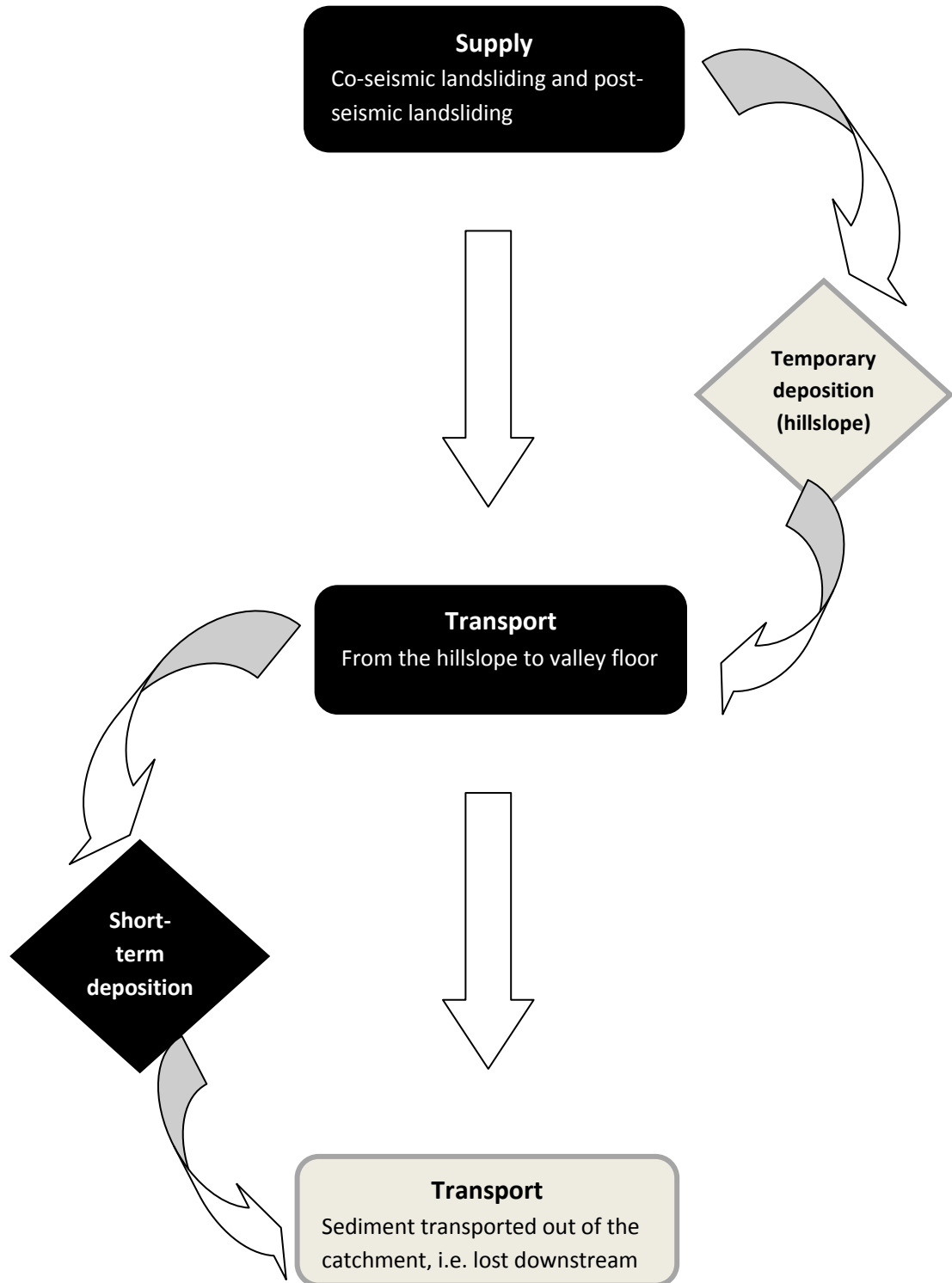


Figure 6.3: Flow diagram of sediment movement through a typical catchment. Highlighted areas (black) indicate what has already been addressed in previous chapters and areas outlined in red indicate the focuses of this chapter.

6.4. Evaluation of the resources and techniques used

6.4.1. Satellite imagery

The results of landslide mapping (Chapter 3) show that the total area covered by landslides decreased between June and October 2008, before increasing again between October 2008 and March 2009. This suggests a rapid healing of co-seismic landslide scars and few new post-seismic failures in this time period. However based upon what is seen in oblique photographs and from conversations with scientists in the area (Huang, 2010 *per coms*), neither of these scenarios is likely. Figure 6.4 shows high-density landsliding around Beichuan town in July and November 2008; as can be seen from these photographs, the amount of landsliding did not decrease in area between these dates and in certain locations new post-seismic failures can be identified, supporting the idea that the results from chapter 3 are not in agreement with what is seen on the ground.

Further inspection of the satellite imagery used and the resulting landslide maps has revealed a possible explanation for this error. As shown in Figure 6.5, classification of the panchromatic SPOT-5 image (October 2008) has omitted some failures as they were not contrasting enough compared to undisturbed ground in order to be identified by the classification technique. Thus, despite the application of an established mapping algorithm (Parker, 2010) and additional filters (see section 3.1) the resulting classification of landslides on the October 2008 image (S2) is not directly comparable with the June 2008 (S1) and March 2009 (S3) images. Given this issue, the most accurate and reliable depiction of temporal change in landslide occurrence is gained by comparing only the results from June 2008 and March 2009.

This error in landslide classification indicates that using different types of imagery can present problems for studies where the results need to be comparable. The panchromatic image used in this study (S2) required a different classification method to the multispectral images used (S1 and S3) and subsequently error was seen in the results.

6.4.2. Volume scaling laws

The establishment of a scaling law specific to the study area of this research was the most accurate method of estimating landslide volume, given the time and resource limitations. To improve upon this, more field measurements could be taken and factored into the regression

analysis; alternatively if a high resolution DEM is available both pre- and post-landslide events then they can be used to evaluate the change in depth.

Accuracy in the calculations of sediment volume is dependent upon the accuracy of the parameters: area and depth. Measurements of landslide area were gained from satellite imagery and thus present the following potential error: firstly, both the scar and the deposit were included in the area as it is often not possible to resolve the difference between them from the imagery; secondly, many small landslides that are clustered together have been delineated as one large landslide owing to image resolution (Figure 6.6). Both of these potential errors result in an overestimation of landslide area and thus an overestimation of landslide volume.

When applying the volume scaling law, it is most accurate and reliable in the area it was developed in (Larsen *et al.*, 2010). Therefore the scaling relationship developed in this work is the most accurate estimation of landslide volume for the Beichuan area; however its reliability will depend on the type and size of the landslide it is applied to. For example, within the sample of landslides measured and used to develop the relationship there were fewer larger failures (> 16 m deep) compared to small and medium failures (2 – 16 m deep); as a result the scaling relationship is likely to produce a more accurate result when applied to a small or medium sized failure. The same principle also applies to the type and geology of the landslide.

6.4.3. Oblique photographs and sediment aggradation technique

Investigating the role of sediment storage within a catchment is crucial for developing an understanding of the sediment budget; it also provides another link between sediment dynamics and landscape evolution (Otto *et al.*, 2008). The innovative oblique photograph technique has provided a unique way of obtaining sediment storage volumes for Beichuan town, which does not rely on various estimation techniques that can often produce a large uncertainty and error in estimation (Otto *et al.*, 2008). Results have shown that the evaluation of sediment depth using this technique is accurate to within 15% of the actual value (section 5.2). This error band can be attributed to factors relating to the use of photographs: distance between the camera and object; photograph quality; lighting; and ease of identification. With this understanding, any future application of this technique can seek to minimise the influence of these factors, thus improving further upon the accuracy of the results.

The primary limitation of the oblique photograph technique is the reliance on a wealth of available photographs of the chosen study area from a wide spatial and temporal range. However if this resource is available then the technique provides a simple and effective

method of remotely constraining sediment depth. It is far less time- or financially- intensive than in-field measurements and provides much more reliable results than estimations from other imagery, i.e. satellite imagery, where depth cannot be constrained.

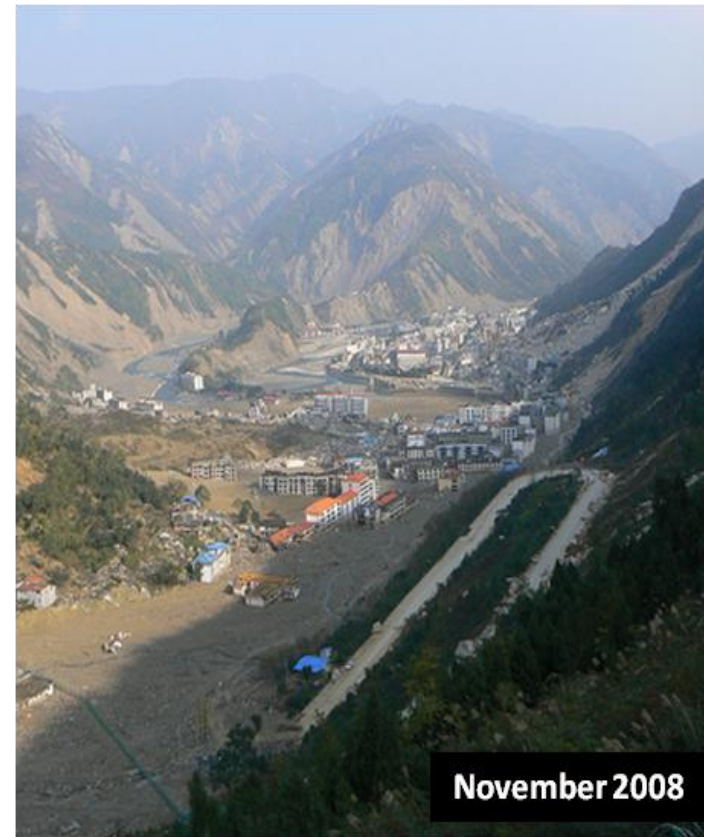


Figure 6.4: Oblique photographs displaying high-density landsliding around Beichuan town in July 2008 and November 2008. July 2008 photograph credited to Lynn Highland, USGS; November 2008 photograph credited to Melanie Rodriguez, BBC

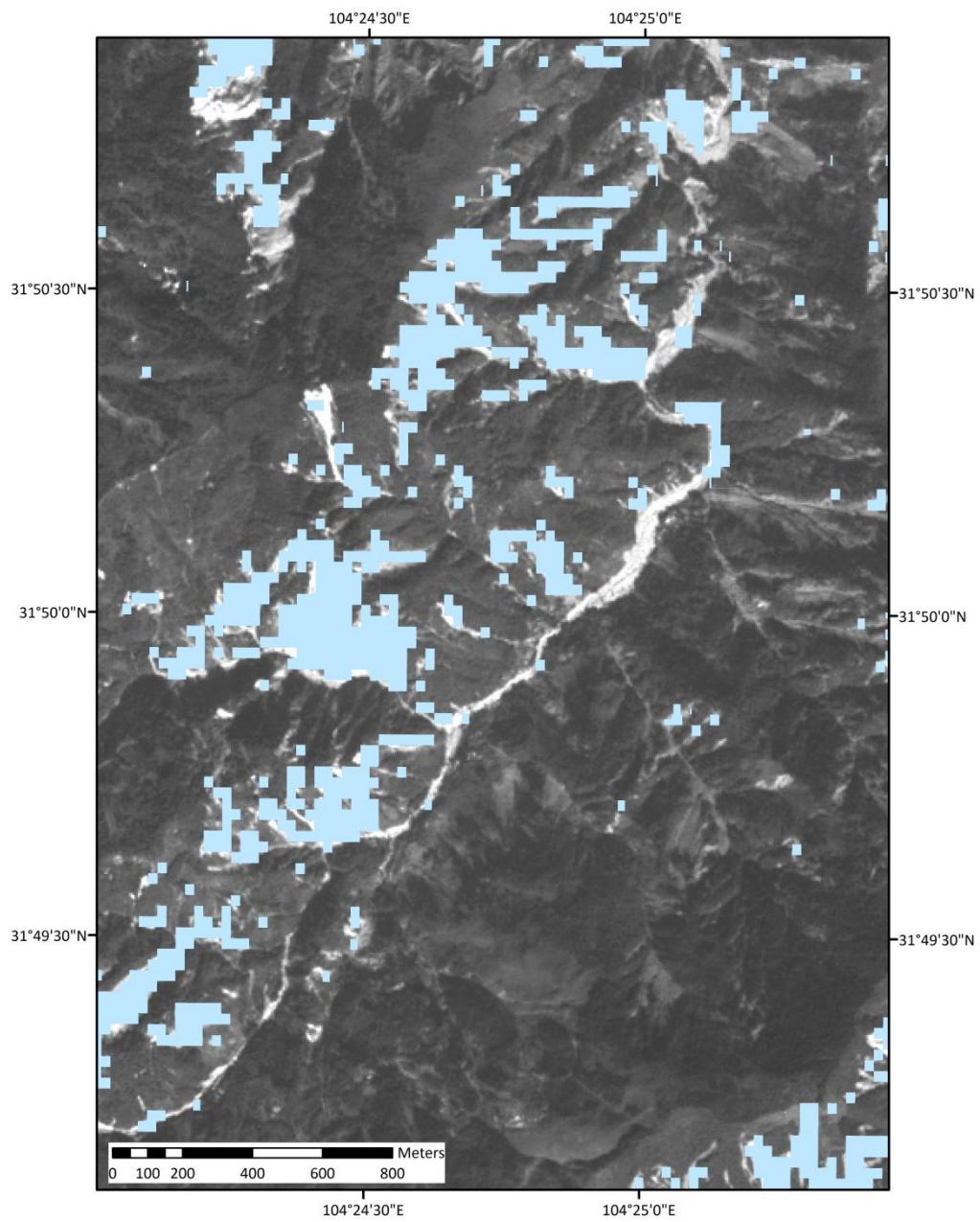


Figure 6.5: Automated landslide mapping of image S2 – visible landslides (white and light grey) indicate areas of omission by the classification due to image brightness

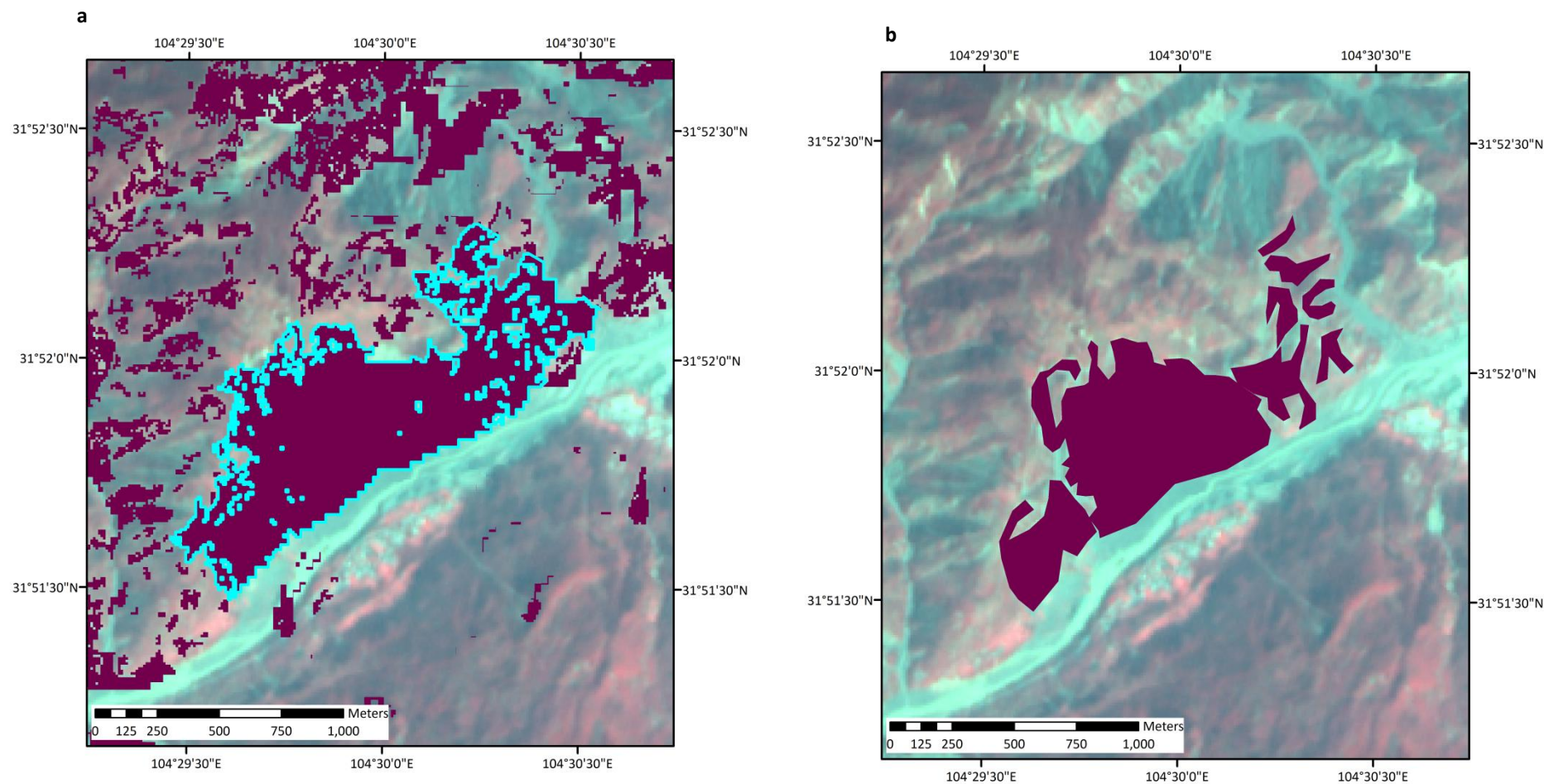


Figure 6.6: An example of coalescence of landslides during mapping: the large combined failure in **a** generates a calculated landslide volume = $1.8 \times 10^7 \text{ m}^3$, whereas the individual landslides (mapped manually) in **b** generate a total landslide volume of $8.7 \times 10^6 \text{ m}^3$

7. Conclusions

This work began with the aim to assess the controls upon and impact of the mobilisation of debris released by landslides triggered during the Wenchuan Earthquake in China, May 2008. Using a combination of desk-based and field-based research, the research objectives have been achieved as landslide sediments have been considered at the source, transfer and deposition stages within the catchment. This contributes to the knowledge and understanding of the impact of the Wenchuan earthquake upon landscape scale sediment dynamics. The main findings of this research are summarised according to stages in the conceptual model which describes sediment movement through the catchment (Figure 6.3); this model was introduced in Chapter 2 of this study and has been referred to throughout to illustrate the contribution of knowledge at each stage.

7.1. Main findings

The supply of sediment generated by co-seismic and post-seismic landsliding has been evaluated using satellite imagery and volume-area scaling relationships. Using the results of landslide mapping from satellite imagery, seismological, topographical and geological controls have all been examined to assess their influence upon the occurrence of landslides. Whilst some variables appear to exert a stronger influence over landslide occurrence and distribution than others, the results and discussion of this study suggest that primarily a combination of these parameters are needed to generate landsliding. Thus it is difficult to fully separate and individually evaluate the controls on sediment supply from landsliding.

Establishing a volume-area scaling relationship specific to the Beichuan region has provided a sufficiently accurate assessment of the volume of material eroded by landsliding. In support of recent work from Parker *et al.* (2010), the results suggest that the Wenchuan earthquake has most likely eroded more material through landsliding than it has built through co-seismic surface uplift. The landslide volume estimations were further used to compare with the findings from quantifying sediment aggradation, providing a comparison between sediment supply and (temporary) deposition. This serves to ensure that landsliding and sediment dynamics have been evaluated at each stage in the conceptual model (Figure 6.3). Results of this comparison have reassuringly indicated a much lower volume of material deposited in the valley compared to that generated by landsliding, suggesting that a large proportion of material has remained temporarily stored on the hillslope or has become transported

downstream out of the catchment. Whilst neither of these volumes have been constrained in this study, it has served to inform and highlight of the potential hazard that remains in the form of loose material on the hillslope and large volumes of material in the river network.

In addition to evaluating sediment dynamics at different stages within the catchment, this study has also examined temporal changes in the supply and deposition of material. Overall, the landslide distribution has become more widespread over time. Furthermore, results have shown that the seismological parameters controlling co-seismic landslide occurrence also exert influence over the distribution of post-seismic failures as slopes are weakened by seismic activity and thus more susceptible to failure. Other temporal changes, for example the distribution of landslides across geologic units, have demonstrated the differing response of geological and topographical parameters to different triggers of landslides. Certain slopes (defined by gradient, aspect, elevation and/or geology) are more susceptible to seismic shaking, whereas others are more susceptible to post-seismic rainfall events.

Temporal changes in material deposition have been illustrated through the case study of sediment aggradation in Beichuan town. The results have shown that times of elevated sediment deposition coincide with periods of intense rainfall, as expected due to the increased transport capacity at this time.

7.2. Contribution to knowledge

This study has provided information to aid the prediction and assessment of future sediment transport in the Sichuan area, and importantly offers both results and techniques that can be used to inform the response of other areas impacted upon by catastrophic earthquakes, particularly where no direct field measurements are available. Post-earthquake assessments often focus upon instantaneous events, however this study has built upon that by investigating the geomorphological aftermath, providing insight into the role of earthquakes in landscape evolution. In doing so, the development and application of various techniques has furthered existing geographical knowledge, including:

- Extending an existing database of the pre- and post- earthquake conditions in Sichuan, building upon research from Parker (2010) amongst others;
- Establishing relationships between landslide geometry and sediment volume to enable quantitative estimates of sediment mobilisation, advancing research into the relationship between landslide sediment supply and yield. This has built upon work from Larsen *et al.* (2010) and Guzzetti *et al.* (2009) with regards volume-area scaling

relationships, and also has further developed ideas from Imaizumi and Sidle (2007) and Malamud *et al.* (2004) regarding landslide sediment supply and mobilisation;

- Methodological innovation of constraining the vertical aggradation of sediment using oblique imagery.

7.3. Future research

Understanding the evolution of post-earthquake landsliding and the controls upon this has been well established through this research and the many previous studies that it has built upon. This study has quantified the volume of landslide material at the supply and deposition stages, providing a unique understanding of this in the Beichuan area. Conversely, the temporary deposition of material on the hillslope is not well constrained and subsequently presents an unknown store of material within the catchment system. Investigating this store would serve two key purposes in future research: firstly to quantify the amount of material that remains a potential hazard on the hillslope, thus also indicating how much material has already been transported; and secondly to examine the location of hillslope deposits with respect to the river network in order to further investigate connectivity between the hillslope and channel. The remaining unknown in the model of sediment movement (Figure 6.3) is the amount of material which is transported out of the catchment that it had been eroded from. Quantifying this volume of material is recommended for future studies as it would augment the calculated erosion rates and signify the longevity of the impact of earthquake-related sediment dynamics on the landscape.

References

- Barnard, P.L., Owen, L.A., Sharma, M.C. and Finkel, R.C. 2001: Natural and human-induced landsliding in the Garhwal Himalaya of northern India, *Geomorphology*, 40: 21-35.
- BBC (2010) 'Rain triggers fresh China landslides', *BBC News Asia-Pacific* (<http://www.bbc.co.uk/news/world-asia-pacific-10961252>, accessed 15/11/2010)
- Borghius, A.M., Chang, K. and Lee, H.Y. (2007) Comparison between automated and manual mapping of typhoon-triggered landslides from SPOT-5 imagery, *International Journal of Remote Sensing*, 28: 1843-1856
- Bucknam, R.C., Coe, J.A., Chavarria, M.M., Godt, J.W., Tarr, A.C., Bradley, L.A., Rafferty, S., Hancock, D., Dart, R.L. and Johnson, M.L. (2001) Landslides triggered by hurricane Mitch in Guatemala – inventory and discussion, *USGS Open File Report: 01-443*, USGS
- Bull, W.B. (2009) 'Chapter 4: Sediment Yield and Landslides', in Bull, W.B. (2009) *Tectonically Active Landscapes*, Wiley-Blackwell: Oxford, pp.97-128
- Chang, K.T., Chiang, S.H. and Hsu, M.L. 2007: Modeling typhoon- and earthquake-induced landslides in a mountainous watershed using logistic regression, *Geomorphology*, 89: 335-347
- Chen, Y., Li, L., Li, J. and Li, G. (2008) Wenchuan Earthquake: Way of thinking is changed, *Episodes*, 31(4): 374-377
- Chen, H. and Petley, D. (2005) The impact of landslides and debris flows triggered by Typhoon Mindulle in Taiwan, *Quarterly Journal of Engineering Geology and Hydrogeology*, 38: 301-304
- Chen, S.C. and Wu, C.H. (2009) Landslide restoration on Mt.99 peaks after ChiChi earthquake in Taiwan. In Lee, C.T. (ed) *The Next Generation of Research on Earthquake-induced Landslides: An International Conference in Commemoration of 10th Anniversary of Chi-Chi Earthquake*, National Central University, Taiwan: National Central University, pp.344-359.
- Cheng, K.S., Wei, C. and Chang, S.C. (2004) Locating landslides using multi-temporal satellite images, *Advances in Space Research*, 33(3): 296-301
- Chigira, M., Wu, X., Inojuchi, T. and Wang, G. (2010) Landslides induced by the 2008 Wenchuan earthquake, Sichuan, China, *Geomorphology*, 118: 225-470
- Chuang, S.C., Chen, H., Lin, G.W., Lin, C.W. and Chang, C.P. 2009: Increase in basin sediment yield from landslides in storms following major seismic disturbance. *Engineering Geology* 103: 59-65.
- Cole, W.F., Marcum, D.R. and O'Shires, P. (1998) Analysis of earthquake-reactivated landslides in the epicentral region, central Santa Cruz Mountains, California. In Keefer, D.K. (ed) *The Loma*

- Prieta, California, earthquake of October 17, 1989: Landslides: U.S. Geological Survey Professional Paper 1551-C pp.165-185.
- Dadson, S.J., Hovius, N., Chen, H., Dade, W.B., Lin, J.C., Hsu, M.L., Lin, C.W., Horng, M.J., Chen, T.C., Milliman, J. and Stark, C.P. 2004: Earthquake-triggered increase in sediment delivery from an active mountain belt, *Geology* 32: 733-736
- Dai, F.C., Xu, C., Yao, X., Xu, L., Tu, X.B. and Gong, Q.M. (2010) Spatial distribution of landslides triggered by the 2008 Ms 8.0 Wenchuan earthquake, China, *Journal of Asian Earth Sciences* (in press)
- Davies, T.R. and **Korup, O.** (2010) 'Sediment cascades in active landscapes' in: Burt, T.P. and Allison, R.J. (eds) *Sediment cascades: An Integrated Approach*, Wiley-Blackwell: Chichester, pp. 89-115.
- De La Ville, N., Chumaceiro Diaz, A. and Ramirez, D. (2002) Remote Sensing and GIS Technologies as Tools to Support Sustainable Management of Areas Devastated by Landslides, *Environment, Development and Sustainability*, 4(2): 221-229
- De Michele, M., (2010) Three-dimensional surface displacement of the 2008 May 12 Sichuan earthquake (China) derived from Synthetic Aperture Radar: evidence for rupture on a blind thrust, *Geophysical Journal International*, 183(3): 1097
- Densmore, A.L., Anderson, R.S., McAdoo, B.G. and Ellis, M.A. 1997: Hillslope Evolution by Bedrock Landslides. *Science* 275, 369-372.
- Densmore, A.L. and Hovius, N. 2000: Topographic fingerprints of bedrock landslides. *Geology* 28: 371-374.
- Densmore, A.L., Li, Y., Richardson, N.J., Zhou, R., Ellis, M. and Zhang, Y. (in review) The role of late Quaternary upper-crust faults in the 12 May 2008 Wenchuan earthquake
- Dunning, S.A., Mitchell, W.A., Rosser, N.J. and Petley, D.N. (2007) The Hattian Bala rock avalanche and associated landslides triggered by the Kashmir Earthquake of 8 October 2005, *Engineering Geology*, 93(3-4): 130-144
- Fan, H. and Cai, Q. (2005) A suspended sediment budget for the Liu River basin, China, *Sediment Budgets 1 (Proceedings of symposium S1 held during the Seventh IAHS Scientific Assembly at Foz do Iguacu, Brazil, April 2005)*
- Gallant, J.C. and Hutchinson, M.F. (1996) Towards an understanding of landscape scale and structure, *Proceedings of the Third International Conference/Workshop on Integrating GIS and Environmental Modeling*, National Center for Geographical Information and Analysis: Santa Barbara, CA

- Galli, M., Ardizzone, F., Cardinali, M., Guzzetti, F. and Reichenbach, P. (2008) Comparing landslide inventory maps, *Geomorphology*, 94(3-4): 268-289
- Geosolution (2006) 'LaserAce Hypsometer', *Laser Devices: MDL: LaserAce Hypsometer* (http://www.geosolution.com/mdl_hypsometer.htm, accessed 10/03/2010)
- Gong, J., Wang, D., Li, Y., Zhang, L., Yue, Y., Zhou, J. and Song, Y. (2010) Earthquake-induced geological hazards detection under hierarchical stripping classification framework in the Beichuan area, *Landslides*, DOI 10.1007/s10346-010-0201-4
- Guzzetti, F., Carrara, A., Cardinali, M. and Reichenbach, P. 1999: Landslide hazard evaluation: a review of current techniques and their application in a multi-scale study, Central Italy, *Geomorphology* 31: 181-216
- Guzzetti, F., Ardizzone, F., Cardinali, M., Galli, M., Reichenbach, P. and Rossi, M. (2008) Distribution of landslides in the Upper Tiber River basin, central Italy, *Geomorphology*, 96(1-2): 105-122
- Guzzetti, F., Ardizzone, F., Cardinali, M., Rossi, M. and Valigi, D. (2009) Landslide volumes and landslide mobilization rates in Umbria, central Italy, *Earth and Planetary Science Letters* 279: 222-229.
- Harp, E.L. and Jibson, R.W. (1996) Landslides triggered by the 1994 Northridge, California, earthquake, *Bulletin of the Seismological Society of America*, 86: 319-332
- Hervas, J. and Bobrowsky, P. (2009) Mapping: Inventories, Susceptibility, Hazard and Risk, in Sassa, K. and Canuti, P. *Landslides – Disaster Risk Reduction*, Berlin: Springer-Verlag pp.321-349
- Hovius, N., Stark, C.P. and Allen, P.A. (1997) Sediment flux from a mountain belt derived by landslide mapping, *Geology*, 25: 231-234
- Hovius, N., Stark, C.P., Chu, H.T. and Lin, J.C. 2000: Supply and removal of sediment in a landslide-dominated mountain belt: Central Range, Taiwan, *Journal of Geology*, 108: 73-89
- Hovius, N. and Stark, C.P. (2002) Landslide-driven erosion and topographic evolution of active mountain belts. In Evans, S.G., Mugnozza, G.S., Strom, A. and Hermanns, R.L. (eds) *NATO Advanced Research Workshop on Massive Rock Slope Failure - New Models for Hazard Assessment*, Celano, ITALY, pp. 573-590
- Hovius, N., Meunier, P., Haines, A.J., Lin, C.W., Chen, H., Dadson, S. and Horng, M.J. (2009) Patterns of Seismically Induced Landsliding and the Mass Balance of a Large Earthquake. In Lee, C.T., (ed) *The Next Generation of Research on Earthquake-induced Landslides: An International Conference in Commemoration of 10th Anniversary of Chi-Chi Earthquake*, National Central University, Taiwan National Central University, pp.319-321

- Huang, R.Q. and Li, W.L. (2009a) Development and distribution of geohazards triggered by the 5.12 Wenchuan Earthquake in China, *Science in China Series E: Technological Sciences*, 52(4): 810-819
- Huang, R. Q. and Li, W. L. (2009b) Analysis of geo-hazards triggered by the 12 May 2008 Wenchuan Earthquake, China, *Bulletin of Engineering Geology and the Environment*, 68: 363-371
- Imaizumi, F. and Sidle, R.C. (2007) Linkage of sediment supply and transport processes in Miyagawa Dam catchment, Japan, *Journal of Geophysical Research*, 112: F03012
- Jen, C.H., Lin, J.C., Hsu, M.L. and Petley, D.N. (2004) Fluvial transportation and sedimentation of the Fu-shan small experimental catchments, *Quaternary International*, 147: 34-43
- Keefer, D.K. (1984) Landslides caused by earthquakes, *Geological Society of America Bulletin*, 95(4): 406-421
- Keefer, D.K. (1994) The importance of earthquake-induced landslides to long-term slope erosion and slope-failure hazards in seismically active regions, *Geomorphology*, 10:265-284
- Keefer, D.K. (1999) Earthquake-induced landslides and their effects on alluvial fans. *Journal of Sedimentary Research*, 69: 84-104
- Keefer, D.K. (2000) Statistical analysis of an earthquake-induced landslide distribution -- the 1989 Loma Prieta, California event. *Engineering Geology*, 58:231-249.
- Keefer, D.K. (2002) Investigating landslides caused by earthquakes - A historical review. *Surveys in Geophysics*, 23: 473-510.
- Keefer, D.K. and Larsen, M.C. (2007) Geology: Assessing Landslide Hazards, *Science*, 316: 1136-1138.
- Korup, O., McSaveney, M.J. and Davies, T.R.H. (2004) Sediment generation and delivery from large historic landslides in the Southern Alps, New Zealand, *Geomorphology*, 61: 189-207
- Korup, O., Densmore, A.L. and Schlunegger, F. (2009) The role of landslides in mountain range evolution, *Geomorphology* (In Press, Corrected Proof)
- Larsen, I.J., Montgomery, D.R. and Korup, O. (2010) Landslide erosion controlled by hillslope material, *Nature Geoscience* (advance online publication)
- Lee, C.T., Huang, C.C., Lee, J.F., Pan, K.L., Lin, M.L. and Dong, J.J. (2008) Statistical approach to earthquake-induced landslide susceptibility, *Engineering Geology*, 100: 43-58
- Lillesand, T.M. and Keefer, D.K. (2004) *Remote Sensing and Image Interpretation*, New York: Wiley

- Lin, J.C., Petley, D., Jen, C.H., Koh, A. and Hsu, M.L. (2006) Slope movements in a dynamic environment - A case study of Tachia River, Central Taiwan. *Quaternary International*, 147: 103-112
- Lin, G.W., Chen, H., Hovius, N., Horng, M.J., Dadson, S., Meunier, P. and Lines, M. (2008) Effects of earthquake and cyclone sequencing on landsliding and fluvial sediment transfer in a mountain catchment, *Earth Surface Processes and Landforms*, 33: 1354-1373
- Lin, J.-C. and Tang, C. (2009) Landslide Hazard Assessment of the 2008 Wenchuan Earthquake: A Case Study in Beichuan Area, in Lee, C.T. (ed) *The Next Generation of Research on Earthquake-induced Landslides: An International Conference in Commemoration of 10th Anniversary of Chi-Chi Earthquake*, National Central University, Taiwan: National Central University, pp.85-90
- Malamud, B.D., Turcotte, D.L., Guzzetti, F. and Reichenbach, P. (2004a) Landslide inventories and their statistical properties, *Earth Surface Processes and Landforms*, 29(6): 687-711
- Malamud, B.D., Turcotte, D.L., Guzzetti, F. and Reichenbach, P. (2004b) Landslides, earthquakes, and erosion, *Earth and Planetary Science Letters*, 229: 45-59
- Martha, T.R., Kerle, N., Jetten, V., van Westen, C.J. and Kumar, K.V. (2010) Characterising spectral, spatial and morphometric properties of landslides for semi-automatic detection using object-oriented methods, *Geomorphology*, 116:24-36
- Martin, Y., Rood, K., Schwab, J.W. and Church, M. (2002) Sediment transfer by shallow landsliding in the Queen Charlotte Islands, British Columbia, *Canadian Journal of Earth Sciences*, 39: 189-205
- Matsuoka, A., Yamakoshi, T., Tamura, K., Maruyama, J. and Ogawa, K. (2008) Sediment yield from seismically-disturbed mountainous watersheds revealed by multi-temporal aerial LiDAR surveys, *Sediment Dynamics in Changing Environments (Proceedings of a symposium held in Christchurch, New Zealand, December 2008)*, pp.208-216
- McKean, J. and Roering, J. (2004) Objective landslide detection and surface morphology mapping using high-resolution airborne laser altimetry, *Geomorphology*, 57(3-4): 331-351
- Metternicht, G., Hurni, L. and Gogu, R. (2005) Remote sensing of landslides: An analysis of the potential contribution to geo-spatial systems for hazard assessment in mountainous environments, *Remote Sensing of the Environment*, 98(2-3): 284-303
- Meunier, P. and Hovius, N. (2006) Properties of earthquake and rainfall-triggered landslides, *Geophysical Research Abstracts*, 8:08480.
- Meunier, P., Hovius, N. and Haines, A.J. (2007) Regional patterns of earthquake-triggered landslides and their relation to ground motion, *Geophysical Research Letters*, 34: L20408

- Meunier, P., Hovius, N. and Haines, J.A. (2008) Topographic site effects and the location of earthquake induced landslides, *Earth and Planetary Science Letters*, 275: 221-232
- NASA (2009) 'ASTER Global Digital Elevation Map Announcement', *ASTER: Advance Spaceborne Thermal Emission and Reflection Radiometer* (<http://asterweb.jpl.nasa.gov/gdem.asp>, accessed 15/08/2010)
- Nichol, J. and Wong, M.S. (2005) Detection and interpretation of landslides using satellite images, *Land Degredation and Development*, 16: 243-255
- Otto, J.C., Goetz, J. and Schrott, L. (2008) Sediment storage in Alpine sedimentary systems – quantification and scaling issues, *Sediment Dynamics in Changing Environments (Proceedings of a symposium held in Christchurch, New Zealand, December 2008)*, pp.258-265
- Ouimet, W., Whipple, K.X., Royden, L.H., Sun, Z.M. and Chen, Z.L. (2007) The influence of large landslides on river incision in a transient landscape: Eastern margin of the Tibetan Plateau (Sichuan, China), *Geological Society of America Bulletin*, 119(11-12): 1462-1476
- Ouimet, W., Whipple, K. and Granger, D. (2009) Beyond threshold hillslopes: channel adjustment to base-level fall in tectonically active mountain ranges, *Geology*, 37: 579-582
- Ouimet, W. (2010) Landslides associated with the May 12, 2008 Wenchuan earthquake: Implications for the erosion and tectonic evolution of the Longmen Shan, *Tectonophysics*, 491: 244-252
- Owen, L.A., Kamp, U., Khattak, G.A., Harp, E.L., Keefer, D.K. and Bauer, M.A. (2008) Landslides triggered by the 8 October 2005 Kashmir earthquake, *Geomorphology*, 94: 1-9
- Parise, M. And Jibson, R.W. (2000) A seismic landslide susceptibility rating of geologic units based on analysis of characteristics of landslides triggered by the 17 January, 1994 Northridge, California earthquake, *Engineering Geology*, 58: 251-270
- Parker, R.N., Rosser, N., Densmore, A.L. and Petley, D. (2009) Automated Landslide Detection Algorithms to Investigate Controls on the Spatial Distribution of Landslides Triggered by the Wenchuan Earthquake, Sichuan Province, China. In Lee, C.T., editor, *The Next Generation of Research on Earthquake-induced Landslides: An International Conference in Commemoration of 10th Anniversary of Chi-Chi Earthquake*, National Central University, Taiwan: National Central University, 27-32.
- Parker, R.N. (2010) *Controls on the distribution of landslides triggered by the 2008 Wenchuan earthquake, Sichuan Province, China*, (thesis submitted for Master of Science) Durham University

- Parker, R.N., Densmore, A.L., Rosser, N.J., deMichele, M., Yong, L., Huang, R., Whadcoat, S. and Petley, D. (2010) Do large earthquakes build topography? Landsliding and orogenic volume change in the 12 May 2008 M_w 7.9 Wenchuan earthquake (*in review*)
- Pearce, A.J. and Watson, A.J. (1986) Effects of earthquake-induced landslides on sediment budget and transport over a 50-yr period, *Geology*, 14: 52-55
- Peart, M.R., King, J.P. and Ruse, M.E. (2005) Sediment production by landslides in Hong Kong: two case studies. *Sediment Budgets 1 (Proceedings of symposium S1 held during the Seventh IAHS Scientific Assembly at Foz do Iguacu, Brazil, April 2005)*, pp.29-37
- Perry and Taylor (2007) Environmental Sedimentology: Introduction, In: Perry, C. & Taylor, K. *Environmental Sedimentology*. Oxford: Blackwell; 2007: 1-31
- Preston, N.J. (2008) Off-slope sediment delivery from landsliding during a storm, Muriwai Hills, North Island, New Zealand, *Sediment Dynamics in Changing Environments (Proceedings of a symposium held in Christchurch, New Zealand, December 2008)*, pp. 237-241
- Qi, S., Xu, Q., Lan, H., Zhang, B. and Liu, J. (2010) Spatial distribution analysis of landslides triggered by 2008.5.12 Wenchuan Earthquake, China, *Engineering Geology*, 116: 95-108
- Rice, R.M., Corbett, E.S. and Bailey, R.G. (1969) Soil slips related to vegetation, topography, and soil in Southern California, *Water Resources Research*, 5(3): 647-659
- Rice, R.M. and Foggin III, G.T. (1971) Effects of high intensity storms on soil slippage on mountainous watersheds in Southern California, *Water Resources Research*, 7(6): 1485-1496
- Richardson, N.J., Densmore, A.L., Seward, D., Fowler, A., Wipf, M., Ellis, M.A., Yong, L. and Zhang, Y. (2008) Extraordinary denudation in the Sichuan Basin: Insights from low-temperature thermochronology adjacent to the eastern margin of the Tibetan Plateau, *Journal of Geophysical Research-Solid Earth*, 113(B4)
- Saba, S.B., van der Meijde, M. and van der Werff, H. (2010) Spatiotemporal landslide detection for the 2005 Kashmir earthquake region, *Geomorphology*, 124:17-25
- Sato, H., Hasegawa, H., Fujiwara, S., Tobita, M., Koarai, M., Une, H., Iwahashi, J. (2007) Interpretation of landslide distribution triggered by the 2005 Northern Pakistan earthquake using SPOT 5 imagery, *Landslides*, 4(2): 113-122
- Sato, H.P. and Harp, E.L. (2009) Interpretation of earthquake-induced landslides triggered by the 12 May 2008, M7.9 Wenchuan earthquake in the Beichuan area, Sichuan Province, China using satellite imagery and Google Earth, *Landslides*, 6: 153-159
- Schuerch, P., Densmore, A.L., McArdeell, B.W. and Molnar, P. (2006) The influence of landsliding on sediment supply and channel change in a steep mountain catchment, *Geomorphology*, 78: 222-235

- Shen, Z.K., Sun, J.B., Zhang, P.Z., Wan, Y.G., Wang, M., Burgmann, R., Zeng, Y.H., Gan, W.J., Liao, H. and Wang, Q.L. (2009) Slip maxima at fault junctions and rupturing of barriers during the 2008 Wenchuan earthquake, *Nature Geoscience*, 2(10): 718-724
- Shou, K.J., Huang, S.T., Lin, Y.C., Fei, L.Y., Lee, J.F. and Wei, C.Y. (2009) On the correlation of sedimentation and landslides in Wu Hsi catchment influenced by the 1999 Chi-Chi earthquake. In Lee, C.T., editor, *The Next Generation of Research on Earthquake-induced Landslides: An International Conference in Commemoration of 10th Anniversary of Chi-Chi Earthquake*, National Central University, Taiwan: National Central University, pp.330-331.
- Simonett, D.S. (1967) 'Landslide distribution and earthquakes in the Bewani and Torricelli Mountains, New Guinea', in Jennings, J.N. and Mabbutt, J.A. (eds) *Landform Studies from Australia and New Guinea*, Cambridge University Press: Cambridge, pp.64-84
- Sklar, L.S., Dietrich, W.E., Foufoula-Georgiou, E., Lashermes, B. and Bellugi, D. (2006) Do gravel bed river size distributions record channel network structure? *Water Resources Research*, 42: W06D18
- Sklar, L.S. and Dietrich, W.E. (2008) Implications of the saltation-abrasion bedrock incision model for steady-state river longitudinal profile relief and concavity, *Earth Surface Processes and Landforms*, 33: 1129-1151
- Stein, R.S., King, G.C.P. and Rundle, J.B. (1988) The growth of geological structures by repeated large earthquakes, *Journal of Geophysical Research*, 93: 13319-13331
- Stone, R. (2008) Lessons of Disasters Past Could Guide Sichuan's Revival, *Science*, 321:476
- USGS (2008) 'Magnitude 7.9 - EASTERN SICHUAN, CHINA' *Earthquakes Hazard Program* (<http://earthquake.usgs.gov/egcenter/eginthenews/2008/us2008ryan/us2008ryan.php>, accessed: 14/01/2010)
- Wang, Z.H., Xu, Q.D., Xu, B. and Zhang, W. (2009a) Emergency aero-photo survey after the 5.12 Wenchuan Earthquake, China. *Science in China Series E-Technological Sciences*, 52: 835-843
- Wang, F., Cheng, Q., Highland, L., Miyajima, M., Wang, H. and Yan, C. (2009b) Preliminary investigation of some large landslides triggered by the 2008 Wenchuan earthquake, Sichuan Province, China, *Landslides*, 6: 47-54
- Warburton, J. (2006) Mountain Environments. In: Perry, C. & Taylor, K. *Environmental Sedimentology*. Oxford: Blackwell; 2007: 32-74
- Xu, Q. and Dong, X.J. (2009) "Wangjiayan landslide, Beichuan" in Xu *et al.* (2009) *Large-scale Landslides Induced by the Wenchuan Earthquake*, Science Press: Beijing pp. 174-187

- Xu, X., Wen, X., Yu, G., Chen, G., Klinger, Y., Hubbard, J. and Shaw, J. (2009) Co-seismic reverse- and oblique-slip surface faulting generated by the 2008 Mw 7.9 Wenchuan earthquake, *Geology*, 37(6): 515-518
- Yang, Z.J., Qiao, J.P., Tian, H.L., Huang, D. And Wang, M. (2010) Epicentral Distance and Impacts of Rainfall on Geohazards after the 5. 12 Wenchuan Earthquake, China, *Disaster Advances*, 3(4): 151-156
- Yin, Y., Wang, F. and Sun, P. (2009) Landslide hazards triggered by the 2008 Wenchuan earthquake, Sichuan, China, *Landslides*, 6: 139-151
- Yin, A. (2010) A special issue of the great 12 May 2008 Wenchuan earthquake (M_w 7.9): Observations and unanswered questions, *Tectonophysics*, 491: 1-9
- Yin, J., Chen, J., Xu, X.W., Wang, X. and Zheng, Y. (2010) The characteristics of the landslides triggered by the Wenchuan Ms 8.0 earthquake from Anxian to Beichuan, *Journal of Asian Earth Sciences*, 37(5-6): 452-459
- Zhou, C.H., Lee, C.F., Li, J. and Xu, Z.W. (2002) On the spatial relationship between landslides and causative factors on Lantau Island, Hong Kong, *Geomorphology*, 43(3-4): 197-207
- Zifa, W. (2008) A preliminary report on the Great Wenchuan Earthquake, *Earthquake Engineering and Engineering Vibration*, 7(2): 225-234